Layer by Layer, Nano-particle “Only” Surface Modification of Filtration Membranes

Luis Escobar-Ferrand

Submitted in partial fulfillment of the

requirements for the degree

of Doctor of Philosophy

in the Graduate School of Arts and Sciences

COLUMBIA UNIVERSITY

2013

Abstract

Layer by Layer, Nano-particle "Only" Surface Modification of Filtration Membranes

Luis Escobar-Ferrand

Layer by Layer (LbL) deposition using primarily inorganic silica nanoparticles is employed for the modification of polymeric micro and ultrafiltration (MF/UF) membranes to produce thin film composites (TFC) with potential nanofiltration (NF) and reverse osmosis (RO) capabilities.. A variety of porous substrate membranes with different membrane surface characteristics are employed, but exhibiting in common that wicking of water does not readily occur into the pore structure, including polycarbonate track etched (PCTE), polyethersulfone (PES) and sulfonated PES (SPEES) MF/UF membranes. Both spherical (cationic/anionic) and eccentric elongated (anionic) silica nanoparticles are deposited using conditions similar to those reported by Lee et al.[1] *Appropriate selection of the pH's for anionic and cationic particle deposition enables the construction of nanoparticle only layers 100 -1200 nm in thickness atop the original membrane substrates. The surface layer thickness varies monotonically with the number of bilayers (anionic/cationic deposition cycles) as expected. The deposition process is optimized to eliminate drying induced cracking and to improve mechanical durability via thickness control and post-deposition hydro-thermal treatment.*

The hydrodynamic permeability of these TFC membranes is measured to evaluate their performance under typical NF operating conditions using dead-end permeation experiments and their performance compared quantitatively with realistic hydrodynamic

models, with favorable results. For track etched polycarbonate MF substrates, surface modification causes a permeability reduction of approximately two orders of magnitude with respect to the bare substrates, to values comparable to those for typical commercial NF membranes. Good quantitative agreement with hydrodynamic models with no adjustable parameters was also established for this case, providing indirect confirmation that the LbL deposited surface layers are largely defect (crack) free. Imaging of our TFC membranes after permeation tests confirmed that no significant mechanical damage resulted, indicating integrity and robustness of the LbL deposited surface layers in typical applications.

The selectivity of these novel TFC membranes was also tested using standard "rejection" tests normally used to characterize NF and RO membranes for their capabilities in typical applications, such as water softening or desalination. We report the dextran standards molecular weight "cut-off" (MWCO) using mixed dextrans from 1.5 to 500 KDa in dead-end stir cells, and the percentage of rejection of standard bivalent and monovalent salt solutions using steady cross flow permeation experiments. The results confirm rejection of at least 60% of even the smallest dextrans, an estimated dextran MWCO of 20 KDa, and rejection of 10% and 20% for monovalent (NaCl) and bivalent ($MgSO_4$) salts, respectively, for all the TFC membranes studied, while the unmodified membranes showed no rejection capability at all. The work supports that nanoparticle based LbL surface modification of MF/UF membranes can produce filtration quality media for important water purification applications, such as nanofiltration (NF) softening processes, natural organic matter (NOM) elimination and possibly reverse osmosis (RO) desalination.

Table of Contents

List of Tables

List of Figures

Acknowledgments

At the end of a journey, the first thoughts that come to my mind have to do with expressing my gratitude, admiration and respect to the people and institutions that supported me and demonstrated their belief in my projects and dreams at all times.

First, I would like to express my sincere gratitude to my advisor Prof. Christopher J. Durning, for his guidance, knowledge and friendship. The overall quality of this work is directly related to his compromise and careful advice.

Collaboration with Prof. Daeyeon Lee's group was also very beneficial for the project. From the consolidation of an idea to achieve a tangible result, Daeyeon always provided good input and important suggestions.

During the course of the program, members of Durning's lab were also important contributors and collaborators in different aspects of the projects. The author acknowledges Lydia Ngai, Amrut Biswal, Christian Lubombo, Ji Seung Kim and also to Diya Li from Lee's lab for their valuable help and compromise with our research.

Pall Corporation has been instrumental in this endeavor. As a Pall employee, the company gave me the flexibility and the opportunity to pursue my doctoral degree financing part of my tuition and allowing me to organize my time in my own way with the compromise of performing properly in both environments and trust me, that is not at all easy….!! Midway in the degree Pall Corporation provided a research grant to finance our experimental work. In addition, Pall facilities, materials and equipment were used for multiple experiments and training was provided to execute some of the techniques presented here. My gratitude goes to Dr. Tom Gsell that believed in this project from the beginning and for his acute sense of scientific research ideas,

Dr. Amarnauth Singh for his expertise, innovation and suggestions to the service of our research; Mike Steves and Pauline Adejo from the Pall Microscopy Lab for all their training, help and extremely useful suggestions and Selina Shi for her masterful technique and help regarding dextran separations.

To be able to complete a goal of this caliber, the personal surroundings need to be in peace and equilibrium. In this regard, I would have never been able to complete this goal without the support, sacrifices, patience and encouragement of my beautiful wife Karina and her outstanding strength. My sincere thanks to the rest of my family in my beloved Chile and my friends all over the world that gave me those words of motivation and support that are always needed when the light is not seen at the end of the tunnel, especially my bud Mithun 8 Radhakrishna.

Dedicated to Karina a.k.a. Titi, my driving force

Introduction

This thesis focuses on the fabrication, by a unique method, of membranes for pressure driven filtration processes. An electrostatically driven self assembly process, Layer by Layer (LbL) deposition, enables surface modification of existing porous membranes with a thin layer of nanoparticles. The resulting thin film composite (TFC) membrane has much finer characteristic porosity than the original substrate. The LbL technique enables tailoring of the surface layer's microstructure on nanometer length-scales, as well as the layer's internal chemistry. The method can produce membranes capable of filtering suspended contaminants in the size range below 100 nm, i.e. it can produce a new class of nanofiltration (NF) and reverse osmosis (RO) membranes.

One of the main applications for membranes of this type is water purification, a critical technology challenge due to the increasing scarcity of good quality natural aquifers in many regions of the world.[1] A metric derived from local water availability, the total water use and the local environmental water requirements is the water stress indicator (WSI). Figure 1 shows a world map highlighting the WSI around the globe as of 2004.[1]

According to the WSI index, agricultural, drinking and industrial use water supplies are in severe danger in the regions where the WSI exceeds 0.7, generating an enormous potential social and political problem if these issues are not resolved in a reasonable time. Estimates indicate water scarcity now affects one in three people on every continent of the globe and it is projected to affect almost two thirds of the global population by 2025.[2, 3, 4] The situation is getting worse as the necessity for water rises along with population growth, urbanization and increases in household and industrial uses.[2] Almost one fifth of

the world's population (about 1.2 billion people) currently live in areas where water is physically scarce. One quarter of the global population also currently live in developing countries that face water shortages due to a lack of infrastructure to obtain and distribute water from rivers and aquifers.[2, 4, 5]

About 70 percent of the total water withdrawn worldwide is for agriculture; in some regions, it is more than 80 percent. In many regions a lack of water has driven up the use of wastewater for agricultural production in poor urban and rural communities. More than 10% of people worldwide consume foods irrigated by wastewater that can contain harmful chemicals or disease-causing organisms, increasing the risk of diarrheal diseases such as cholera, typhoid fever and dysentery, and other water-borne infections.[2] In any region when more than 75 percent of river flows are diverted for agricultural, industrial and municipal purposes, there is typically not enough water to meet both human demands and environmental flow needs. Physical water scarcity, accompanied by severe environmental degradation, declining groundwater, and water allocations that favor some groups over others, is already a reality when this figure reaches 60 percent. Such is the case already in regions where the stress on natural water resources is severe. Water withdrawals are highest in arid and semi-arid lands, where they are needed mostly for irrigation, and lowest in tropical countries.[5]

Wastewater reuse and sea water desalination have emerged as the two principal foci of technology development to address these growing problems. Several significant advances through membrane technologies have been achieved.[6, 7] The development of the membrane bioreactor (MBR), the “active integrated” desalination membrane process system using hollow fiber micro/ultrafiltration in tandem with reverse osmosis (MF/RO),

and nanotechnology and novel polymers expected to drive down the cost in the near future appear as the most notable in this regard.[4, 6]

As mentioned, the membranes we have been able to fabricate in this work can provide a new set of filters capable in water nanofiltration (NF) and in the most important applications of reverse osmosis (RO) technology, water desalination. We describe these applications briefly in what follows.

Water Nano-filtration: Being classified erroneously as "low pressure RO" nanofiltration (NF) is a relatively recent membrane filtration process used normally when brackish water, found in many surface and ground water streams, is the source. The purpose of NF is primarily softening [8], i.e. the removal of relatively large dissolved bivalent cations and anions, removal of disinfection by-product (DBP) precursors and/or small size scale natural organic matter (NOM).[8, 9] The source is classified as brackish if its total dissolved solids (TDS) are in between 1000 and 5000 mg/L.[8, 10] NF operations lie between ultrafiltration (UF) and reverse osmosis (RO) with respect to the size of the contaminants that can be screened.[9] Specifically, NF membranes can reject bivalent cation solutes and therefore have a nominal pore size below 100 nm. The NF membranes are usually rated by a molecular weight cut-off (MWCO), for dissolved dextran standards rejection, or percentage of a particular bivalent salt rejection, rather than nominal pore size.[7, 9] NF has become widely used in food processing applications of dairy products for simultaneous concentration and partial (monovalent ion) demineralization.[11, 12] While feed pressures for typical RO applications (e.g. desalination of sea water) range from 6000-8000 KPa in order to overcome the relatively high osmotic pressure, those for brackish waters and NF softening applications are relatively low, varying between 600-

3000 KPa.[7] Consequently, NF operations have much lower capital and operational costs than do typical RO operations.[7] However, current NF membranes are susceptible to scaling and fouling and feed modifiers such as anti-scalants are generally required for practical use.[8]

Water Desalination: Efficient desalination of water has been a technology goal for decades.[7, 13] Considering that more than 97.5% of the earth's water is either brackish or seawater, that 1.7% is located in the ice caps and that only 0.8% of the total is considered "fresh water" for use[7, 13, 14] there is an obvious current interest in developing reliable technologies to remove dissolved salts to produce fresh potable water. The increasing scarcity of potable water world-wide has intensified research efforts in this direction. [7, 13, 14] Reverse Osmosis (RO) technology is currently the most prevalent, effective technology for this purpose.[1, 7] Although effective, the current technologies has several disadvantages that make the process expensive and difficult to control. For example, the majority of current RO membranes, based on polyamides, exhibit very low resistance to typical processes that are required periodically to clean (defoul) membranes in operation, limiting their effective lifetime severely.

In summary, the growing global water supply problems pose challenges for the current NF and RO technologies. New commercial NF and RO membranes will be very beneficial in the near future. The main motivation for this work is to address this need, at least in part. We developed a new class of thin film composite (TFC) membranes using Layer by Layer (LbL) deposition onto existing microfiltration (MF) and ultrafiltration (UF) polymeric membranes. In this proof-of-concept effort the deposited surface layer consists primarily of inorganic nanoparticles. The resulting membranes, which have NF

or RO rating, with good chemical resistance could be a potential solution to many of the disadvantages of existing membranes. The distinct benefit of the LbL method is that it allows nano-molecular scale design of the surface layer according the application requirements. Indeed several parameters of the TFC architecture can be manipulated easily by this method which could be applied to form TFC membranes in the NF and RO range, engineered for rejection of particular contaminants.

The thesis is organized into four main chapters. Chapter 1 demonstrates the fabrication of TFC membranes by surface modification of existing organic microfiltration/ultrafiltration (MF/UF) membranes (symmetric and/or asymmetric) with inorganic nano layers via aqueous based Layer by Layer (LbL) deposition. Experimental verification of methods that prevent drying-induced cracking is included. The effort in this chapter encourages the view that the fabrication method is robust with respect to the materials used (substrates, nanoparticles).

Chapter 2 demonstrates convincingly using hydrodynamic permeability tests that the TFC membranes produced are likely defect free and have fluxes competitive with existing NF/RO membranes under typical commercial operating conditions. The measured TFC membrane permeabilities compare well with realistic hydrodynamic models without adjustable parameters. Chapter 3 reports on the selectivity of the TFC membranes produced. The rejection levels for dissolved dextran standards and salts by the surface modified membranes demonstrate that our TFC architecture can convert MF and UF membranes to applications typically in the NF range like softening or removal of fine natural organic matter (NOM) and to the RO application of desalination. Finally, Chapter 4 is an initial effort to develop a rigorous theoretical treatment for NF/RO

processes that includes well define molecular-level parameters. Ultimately, a molecular level theory provides greater capability to engineer TFC membranes for applications. The main goal of that chapter is to link Curtiss and Bird's multicomponent flux laws[15] to the free volume treatment of Vrentas and Duda.[16] The important output defines the essential transport coefficients needed to predict the steady flux of species through a membrane under an applied pressure drop in the free volume framework. Future experimental scrutiny of these results will permit a better understanding of the transport mechanisms relevant to NF and RO membranes, especially with respect to the effects of fixed charge and water content in membranes.

References

1. Smakhtin, V.; Revenga, C.; Döll, P. *Water International* **2004**, 29, 307-317.
2. World Health Organization & UNICEF *Water for Life* **2005**.
3. Elimelech, M; Phillip, W.A. *Science* **2011**, 333, 712-717.
4. Service, R.F. *Science* **2006**, 313, 1088-1090.
5. United Nations *The Millenium Development Global Report* **2009.**
6. Shannon, M.A.; Bohn, P.W.; Elimelech, M.; Georgiadis, J.G.; Mariñas, B.J.; Mayes, A.M. *Nature* **2008**, 452, 301-310.
7. Greenlee, L.F.; Lawler, D.F.; Freeman, B.D; Marrot, B.; Moulin, P. *Water Research* **2009**, 43, 2317-2348.
8. Van der Bruggen, B.; Manttari, M.; Nystrom, M. *Separation and Purification Technology* **2008**, 63, 251-263.
9. Ulbricht, M. *Polymer* **2006**, 47, 2217-2262.
10. Ela, Wendell P., *Introduction to Environmental Engineering and Science*, **2007** Prentice Hall, 3rd ed.
11. Van der Horst, H.C.; Timmer, J. M. K.; Robbertson, T.; Leenders, J. *Journal of Membrane Science* **1995**, 104, 205-218.

12. Kelly P.M.; Horton B.S.; Burling, H. *New Applications of Membrane Processes* **1991**, 130-140.

13. Cooley, H.; Gleick, P.H.; Wolff, G. *Desalination with a Grain of Salt* **2006**, Pacific Institute.

14. Gleick, P.H. Water resources. In *Encyclopedia of Climate and Weather*, **1996** ed. by S. H. Schneider, Oxford University Press, New York, vol. 2, 817-823.

15. Curtiss, C.F.; Bird, R.F. *Industrial & Engineering Chemistry Research* **1999,** 38, 2515-2522.

16. Vrentas, J.S; Duda, J.L. *Journal of Polymer Science: Polymer Physics Edition* **1977,** 15, 403-416.

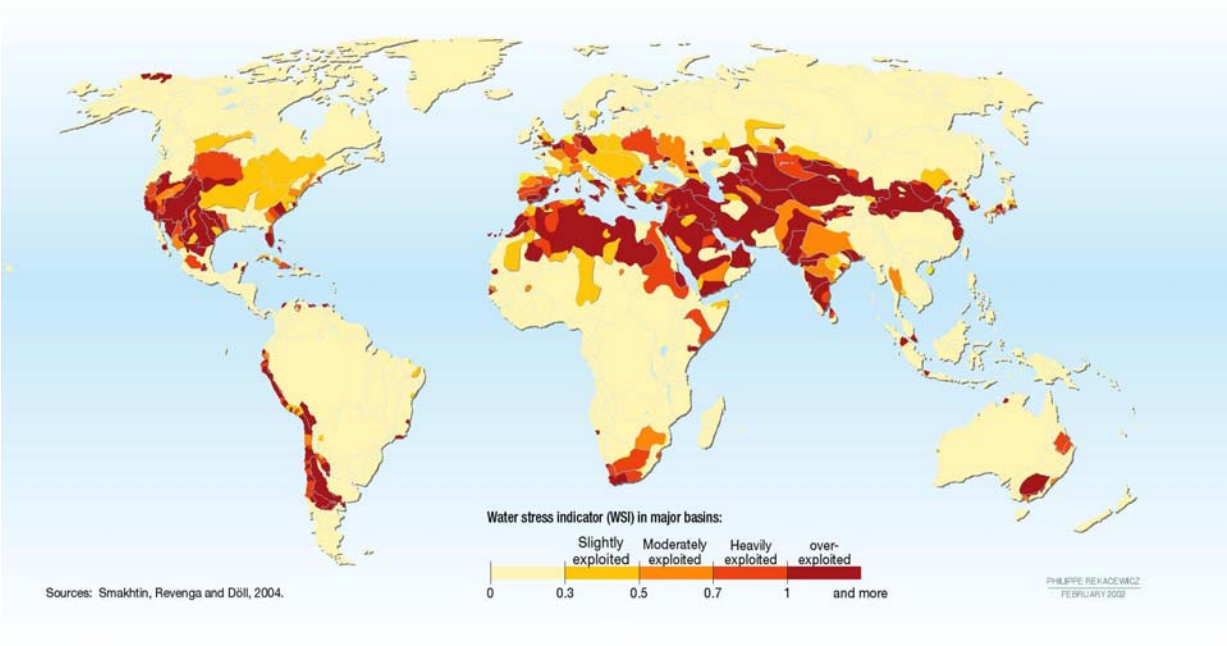

Figure 1. *Water Stress Indicator (WSI) Global Map.*[1]

Chapter 1. Nanoparticle "Only" Layer by Layer Surface Modification of Microfiltation/Ultrafiltration (MF/UF) Membranes

Abstract

Layer by Layer (LbL) deposition using primarily inorganic silica nanoparticles is employed for the modification of polymeric micro and ultrafiltration (MF/UF) membranes. A variety of porous substrate membranes with different membrane surface characteristics are employed, but exhibiting in common that wicking of water does not readily occur into the pore structure, including polycarbonate track etched (PCTE), polyethersulfone (PES) and sulfonated PES (SPEES) MF/UF membranes. Both spherical (cationic/anionic) and eccentric elongated (anionic) silica nanoparticles are deposited using conditions similar to those reported by Lee et al.[1] Appropriate selection of the pH's for anionic and cationic particle deposition enables the construction of nanoparticle only layers 100 -1200 nm in thickness atop the original membrane substrates. The surface layer thickness varies monotonically with the number of bilayers (anionic/cationic deposition cycles) as expected. The deposition process is optimized to eliminate drying induced cracking and to improve mechanical durability via thickness control and post-deposition hydro-thermal treatment. The work suggests that nanoparticle based LbL surface modification can be systematically manipulated to achieve goals for particular membrane applications, e.g. nanofiltration (NF) softening processes, natural organic matter (NOM) elimination and reverse osmosis (RO) desalination.

1.1. Introduction

In membrane technology, "thin film composite" (TFC) membrane refers to multi-layer films consisting of a porous nonselective support layer with a very thin selective barrier layer on top. Such structures have become standard for demanding "filtration" applications including nanofiltration (NF) and reverse osmosis (RO). The main advantage of TFC architectures is the high flux, due to the thinness of the selective top layer, combined with mechanical integrity, due to the porous support layer. Important examples are the interfacially polymerized polyamide composite membranes for desalination by RO known for their high rejection and high flux due to the very thin skin layer.[2] The skin layer and support core are complementary and can be optimized independently.[3] For example Hoek et al[4] added zeolite nanoparticles during the polyamide membrane interfacial polymerization process to tailor the top skin layer for better RO membrane separation performance in a TFC system. As a result, the TFC membranes have been developed to provide good selectivity and flux with reasonable mechanical, thermal and chemical stability, and even self-cleaning properties.[2, 3, 5, 6]

Despite the innovation of TFC architectures, the set of TFC membranes available for the important applications of water nanofiltration and water desalination remains limited. For example, at present mainly the interfacially polyamides are used for desalination via RO.

In this work we demonstrate modification of surfaces of organic microfiltration (MF) and ultrafiltration (UF) membrane supports with contiguous inorganic nanoparticle thin layers to obtain defect free TFC membranes with NF or RO rejection capabilities. The methodology achieving this employs layer by layer deposition (LbL) enabling the fabrication of "engineerable" highly selective top layers on the substrate.

1.2. Layer by Layer (LbL) Deposition Process

LbL deposition was reported first by Iler more than 40 years ago[7]. It has been explored and developed since then as a thin film deposition and surface modification process especially during the last twenty years. It can be thought of as "directed" self assembly, enabling preparation of thin films with controlled nanostructure.[1, 8, 9] The LbL process is simple, robust and employs mild, environmentally friendly reagents and conditions. It has become a primary tool for thin film fabrication.[8, 9, 10, 11] The unique advantages of the method are that a wide variety of materials, both organic and inorganic, can be incorporated into LbL thin films and that the film architecture is largely controlled by the deposition sequence. Compared with many other methods for thin film fabrication, (e.g. vapor phase deposition, surface initiated polymerization) LbL offers easier preparation and more durable, largely defect free deposited layers. [2, 3, 6, 12] In addition, a variety of deposition protocols work well (e.g. dip/rinse cycles, spin processing, spray processing) all resulting in essentially the same thin film structures.[13, 14] Some minor differences do result from the various protocols, e.g. when compared with spraying, the dipping LbL sequence produces thicker, denser and somewhat smoother films.[13, 14] The flexibility with respect to deposition protocol makes fast, automated industrial processing possible.

Multilayer thin films from LbL appear in several applications such as antifogging, and/or antireflection coatings and self cleaning surfaces.[1] The literature also mentions applications in sensors fabrication, friction reducing coatings, integrated optics and electronic device fabrication.[8, 9, 10, 11] Several industries have benefited by the development and application of this technique such as the semiconductor, automotive and construction industries.[1]

The most common LbL process involves dipping an initially charged substrate (e.g. cationic) into a dilute aqueous solution of the complementary anionic polyelectrolyte and

allowing the polymer to adsorb and "overcharge" the substrate surface. The negatively charged coated substrate is rinsed to remove free (unbound) polyanion and dipped into a solution of a cationic polyelectrolyte, which adsorbs and re-creates a positively charged surface. Sequential, alternating adsorptions of anionic and cationic polyelectrolytes allow the construction of multilayer films.[8, 10] Fig. 1-1 shows a process schematic.

Chen and McCarthy[9] reported using LbL on PET films to prepare TFCs resembling TFC membranes. Podsiadlo et al[15, 16] reported tailoring nanoarchitectures of the deposited film's using LbL and have demonstrated high mechanical strength of TFC overlayers produced by LbL. They also demonstrated the superior mechanical properties of hybrid organic-inorganic nanocomposite films prepared by this method. These efforts inspire the current work, whose aim is to create TFC filtration membranes via LbL modification of microporous MF and UF membranes.

1.3 Experimental

1.3.1 Materials

All materials were used as received. Poly(allylamine hydrochloride) (PAH, M_w = 56,000 Dalton), and Poly(acrylic acid) (PAA, M_w=100,000 Dalton, 35 wt% solution in water) were purchased from Sigma Aldrich (St. Louis, MO). Ludox® CL colloidal spherical silica nanoparticles (30 wt% solution in water) 15 nm average diameter, and Ludox® TM-40 colloidal spherical silica nanoparticles (40 wt% solution in water) 25 nm average diameter were purchased from Sigma Aldrich (St. Louis, MO); Snowtex®-UP 9-15 nm width, 40-100 nm length basic colloidal elongated silica nanoparticles and Snowtex®-OUP 9-15 nm width, 40-100 nm length acid colloidal elongated silica nanoparticles were obtained through Nissan Chemical America (Houston, TX). Hydrochloric Acid (HCl) (5M) and Sodium Hydroxide (NaOH) (5M) solutions

to adjust pH were prepared from NaOH (ACS grade, ≥ 97%) obtained from Sigma Aldrich (St. Louis, MO) and HCl purchased from Amend Drug and Chemicals Ltd. (Irvington, NJ). DI water obtained from a Millipore Q-Gard® 1 and Progard® 2 (Billerica, MA) systems. Diced silicon wafers 16006 (10 cm diameter, each 10x10mm) were obtained from Ted Pella Inc.(Redding, CA)

A stock polyelectrolyte solution of PAH was prepared with 0.94 g/L of PAH in DI water adjusted to pH 7.5 using 5M NaOH. A stock solution of PAA was prepared by dissolving 2.06 g/L of PAA in DI water and then adjusting to a pH of 3.5 using 5M HCl. Stock nanoparticle solutions were prepared at 1.00 g/L for Ludox® CL, 0.75 g/L for Ludox® TM-40, 1.50 g/L for Snowtex®-UP and 1.94 g/L for Snowtex®-OUP. The pHs were adjusted to 3.0, 3.0, 10.0, 4.0-6.0 respectively, by 5M NaOH or 5M HCl. Concentrations and pH values for stock solutions were chosen to match values reported in the literature ensuring optimal conditions for building LbL multilayers.[1, 17, 18] For elongated nanoparticles (Snowtex®) we tried different pHs and selected the optimal values reported later in this chapter.

A variety of flat-sheet membrane substrates were used for this work. Nuclepore® Track-Etch Polycarbonate (PCTE) membranes from Whatman (Kent, UK) were used with nominal pore sizes of 0.03 μm, 0.05 μm, 0.08 μm , 0.1 μm and 0.2 μm. Omega® Poly(ethersulfone) (PES) membranes with dextran standards molecular weights cut-offs (MWCO) of 100 KDa, 300 KDa, 500 KDa and 1000 KDa; Supor® PES (Supor 100, Supor 100H Thin, Supor 200, Supor 200 WE4 and AA Supor 200) with 100 nm and 200 nm nominal pore size; Nylon AN-15 and AN-25 membranes with 100 and 150 nm nominal pore size respectively and Sulfonated Poly(etherethersulfone) (SPEES®) membranes with dextran standards MWCO of 10 KDa & 100 KDa were all obtained from Pall Corporation (Port Washington, NY). Table 1-1 shows a

summary of the substrates properties and Figure 1-2 (a) and (b) show representative SEM micrographs of two of the substrates employed.

1.3.2 Characterization Methods

Morphological characterization of the substrates and TFC membranes fabricated was conducted using several techniques. Atomic force microscopy (AFM) was performed using a TopoMetrix Explorer Microscope (now Veeco Instruments) (Santa Clara, CA) with software version 5.01. Cross section and frontal incidence scanning electron microscopy (SEM) for relatively low magnifications (less than 40,000 X) was conducted with a JEOL JSM-5600 LV Microscope (Tokyo, Japan) and for higher magnifications (up to 500,000 X) with a Zeiss LEO 1550 high resolution field emission SEM Microscope (Cambridge, UK) equipped with a Schottky Field Emitter (FESEM). Energy dispersive X-Ray spectroscopy (EDX) on fracture cross sections was performed with a prism/digital spectrometer from Princeton Gamma Tech (PGT) (Princeton, NJ) Image analysis was done using the Nikon NIS-Elements Advanced Research software (Melville, NY).

Sample Preparation for SEM microscopy and Energy Dispersive X-ray Spectroscopy (EDX). Samples for SEM, EDX and FESEM were prepared on aluminum stubs. For frontal incidence SEM (top view) samples were adhered to stubs with double sided tape or a suitable conductive adhesive (except for polycarbonate membranes). More than one sample could be placed on a stub. For polycarbonate membranes, an Au/Pd coating was placed, along the edges of the sample to adhere the membrane to the stub. For cross-section samples, 45° aluminum stubs were used. A rectangular piece of sample about 2 cm long and ½ to 1 cm wide was cut and, using forceps, it was immerse into a wetting fluid for the membrane allowing it to wick in and imbibe completely into the sample. Isopropanol or Filmex® were used as the wetting

liquids. Using forceps, the saturated sample was submerged in liquid nitrogen, and quickly snapped to break the sample cleanly, producing a freeze fracture surface. The sample was then air dried and adhered to an angled aluminum stub with the fracture edge protruding slightly over top stub's edge.

SEM Imaging. The JEOL 5600 LV instrument was setup for 1280x960 pixels image collection which took approximately 60 to 90 seconds per image to collect data. Each image generated by the JEOL SEM carries a scale bar in μm, date and text sample identification. This information is displayed on the SEMs included in this work. The images are saved with a standard name format consisting of 2 digits for the year, 2 digits for the month, 2 digits for the day and 3 digits for an image number (yymmddxxx). The image number is not user controlled and is reset at the beginning of each day by the instrument's software. The images are numbered consecutively starting at 001 each day. The images are stored in bmp format by the JEOL 5600 SEM software. The images generated by the LEO FESEM carry the same information and the procedure to obtain the images is similar. The images are stored in tif format by the LEO 1550 FESEM software.

Energy Dispersive X-ray Spectroscopy. The main purpose of energy dispersive X-ray spectroscopy (EDX) is to chemically depth profile our samples to determine where nanoparticles reside. Cross sectional freeze fracture samples, prepared as described previously, are used for the EDX depth profiling. The Princeton Gamma Tech (PGT) instrument, which is attached to the JEOL SEM, first performs a low resolution area scan of the sample, at approximately 200X, to obtain a record of major, minor, and trace elemental identities. The area surveyed by this first scan is approximately 3.0-3.5 mm^2. Following this, we performed additional scans from 500 X

to1200 X at 512 x 512 pixels for depth profiling surveying areas as small as 0.8-1.0 mm^2. The instrument resolution obtained at the highest magnification is 0.4 μm/pixel.

AFM. The main purpose for carrying out AFM scans of TFC membrane surfaces was to inspect the LbL film surface morphology, specifically the cracking morphology. The instrument was operated in non-contact mode, normally used for soft samples, with a special silicon probe model LTESP-MT from Bruker AFM Probes Instruments (Camarillo, CA), and adjusting to set an optimal instrument frequency for this application. The latter was determined by the cantilever maximum peak (the resonance value obtained on the spectrum plot of amplitude vs. frequency) measured after the beam alignment. After setting the optimal frequency, AFM scans for sample topology were performed with a resolution on the order of a nanometer. The AFM images were named by the instrument software with the same format as the SEM software: 2 digits for the year, 2 digits for the month, 2 digits for the day and 3 digits for the image number. The AFM images were stored in zfp and tif formats.

1.3.3 Programmable Dipper, Glass and Frames Sample Holders

A Microm MS-50 slide stainer (Zeiss, Thornwood, NY) interfaced to a desktop computer was adapted for this work and used as a programmable dipper for performing the LbL coating process on porous membranes. Cationic and anionic polyelectrolytes and both spherical (cationic/anionic) and elongated (anionic) silica nanoparticles were deposited by this device using solutions and dipping conditions similar to those reported by Lee et al.[1] Appendix-A shows the run-time commands required to conduct a typical dipping LbL experiment.

Porous flat-sheet MF and UF membranes selected for this work were surface modified in the dipper using two different sample holders according to the use of the resulting TFC membrane. They were either adhered to glass slides or clamped in specially designed frames.

TFC's fabricated on glass slides were mainly employed for imaging and EDX. The frames were designed to allow surface modification on only one side of the membrane and permitted subsequent removal from the frame. These samples were used in hydrodynamic permeability and selectivity experiments on the TFC membranes (see Chapters 2 and 3). Frames were machined out of acrylic and Rulon® polymers and assembled with Zip glue®.

1.3.4 Glass Cleaning

All glassware used in any capacity passed through the same cleaning procedure. As received glassware was first washed in surfactant solution (2% w/w solution of Alconox®) and then rinsed repeatedly with tap water followed by several rinses with DI water. The glass was then rinsed in an alternating fashion in double baths of DI water and acetone until bubbles stopped appearing on the glass surface or at least 10 times in each bath followed by a final rinse with DI water. The clean glassware was finally stored under a 1% v/v HNO_3 solution. Before using any glass material, the pieces were taken out from the acid solution and given a careful rinse with DI water followed by air drying in a laminar flow hood.

1.3.5 Mounting Samples for Dip-coating

Glass Holders. Ten bilayers of polyelectrolytes were first deposited onto flat glass sample holders to adhere membranes, which were also dipped in the same polyelectrolytes. This polyelectrolyte "molecular glue" mounted samples securely for the subsequent dipping process. The last coat on the glass was with the polyanion PAA. To adhere the membrane to the polyelectrolyte coated glass, it was dipped with only 2.5 bilayers of polyelectrolytes, ending on the polycation PAH, then placed on the glass under DI water. When dry the glass holder and membrane adhered strongly.

The glass flat with membranes was either fastened to the dipping basket with clips, or just set inside the dipping basket, depending on the type of dipping basket and how many samples are being coated. Clips permitted multiple samples to be coated at once (see Figure 1-3.).

Frame Holders. The uncoated membrane, manipulated using tweezers, is placed flush against a clean glass slide with few drops of DI water. The glass slide is carefully centered and aligned in a slot machined into the top half of the frame before closing. The closed frame is secured and fixed with stainless steel clips positioned such that sealing to the frame base occurs. The sealed frames were then placed in the basket of the dipper. The frame assembly process is illustrated in Figure 1-4.

1.3.6 Polyelectrolyte Coating

The most reproducible results we obtained depositing nanoparticle layers were observed ensuring a strong surface charge prior to the nanoparticle deposition. Consequently all LbL preparations reported here feature a precursor polyelectrolyte layer directly atop the porous substrate to facilitate subsequent adsorption of the nanomaterials. In particular 2.5 polyelectrolyte bilayers were deposited directly on top of the membrane surface to assure high surface charge density. The dipping process starts with cationic PAH solution for 10 minutes followed by two DI rinses for 2 and 1 minutes, respectively. Then follows dipping in the anionic PAA solution for 10 minutes, with two DI water rinses of 2 and 1 minutes each. This would complete a first bilayer of polyelectrolyte coating. The precursor coating process stops midway during the third layer after a PAH dip and the two DI water rinses. Presumably, as a result of this sequence, the sample surface becomes positively charged and ready for the first dip into anionic nanoparticle solution. Figure 1-2 (c) and (d). shows representative fracture surface SEM micrographs of the polyelectrolyte precursor layer we believe is typical for the substrates used.

1.3.7 Nanoparticle Deposition

LbL deposition was carried out immediately following precursor coating. The sample is repositioned to the staring bath of the dipper. The solution and DI water baths were changed to hold nanoparticle solutions and fresh DI water. Dipping commenced in anionic particles (Ludox Cl or Snowtex-UP) for 10 minutes and proceeded to three rinses with DI water for 2, 1and 1 minute, respectively. The sample then proceeded to the next bath containing cationic nanoparticles (Ludox-TM 40) for 10 minutes followed by three DI water rinses of 2, 1 and 1 minute, respectively. This would complete 1 bilayer cycle of nanoparticle deposition. The whole sequence was iterated up to 300 times to achieve the desired number of bilayers. The whole process could be programmed and controlled by computer. Following nanoparticle deposition the TFC samples were air dried and stored in the laminar flow hood. The nanoparticles employed in this study were imaged by SEM after deposition onto cleaned glass substrates treated with a polyelectrolyte precursor layer and onto membrane substrates (see Figure 1-5).

1.3.8 Autoclaving the Sample

As discussed subsequently, a post treatment was applied to some samples to reduce the occurrence of cracking in the deposited nanoparticle layer. After completing the nanoparticle deposition, some TFC membrane samples mounted on glass slides were first air dried for about 30 minutes in a laminar flow hood and then put into an autoclave oven and subject to a wet (100% humidity) autoclaving (heating) cycle at 121ºC for approximately an hour. After nanoparticle deposition, air drying and possible autoclaving, samples were stored in a laminar flow hood awaiting analysis or testing.

1.4 Results and Discussion

1.4.1 TFC Membrane Morphology

The initial attempts to prepare TFC membranes were conducted using a variety of different porous substrates from 10-300 bilayers of the spherical nanoparticles (Ludox®) on top, resulting in surface layer thicknesses as large as 3 μm atop the porous membrane substrates. Imaging made clear that the resulting TFCs have a very sharp interface between the deposited layer and the substrate (see Figure 1-6). The substrates used for surface modification have different characteristics regarding hydrophobicity, surface charge, rating and wetting chemistry as described in detail in Table 1-1. However, the ability of preventing wicking of water into the porous interior is present in all cases regardless of the substrate used. This appears to be important in successful deposition localized at the surface even without polyelectrolyte precursor (i.e. only nanoparticles) suggesting that "no wicking" is key to achieve these results.

1.4.2 Energy Dispersive X-ray Spectroscopy

Depth profiling characterization of deposited over layers was conducted by EDX elemental analysis to check that no significant intrusion into the substrate pore occurred in our systems. Representative results are shown on figure 1-7. The technique, based on SEM images of 512 x 512 pixels, shows the presence of the great majority of silica nanoparticles on the membrane surface with little silica getting deposited within the porous interior of substrates within a resolution of 0.4 μm/pixel. The method indicates a ratio of more than 50 times between silica detected in the surface deposited layer and that detected in the interior based on silica weight percentage composition on the spot points selected across the TFC thickness.

1.4.3 Thickness vs. Number of Bilayers

Given qualitative indications of success, a primary question to be answered was if LbL in these systems obeyed the most commonly found linear growth law, i.e. if the thickness of the deposited layer increased linearly with the number of bilayers.[1, 10, 17, 18]

Measurements were made of deposited layer thickness to determine its variation with the number of bilayers deposited. Depositions were made onto both silicon wafers with a native oxide coating and porous membrane substrates (PCTE 0.03 μm). Deposited layer thicknesses were calculated from fracture cross section SEMs by NIS software. Experiments were performed for the spherical/spherical and spherical/elongated nanoparticle combinations using concentrations and pH's indicated earlier.

Figure 1-8 shows data for these experiments, which indicate, in both cases and for both types of substrates, a monotonic increase of the deposited layer thickness with the number of bilayers. Although exhibiting scatter, the results are most consistent with a linear growth law. It appears that the thickness of deposits increases faster for depositions on silicon than for the case of porous substrates, especially on the spherical elongated case. The slopes observed in Figure 1-8, for both cases, are much lower than the geometric estimate considering the monolayer thickness as the particle diameter and two monolayers of nanoparticles per bilayer.

1.4.4 Cracking Phenomena

While the forgoing results clearly indicate LbL deposition can effectively create a surface layer on a porous substrate, it was also clear that TFCs were not intact and that cracks ran through the top coating's length and breadth (See Figures 1-6 and 1-9). The cracking phenomena appeared to be ubiquitous and the efforts were concentrated on determining the origin of this cracking, and to produce crack-free, intact TFC samples required for membrane filtration

applications. AFM microscopy studies on the cracks, determined that in most of the cases the crack contours are elevated relative to the rest of the sample (see Figure 1-6). It was noticed, from frontal incidence SEMs a pattern geometry to the cracking with a characteristic length, reminiscent of findings on drying induced cracking of particle beds in the colloid literature.[19] Figure 1-9 shows representative results for our systems. The crack's geometric pattern resembles closely the ones observed in colloidal systems except for a change in scale. The drying induced cracking mechanism anticipates raised edges along crack contours which are produced due to lateral compressive stresses during the drying process causing the cracking.[19, 20, 21] To further support the assertion that the cracking exhibiting patterns such as in Figure 1-9 was due to drying and not to mechanical failure during handling of samples after coating, several experiments were designed.

We examined the morphology of cracks induced mechanically. TFC samples were purposely bent through a known radius of curvature (rolling test schematized in Figure 1-10.), and exposed to the stress of folding and pressing. SEM imaging shows a distinctly different crack morphology results from mechanical bending (rolling or folding) compared with the results observed in Figures 1-6 and 1-9.

This evidence strongly suggests drying induced cracking is the main cause of the surface defects in our system. If true, by analogy , the deposited thickness is the most important variable controllable to prevent such cracking. In fact, analysis of the drying process indicates a thickness threshold h_c, below which one avoids the stiffness associated with a thick over layer and consequent damaging drying stresses.[20]

$$h_c = 0.64\left[\frac{GM\phi_r R^3}{2\gamma}\right]^{1/2}\left[\frac{2\gamma}{-P_m R}\right]^{3/2} \qquad (1\text{-}1)$$

Here, G is the shear modulus of the particles, M the coordination number of the "packed bed" of spheres, ϕ_r the particle volume fraction at random close packing, R the particle radius, γ the water air interfacial tension, and P_m the maximum capillary pressure. From Equation 1-1, the maximum theoretical thickness for crack-free films of our systems corresponds to a NP-LbL film of ~100 bilayers.

Testing the threshold limit calculated was carefully done by examining the surface in one system of a series of thinner films. Indeed crack-free TFC's for several combinations of substrates/polyelectrolytes/nanoparticles are observed for thin enough depositions in Figure 1-11.

The sample post-treatment also seems to have a role in the fabrication of defect free composites. The thermal treatment ensures adhesion of the top layer, provokes sintering of the nanoparticles by chemical hydrolysis of SiO_2 bonds that are induced by the high temperature, enhances the film durability and removes residual defects of the TFC fabricated. It would also compact the top layers making the particles stiff and consequently thinner.

1.5 Conclusions

LbL appears to work atop porous substrates, provided wicking of the dipping solution is avoided. Silica nano-particle surface layers showed a very sharp interface independent of support. The deposited layer thickness increases with respect to the number of bilayers for porous substrates very much like that on smooth contiguous solids, although at a lower rate, and appears to follow a linear growth law.

This work demonstrates preparation of defect free thin film composite (TFC) membranes through LbL surface modification of polymeric porous MF/UF membranes, using primarily inorganic nanoparticles. These membranes hold promise for NF/RO applications and may provide new options for water purification applications. Crack free TFC membranes were

consistently achieved by considering the thickness threshold below which damaging drying induced cracking was avoided. Crack-free surface layers are possible with thin enough layers and post treatment by autoclaving stabilizes these layers.

Further improvements regarding fabrication of TFC's using the LbL deposition technique are certainly possible. The choice of the assembly method, e.g. dip coating vs. spray coating could reduce the time scale for samples.

The robustness of the method developed suggest that it could be applicable to many substrate materials and a variety of nanoparticles with different nano-architectures (e.g. multi and single-walled carbon nanotubes, nanowires, cellulose whiskers, graphenes, etc.). Complementary work reports on the permeability characteristics of these TFC membranes.

Acknowledgements

The author acknowledges Prof. Daeyeon Lee from UPenn for his collaboration work with our group and his important input during the fabrication of nanocomposites.

The author especially thanks Mike Steves and Pauline Adejo from Pall Corporation Microscopy Lab, where most of the imaging was conducted, for all their suggestions and training regarding multiple microscopy techniques and the Materials Microscopy Lab of SUNY Stony Brook University where the high resolution FESEM was performed. The author also acknowledges Dr. Elliot Campbell for his help with equipment, facilities and suggestions. My gratitude to the members of Durning's Lab, Amrut Biswal, Lydia Ngai and Ji Seung Kim and also to Diya Li from Daeyeon's Lab for their assistance during this tiring process. Last but not least, the author thanks Dr. Tom Gsell and Dr. Amarnauth Singh for their support of this work. Partial funding for this research was provided by a Pall Corporation grant.

References

1. Lee, D.; Rubner, M.F.; Cohen, R. *Nanoletters* **2006**, 6, 2305-2312.

2. Petersen, R.J. *Journal of Membrane Science* **1993**, 83, 81-150.

3. Schmidt, G.; Malwitz, M. *Current Opinion in Colloid and Interface Science* **2003**, 8, 103–108.

4. Jeong, B.; Hoek, E.M.V.; Yan, Y.; Subramani, A.; Huanga, X.; Hurwitz, G.; Ghosha, A.K.; Jawor, A. *Journal of Membrane Science* **2007**, 294, 1–7.

5. Ramakrishnan, S.; McDonald, C.J.; Prud'homme, R.K.; Carbeck, J.D. *Journal of Membrane Science* **2004**, 231, 57-70.

6. Lee, D.; Gemici, Z.; Rubner, M.F.; Cohen, R.E. *Langmuir* **2007**, 23, 8833-8837.

7. Iler, R.K. *Journal of Colloid Interface Science* **1966**, 21, 569-594.

8. Decher, G. *Science* **1997**, **277**, 1232-1237.

9. Chen, W.; McCarthy T.J. *Macromolecules* **1997,** 30, 78-86.

10. Decher, G.; Schlenoff, J.B. *Multilayer Thin Films* **2003,** Wiley-VCH.

11. Crespilho, F.N.; Zucolotto, V.; Oliveira Jr., O.N.; Nart, F.C. *Electrochemical Science* **2006**, 1, 194-214.

12. Gemici, Z.; Shimomura, H.; Cohen, R.E.; Rubner, M.F. *Langmuir* **2008**, 24, 2168-2177.

13. Kolasinska, M.; Krastev, R.; Gutberlet, T.; Warszynski, P. *Langmuir* **2009**, 25, 1224-1232.

14. Izquierdo, A.; Ono, S.S; Voegel, J.C.; Schaaf, P.; Decher. G. *Langmuir* **2005**, 21, 7558-7567.

15. Podsiadlo, P.; Michel, M.; Critchley, K.; Srivastava, S.; Qin, M.; Lee, J.W.; Verploegen, E.; Hart, A.J.; Qi, Y.; Kotov, N.A. *Angewandte Chemie International Edition* **2009**, 48, 7073-7077.

16. Podsiadlo, P.; Kaushik, A.K.; Arruda, E.M.; Waas, A.M.; Shim, B.S.; Xu, J; Nandivada, H.; Pumplin, B.G.; Lahann, J.; Ramamoorthy A.; Kotov, N.A. *Science* **2007**, 318, 80-83.

17. Lee, D.; Omolade; D. Cohen; R.E.; Rubner, M.F. *Chemistry of Materials* **2007**, 19, 1427-1433.

18. Bravo, J.; Zhai, J.; Wu, Z.; Cohen, R.E.; Rubner, M.F. *Langmuir* **2007**, 23, 7293-7298.

19. Shorlin, K.; de Bruyn, J. *Physical Review E* **2000**, 61, 6950-6957.

20. Singh, K.; Tirumkudulu, M.S. *Physical Review Letters* **2007**, 98, 1-4.

21. Xu, P.; Mujumdar, A.S.; Yu, B. *Drying Technology* **2009**, 27, 636-652.

Substrate	Rating	Nominal Pore Size (nm)	MWCO KDa	Surface Wettability	Surface Charge	Wetting Chemistry	Supported/ Unsupported
Omega PES 100	UF		100	**Hydrophobic**	Slightly Negative	None	Supported
Omega PES 300	UF		300	**Hydrophobic**	Slightly Negative	None	Supported
Omega PES 500	UF		500	**Hydrophobic**	Slightly Negative	None	Supported
Omega PES 1000	UF		1000	**Hydrophobic**	Slightly Negative	None	Supported
Nylon AN-15	MF	100		Hydrophilic	Positive	None	Unsupported
Nylon AN-25	MF	150		Hydrophilic	Positive	None	Unsupported
Supor-100 (P/N: 80610) PES	MF	100		Very Hydrophilic	Neutral	WE1(PVP K-90)	Unsupported
Supor-100H Thin (P/N: 80529) PES	MF	100		**Hydrophobic**	Neutral	None	Unsupported
AASupor-200 (P/N: 80704) PES	MF	200		Hydrophilic	Highly Positive	WE2 – PEI polyethylenimine	Unsupported
Supor-200WE4 (P/N: 80542N) PES	MF	200		Hydrophilic	Neutral	WE4 (Methacrylate)	Unsupported
Supor-200 (P/N: 80700) PES	MF	200		Very Hydrophilic	Neutral	WE1	Unsupported
PCTE	MF	30		Hydrophilic	Neutral	PVP	Unsupported
PCTE	MF	50		Hydrophilic	Neutral	PVP	Unsupported
PCTE	MF	80		Hydrophilic	Neutral	PVP	Unsupported
PCTE	MF	100		Hydrophilic	Neutral	PVP	Unsupported
PCTE	MF	200		Hydrophilic	Neutral	PVP	Unsupported
SPEES 10	UF		10	Hydrophilic	Negative	None	Unsupported
SPEES 100	UF		100	Hydrophilic	Negative	None	Unsupported

Note 1: All the information about the substrates was obtained directly from the membrane manufacturers (Pall Corporation and Whatman).
Note 2: PVP= polyvinylpirrolidone.

Table 1-1. *Summary of all substrates employed for fabrication of TFC membranes and their properties.*

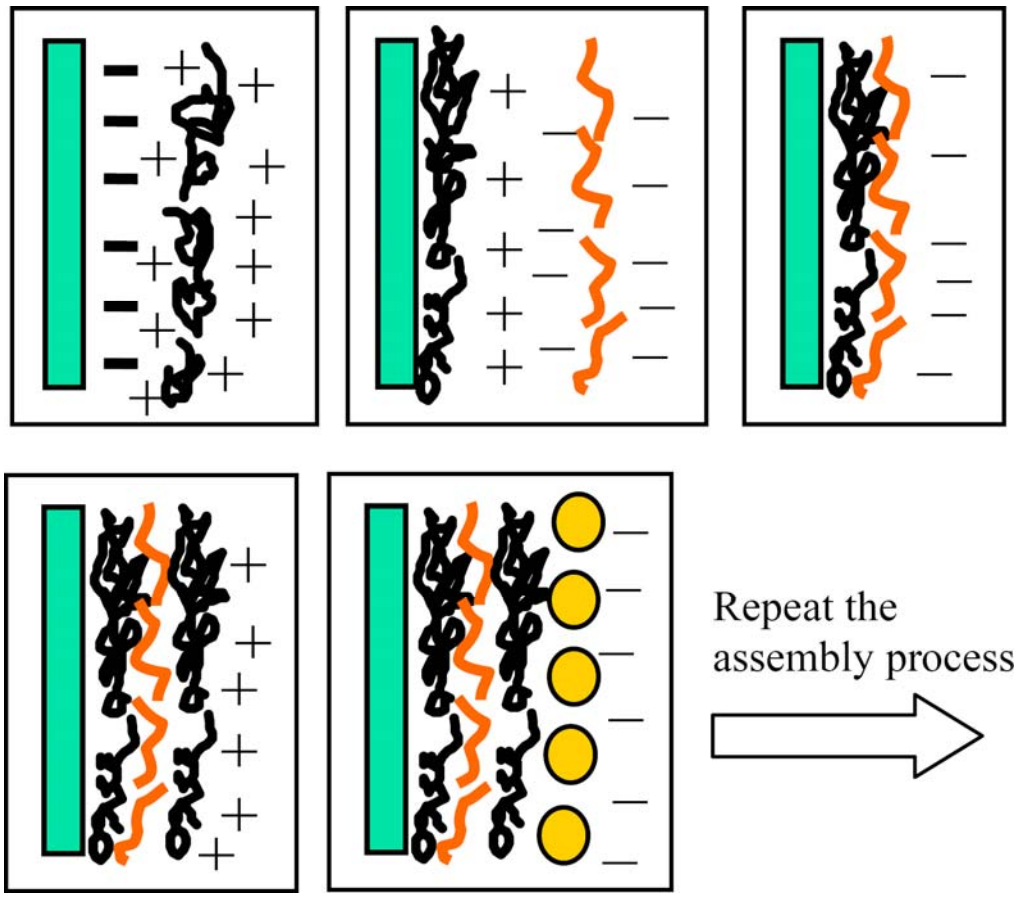

Figure 1-1. *Schematic of a typical LbL process. Green indicates the substrate, black and orange indicate the polyelectrolyte layers and yellow indicates nanoparticles. In this work, polyelectrolytes are only used to initiate deposition; the deposited layer after the initial few polyelectrolyte layers are nanoparticle only.*

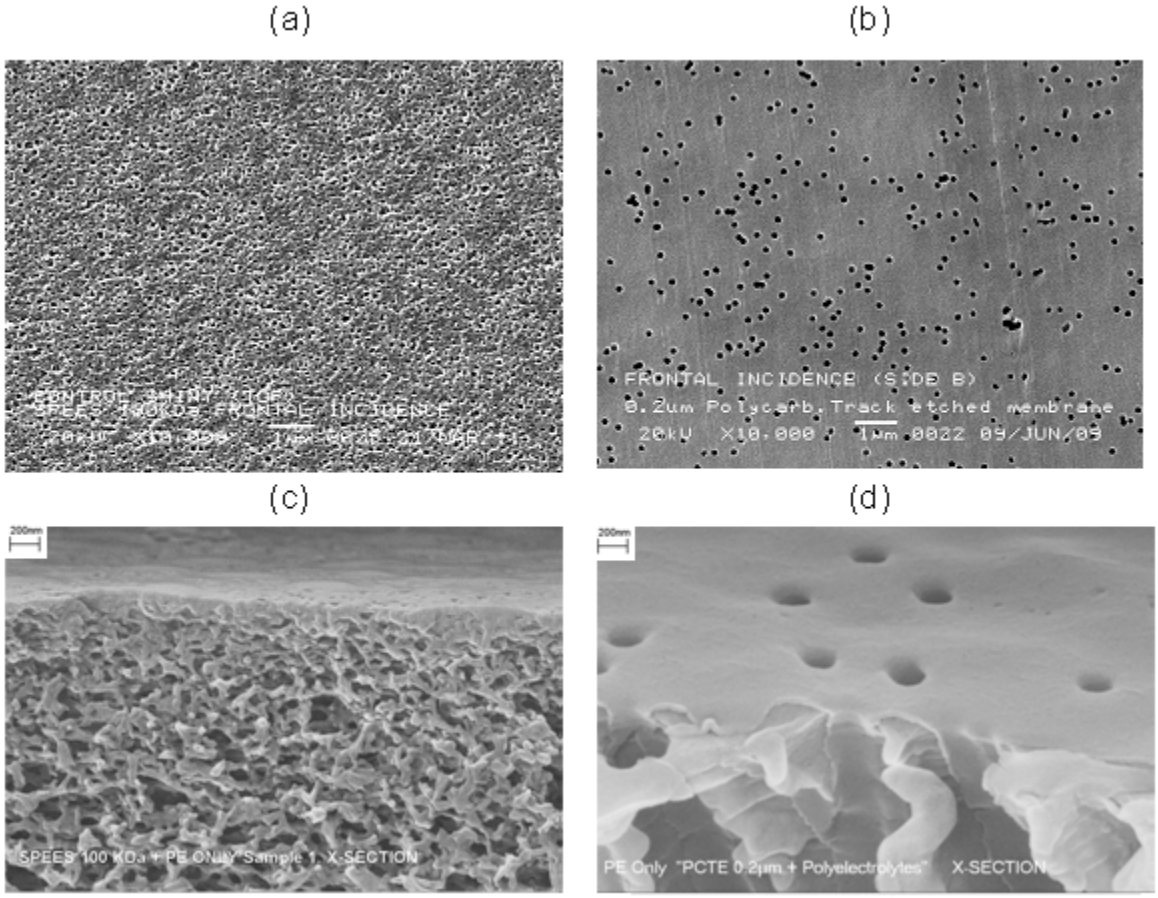

Figure 1-2. *Representative SEMs of uncoated and polyelectrolyte only coated supports. (a) Frontal incidence SEM of uncoated SPEES 100 KDa membrane; (b) Frontal incidence SEM of uncoated PCTE 0.2 µm membrane; (c) and (d) SEM of fracture surface cross sections of SPEES 100 KDa and PCTE 0.2 µm membranes, respectively, surface modified by LbL with only polyelectrolytes (PAA & PAH). The precursor layer, whose thickness ranges between 15-20 nm, is visible as a thin "veil" over the membrane surface that does not completely block the pore structure.*

(a)

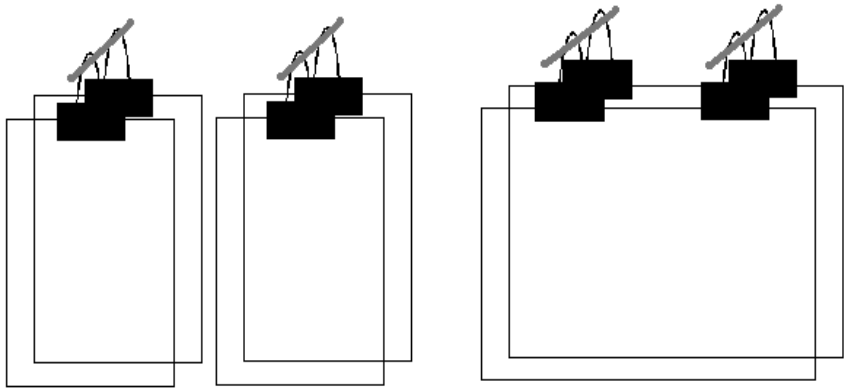

(b)

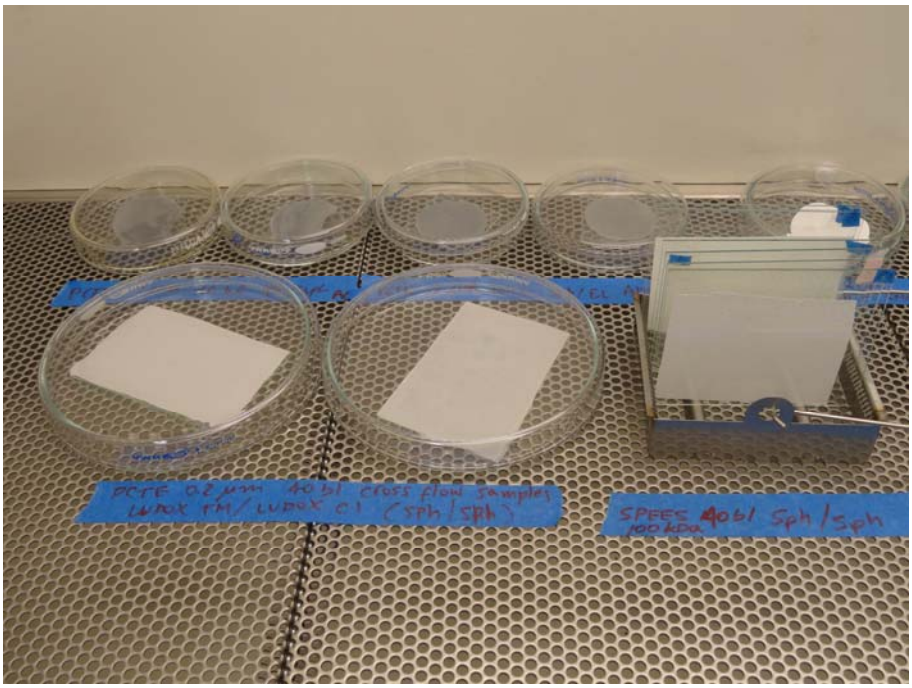

Figure 1-3. *(a) Schematic of the glass holder arrangement permitting dipping of multiple samples in the programmable dipper. (b) TFC membrane samples adhered to holders drying in a laminar flow hood awaiting analysis.*

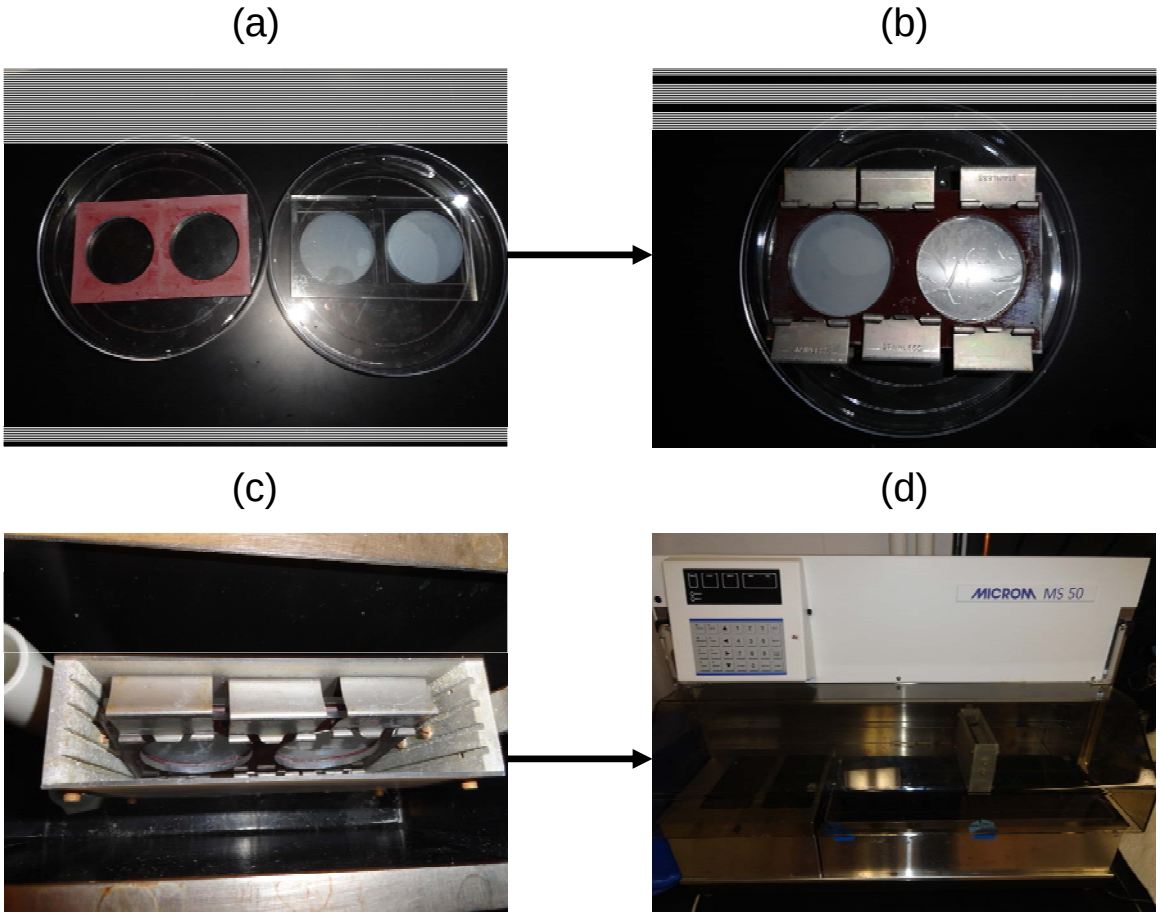

Figure 1-4. *Sequence of steps for sample loading onto frame holders. (a) Placement of samples on open frame, (b) sealing with clamps, (c) placement in basket slide stainer and (d) LbL deposition in the programmable dipper.*

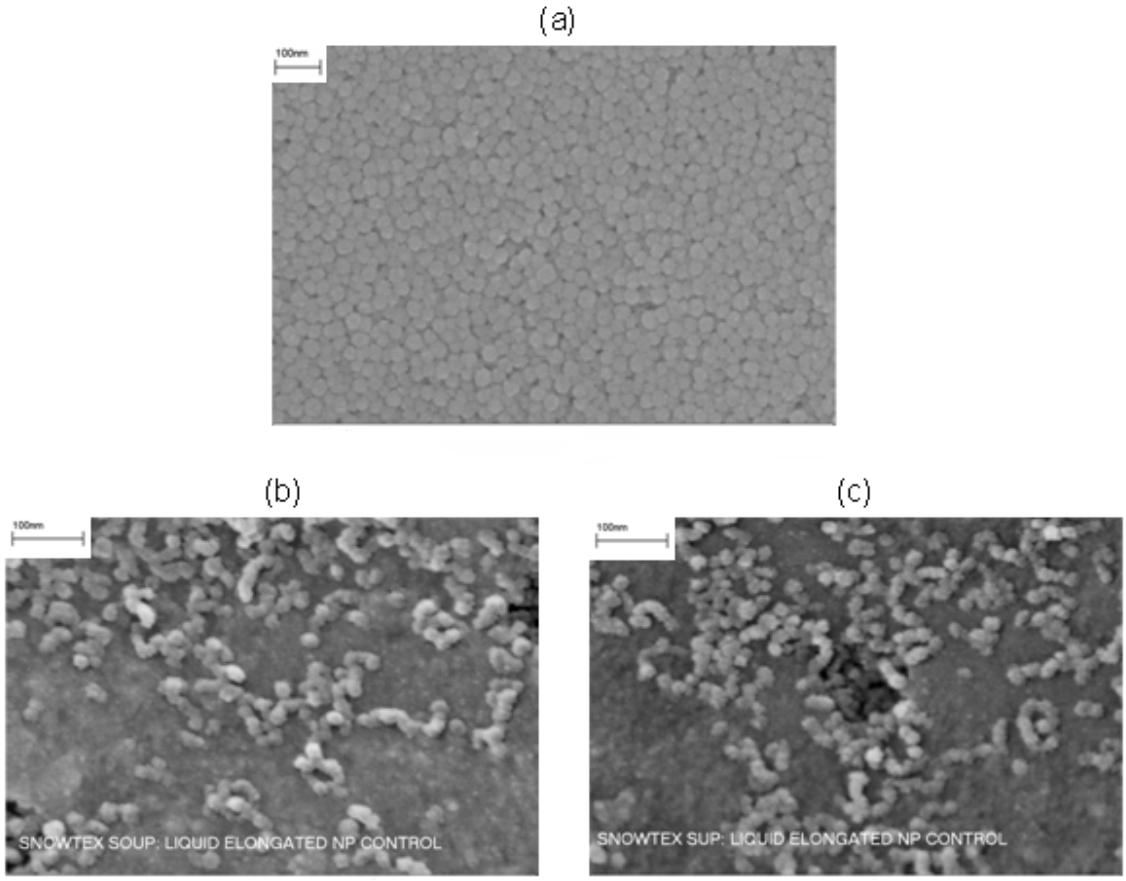

Figure 1-5. *(a) Frontal incidence SEM image of spherical Ludox TM-40 nanoparticles on coated glass substrate. The nanoparticles appear fairly uniform with a particle size diameter of 25-30 nm; (b) and (c) Frontal incidence SEM image of two different anionic silica nanoparticles (Snowtex SOUP and Snowtex SUP) respectively on membrane substrate. They are elongated and appear to be short chains of roughly spherical particles 10-15 nm in diameter and 2-10 strings together in length.*

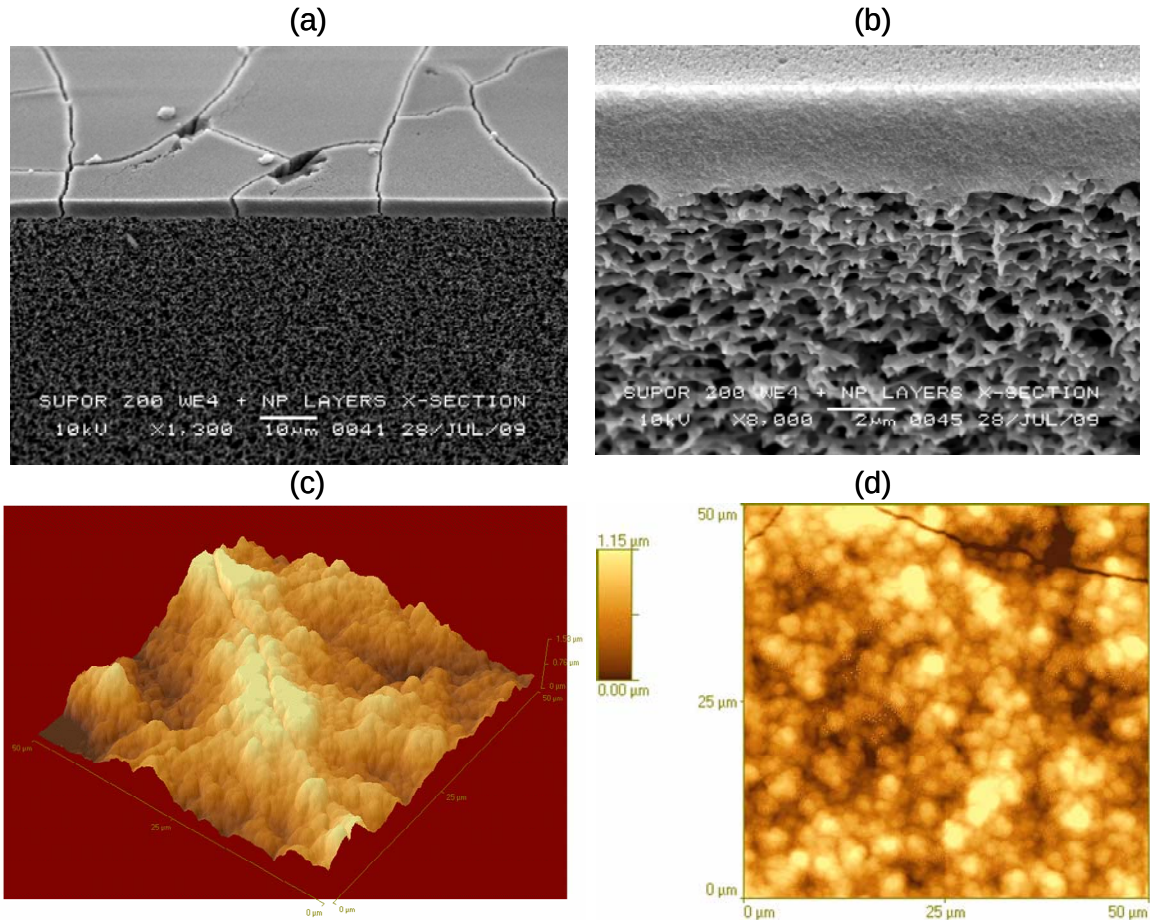

Figure 1-6. *(a) and (b) Representative cross section SEMs of Supor 200 WE4 - 200 bl - Ludox CL(+)/Ludox TM40(-) at different magnifications. Note visually sharp interface between deposited layer and substrate and the surface cracking. (c) 3D AFM image of the same TFC along a crack edge. Notice the raised surface crack along the crack contour; (d) 2D AFM of the same composite showing surface cracking.*

(a)

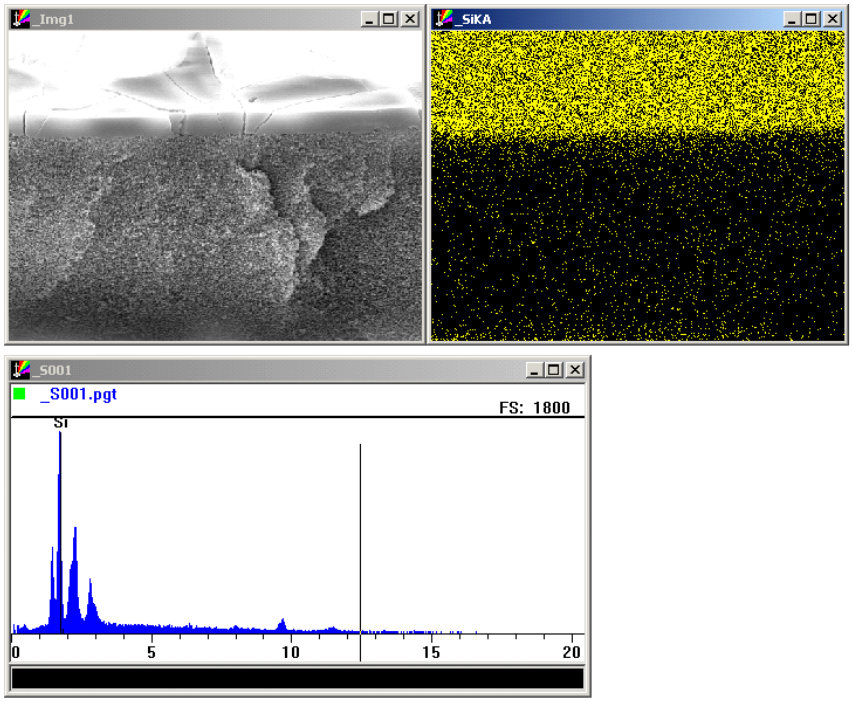
_Img1
_SiKA
_S001
_S001.pgt
FS: 1800
Si
0
5
10
15
20

(b)

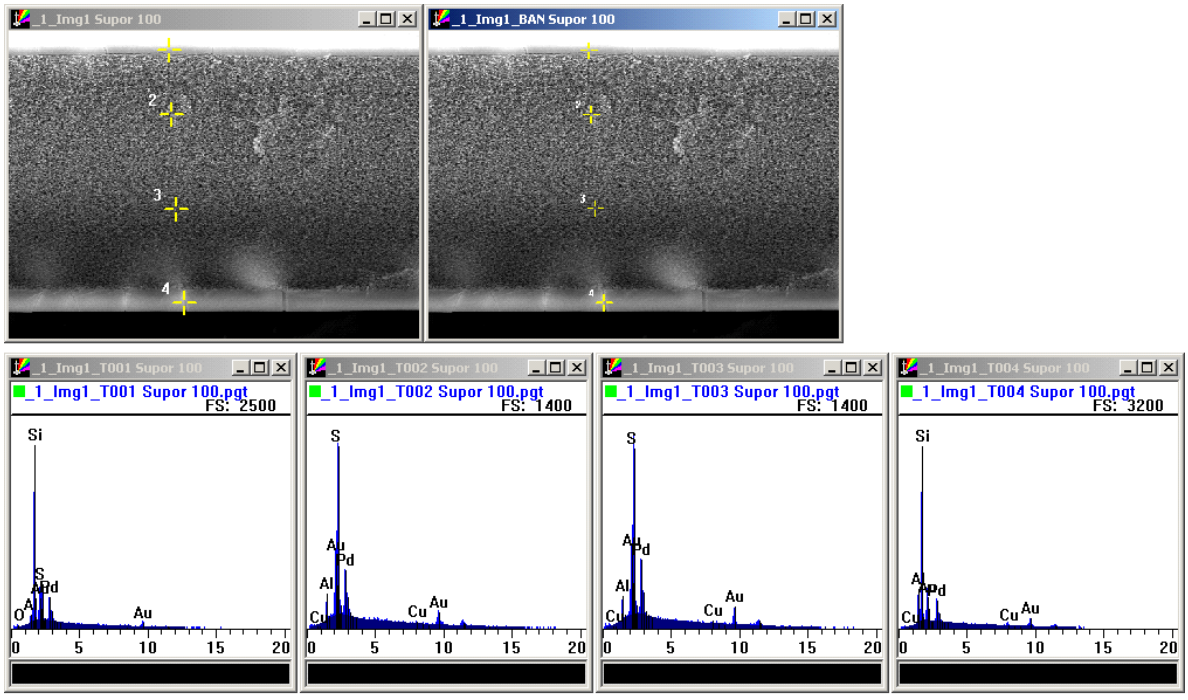
_1_Img1 Supor 100
_1_Img1_BAN Supor 100
2
3
4
_1_Img1_T001 Supor 100
_1_Img1_T001 Supor 100.pgt
FS: 2500
Si
S
Al
Pd
O
Au
_1_Img1_T002 Supor 100
_1_Img1_T002 Supor 100.pgt
FS: 1400
S
Au
Pd
Al
Cu
Au
_1_Img1_T003 Supor 100
_1_Img1_T003 Supor 100.pgt
FS: 1400
S
Au
Pd
Al
Cu
Au
_1_Img1_T004 Supor 100
_1_Img1_T004 Supor 100.pgt
FS: 3200
Si
Al
Pd
Cu
Au
0
5
10
15
20

Figure 1-7. *Representative cross section SEMs of Supor 100 H Thin - 200 bl - Ludox CL(+)/Ludox TM40(-) for EDX analysis. (a) Qualitative analysis of silica distribution (represented in yellow). The analysis indicates that most of the nanoparticles remain on the membrane surface with minimal intrusion into the porous substructure. The upper left image shows the cross section SEM selected for qualitative EDX at 1200 X; the upper right shows the silica elemental analysis for the image on the upper left; the lower left indicates the qualitative sample chemical elemental profile. (b) Quantitative elemental analysis across a TFC thickness for the same composite shown in (a), indicating a silica ratio of 50 between the surface and porous interior to within a resolution of 0.4 μm/pixel. The upper left and right images are identical cross section SEMs at 1100 X signaling the spots selected for analysis across the TFC thickness. The sequence of scans shown below represents the chemical elemental profile analysis of each spot selected.*

(a)

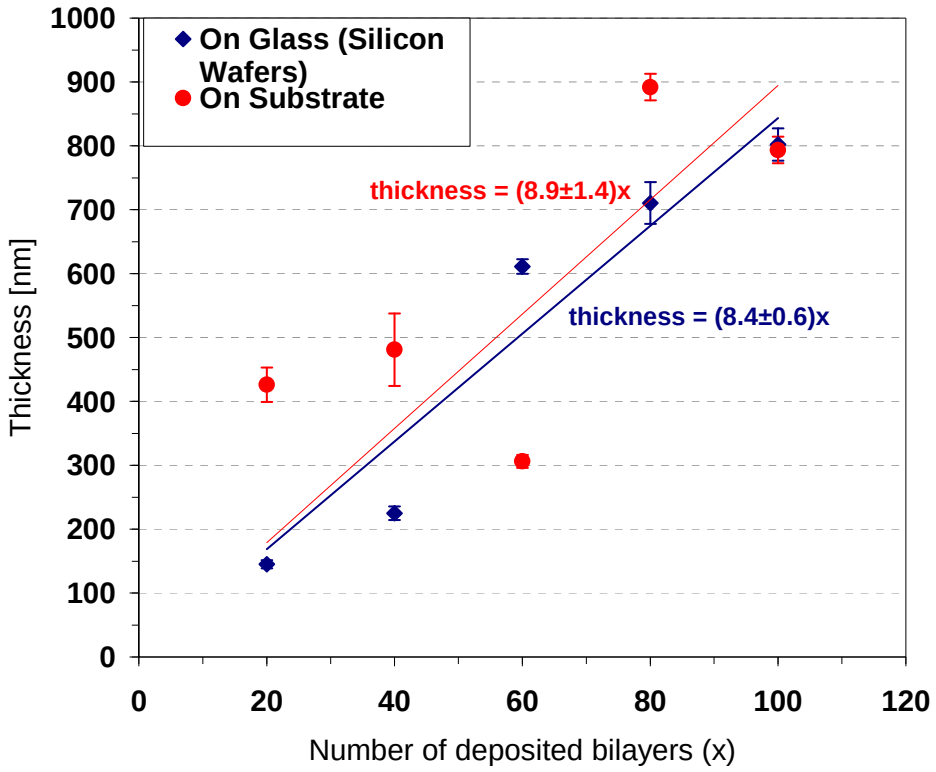
On Glass (Silicon Wafers)
On Substrate
thickness = (8.9±1.4)x
thickness = (8.4±0.6)x
Thickness [nm]
Number of deposited bilayers (x)
0
100
200
300
400
500
600
700
800
900
1000
0
20
40
60
80
100
120

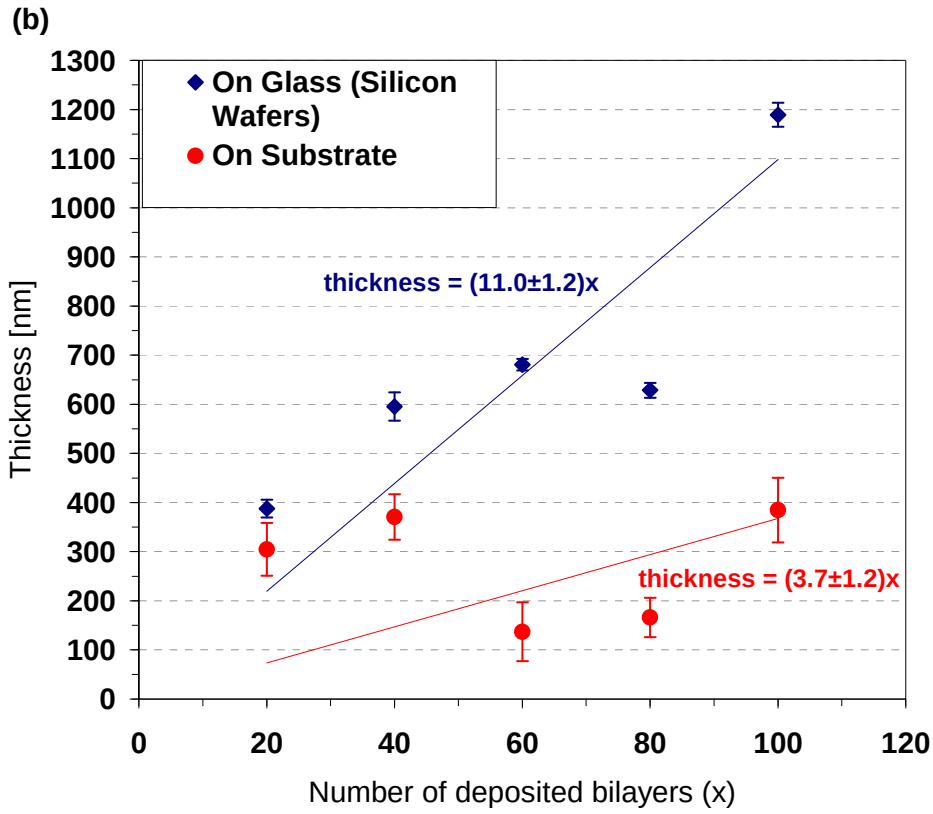

Figure 1-8. *Thickness of LbL deposit versus number of bilayers deposited on silicon wafers and on a porous substrate (PCTE 0.03 μm) for (a) spherical/spherical Ludox CL(+)/Ludox TM40(-) and (b) spherical/elongated Ludox(+) CL/Snowtex UP(-) nanoparticle deposition. The slope values are shown with 95% confidence limits. The lines in (a) and (b) are regression fits constrained to the origin.*

(a)

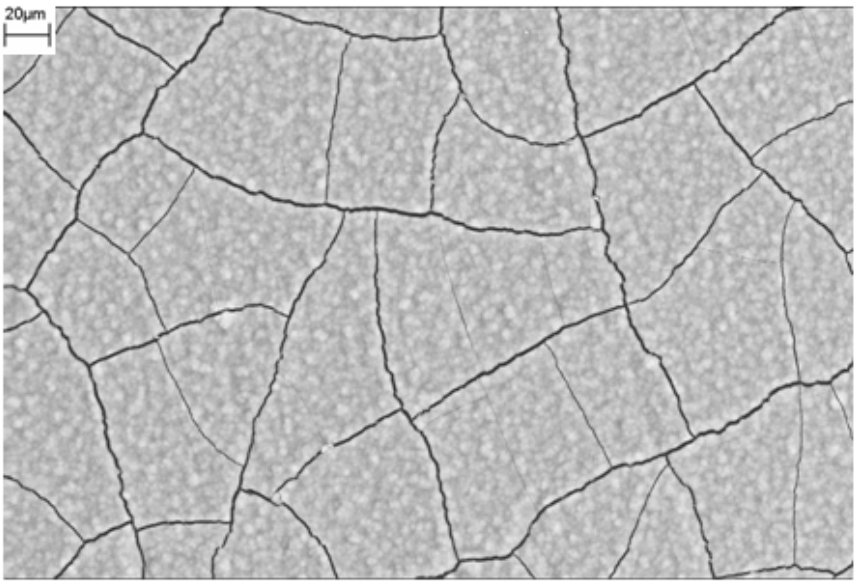

(b)

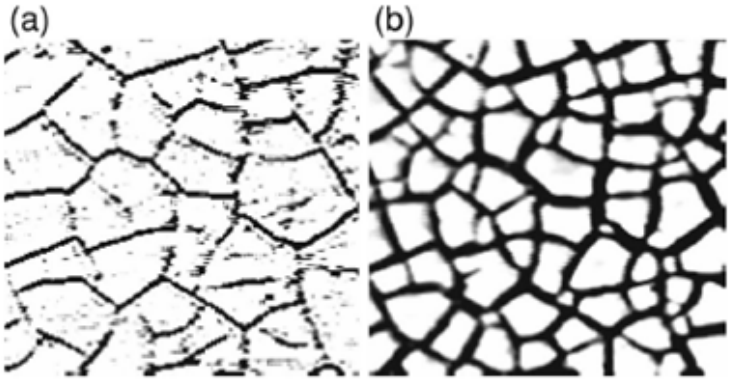

FIG. 3. A portion of the crack pattern forming in a layer 1.31 ±0.03 mm thick. Sand has been added to the layer, and the substrate coated with teflon. At least five triplet junctions, formed when three cracks nucleated at a point, are visible in the images. The area shown is 5.7×5.5 cm^2. (a) 41 h into the run. (b) 56 h into the run.

Figure 1-9. *Representative SEM micrograph of: (a) Topology of drying-induced cracking of LbL deposited nanoparticle layer on PES substrate. Note a characteristic length of ~O(10^2 μm); (b) Analogous cracking in dried sand layers[20] exhibiting much larger characteristic length scale ~O(10^4 μm).*

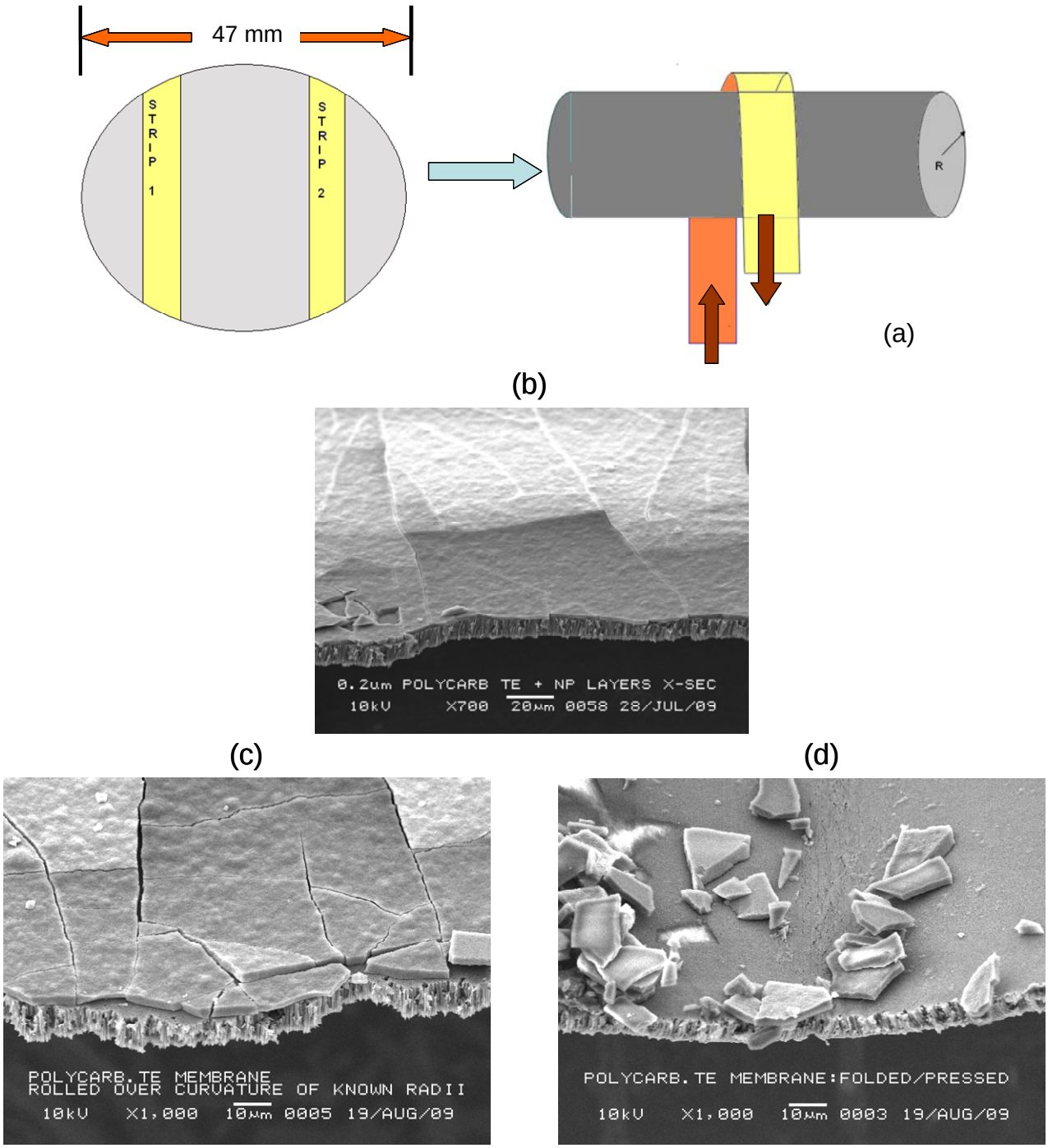

Figure 1-10. *(a) Schematic of "rolling experiment" showing how flexible strips were cut from a TFC membrane and bent over a cylinder of known radius R= 2.94 mm; (b) Control - Fracture surface cross section SEM of PCTE 0.2 µm 40 bl Ludox CL(+)/Ludox TM40(-); Same TFC sample after: (c) Rolling mechanical bending and (d) Folding and pressing mechanical bending.*

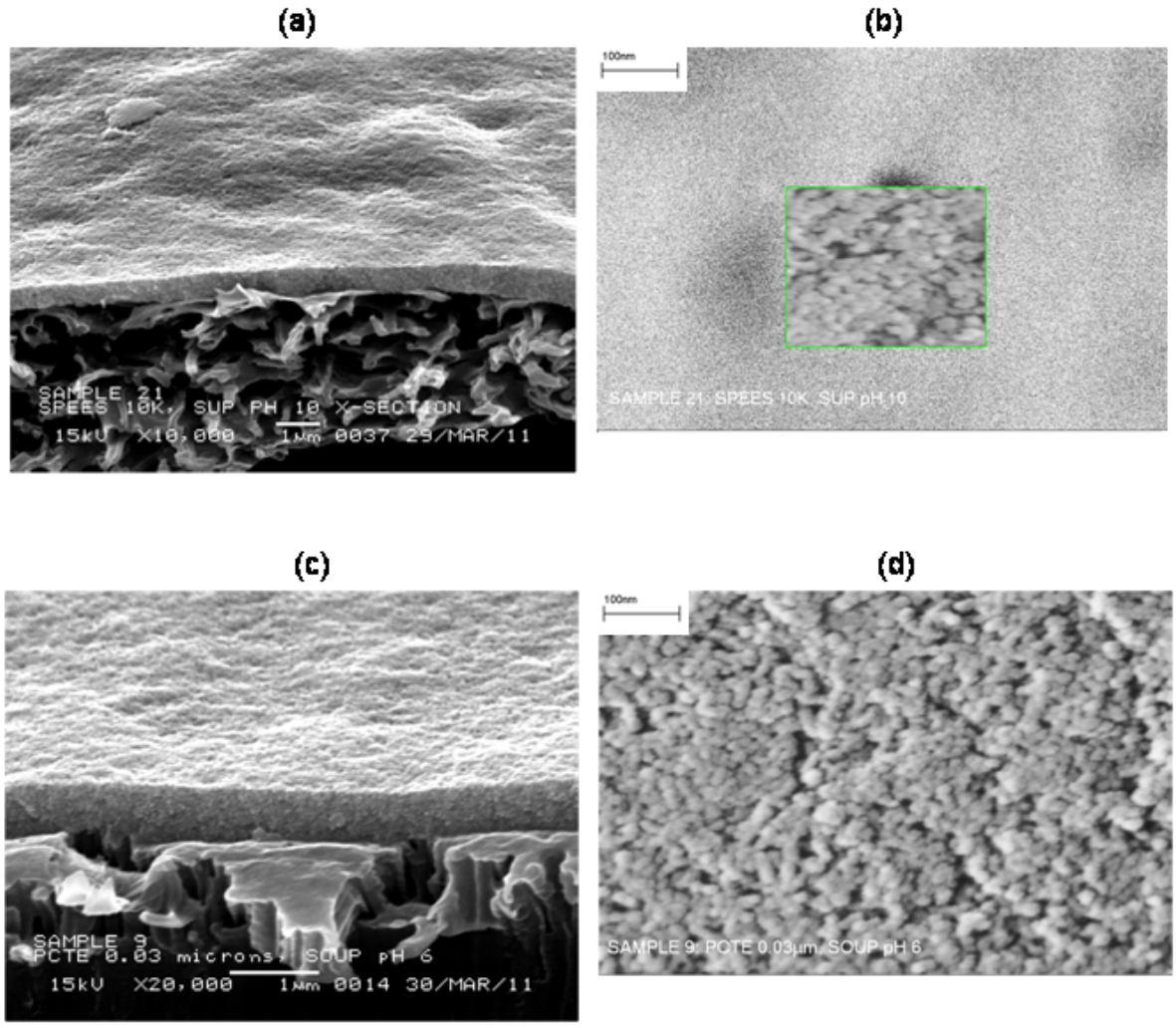

Figure 1-11. *SEMs demonstrating crack free TFC fabrication of: (a)and (b) SEM of fracture surface cross section and frontal incidence of SPEES 10 KDa - 40 bl - Ludox CL(+)/Snowtex SUP(-) respectively (c) and (d) Fracture surface cross section and frontal incidence SEM of PCTE 0.03 µm - 60 bl - Ludox CL(+)/Snowtex SOUP(-) respectively.*

Appendix-A

Sample program for the dipper:

This is an example of nanoparticle deposition of 40 bilayers using the dipper.exe file installed in the control computer.

<C>reate a series of programs to run

- How many programs do you want to run? 2
- Which one is first? 1
- How many times do you want to run this program? 40
- What program is next? 2
- How many times do you want to run this program? 1
- How many times do you want to run the series? 1

<S>how series of programs

<R>un

Chapter 2. Hydrodynamic Permeability of Nanoparticle Surface Modified, Thin Film Composite Membranes

Abstract

Layer by Layer (LbL) deposition of primarily inorganic (silica) nanoparticles enabled surface modification of polymeric micro and ultrafiltration (MF/UF) membranes to produce thin film composites (TFC) with potential nanofiltration (NF) and reverse osmosis (RO) capabilities. The hydrodynamic permeability of these TFC membranes is measured to evaluate their performance under typical NF operating conditions using dead-end permeation experiments. Several combinations of MF/UF membrane substrates and LbL deposited nanoparticle surface layers, including both spherical (cationic/anionic) and elongated (anionic) silica nanoparticles were tried and compared quantitatively with realistic hydrodynamic models, with favorable results. For track etched polycarbonate MF substrates, surface modification causes a permeability reduction of approximately two orders of magnitude with respect to the bare substrates, to values comparable to those for typical commercial NF membranes. Good quantitative agreement with hydrodynamic models with no adjustable parameters was also established for this case, providing indirect confirmation that the LbL deposited surface layers are largely defect (crack) free. Imaging of our TFC membranes after permeation tests confirmed that no significant mechanical damage resulted, indicating integrity and robustness of the LbL deposited surface layers in typical applications. The work supports that nanoparticle based LbL surface modification of MF/UF membranes can produce filtration quality media for important water purification applications, such as nanofiltration (NF) softening processes, natural organic matter (NOM) elimination and possibly reverse osmosis (RO) desalination.

2.1 Introduction

Multi-layer thin films consisting of a porous, nonselective support layer with a very thin selective barrier layer on top are a very important type of separation membranes, frequently referred as a thin film composite (TFC) membrane. The "Loeb-Sourirajan" reverse osmosis membrane, made by a phase inversion process from cellulose acetate and patented in 1960, was one of the first commercially viable TFC membranes.[1-3] Relatively new TFC membranes can combine organic and inorganic materials and now serve a number of technologies. TFC membrane properties can be tailored over a significant range for many applications including fuel cells and batteries, gas and liquid separations and various water purification operations.[4-6] The top selective skin layer and bottom support are complementary and can be optimized independently[4] and this ability is a significant advantage in membrane technology. As a result, modern TFC membranes for separations and water purification can provide high selectivity and flux, thermal and chemical stability and even self-cleaning properties. [4, 7-10]

The main focus of this work is the characterization of novel TFC membranes for the water purification applications nanofiltration (NF) and reverse osmosis (RO). These are prepared by layer-by-layer (LbL) surface modification of existing micro or ultrafiltration (MF/UF) membranes. The LbL process we used deposits a thin, selective layer comprised mainly of inorganic nanoparticles atop the existing porous MF/UF membranes (see Chapter 1 for details). We report here on the hydrodynamic permeability of these composite membranes, that is, their permeability against pure, deionized water, under typical NF/RO operating conditions. These measurements provide a necessary test of the viability of the membranes for NF/RO applications. Firstly, they determine an important practical figure of merit; namely the water flux or "permeance" through the LbL modified membranes, under typical NF/RO operating parameters.

These values must be in the ranges of $7.0*10^{-4}$-$3.5*10^{-3}$ cm/s (0.6-3.0 $m^3/m^2 \cdot d$), $9.3*10^{-4}$-$2.3*10^{-3}$ cm/s (0.8-2.0 $m^3/m^2 \cdot d$) and $5.8*10^{-5}$-$1.2*10^{-3}$ cm/s (0.06-1.0 $m^3/m^2 \cdot d$) for NF, brackish water RO and seawater RO applications, respectively, for the membranes to provide a viable new filtration media.[7, 11, 12] Secondly, through a quantitative comparison with appropriate hydrodynamic models, our permeability measurements establish that the LbL deposited nanoparticles surface layers, are largely crack-free, i.e. that there is no detectible hydrodynamic "shunting" or "bypassing" that would accompany such cracking.

Further, while such measurements do not directly establish the selectivity of the membranes against typical suspended contaminants in pressure driven filtration processes, they can provide indications of such capabilities. For example, it has been demonstrated for many UF membranes, including TFC membranes similar to ours fabricated by depositing and stabilizing micron sized latex particles onto MF membrane porous supports, a strong "trade off" correlation between the 95% rejection molecular weight cut-off (MWCO) of dextran standards and water permeabilities.[8, 9] A similar relationship is evident for NF and RO membranes between water permeability and salt rejection characteristics.[13] Moreover, water permeability measurements provide an intrinsic membrane transport property, independent of the membrane thickness, which is very sensitive to the membrane pore structure and internal surface chemistry. For example, hydrodynamic permeability can distinguish the effect of a very thin hydrophilic polymer coating, such as polydopamine, on the internal surface of normally hydrophobic NF and RO membranes.[14, 15] In another example, Ulbricht reported the sensitivity of the permeability of track etched UF membranes to the coating of their internal pore structure via LbL deposition of polyelectrolyte polymers. It decreases with the number of bilayers deposited on the internal pore walls, enabling estimation of the change in the average pore radius.[16]

2.2 Experimental

2.2.1 Materials

The materials for TFC membrane fabrication, detailed in Chapter 1, were used here as received. Poly(allylamine hydrochloride) (PAH, M_w = 56,000 Dalton), and Poly(acrylic acid) (PAA, M_w=100,000 Dalton, 35 wt% solution in water) were purchased from Sigma Aldrich (St. Louis, MO). Ludox® CL colloidal spherical cationic silica nanoparticles (30 wt% solution in water; 15 nm average diameter), and Ludox® TM-40 colloidal spherical anionic silica nanoparticles (40 wt% solution in water; 25 nm average diameter) were purchased from Sigma Aldrich (St. Louis, MO); Snowtex®-UP (9-15 nm width, 40-100 nm length) basic colloidal anionic elongated silica nanoparticles and Snowtex®-OUP (9-15 nm width, 40-100 nm length) acidic colloidal anionic elongated silica nanoparticles were obtained through Nissan Chemical America (Houston, TX). The flat sheet membrane supports used were Nuclepore® Polycarbonate Track-Etch (PCTE) membranes from Whatman (Kent, UK) with nominal pore sizes of 0.03 and 0.2 μm and Sulfonated Poly etherethersulfone (SPEES®) with a dextran standards molecular weight "cut-off" (MWCO) of 100 KDa from Pall Corporation (Port Washington, NY). Millipore Q-Gard® 1 and Progard® 2 (Billerica, MA) systems provided deionized water with a resistivity of 18.2 MΩ·cm @ 25 °C which was used for all experiments reported in this work. A Denver Instrument Company (Arvada, CO) TR-64 analytical balance (±0.1 mg resolution) was used to determine the density of the permeate, and a Mitutoyo Digimatic Caliper Absolute CD-6" CSX (Kanagawa, Japan) (±0.01 mm resolution and ±0.02 mm accuracy) was employed to determine membrane and permeation cell dimensions.

2.2.2 TFC Membrane Preparation

The preparation of TFC membranes via LbL deposition was described in detail in Chapter 1. The supports used were coated by LbL using a robotic dipper on only one side of the flat sheet membrane, that is, the dip coating method using the special mounting frames described in Chapter 1 was employed. The samples prepared for permeability testing are summarized in Table 2-1. The deposited nanoparticle layer thickness varied from about 200 nm for 40 bilayers to about 800 nm for 100 bilayers for the spherical/spherical nanoparticles case and 600 nm for 40 bilayers to about 1200 nm for 100 bilayers for the spherical/elongated nanoparticles case. All the TFC samples reported on this work were post treated by autoclaving at 121ºC for approximately one hour, as described in Chapter 1.

2.2.3 Dead-end Permeation

The water flux or "permeance", and the hydrodynamic permeability of the bare supports and of the TFC membranes made from them (see Table 2-1) were measured using a dead-end permeation set up. Figure 2-1 (a) shows a schematic. The measurements were accomplished by applying a fixed pressure to the upstream side of the membrane, and weighing the amount of permeate thereafter. The permeate weighing was conducted using an Ohaus Adventurer™ Pro AV8101CU Precision Balance from Ohaus (Parsippany, NJ) scale (±0.1 g resolution) connected to a desktop computer with WinWedge data acquisition software from Tal Tech (Philadelphia, PA). A key component of the set up is the membrane holder or permeation cell which houses the membrane. For each measurement, a 47 mm circular membrane was carefully aligned in the cell base wetted with DI water. All the circuit's valves were closed before starting an experiment (see figures 2-1 (a) and (b)). The cell is tightly closed and the water reservoir filled with DI water and sealed with clamps. The air regulator valve is then opened, and the remaining valves are opened

sequentially from the top end (i.e. the reservoir end) of the apparatus. One then sets the cell's initial upstream pressure to about 15 psi and triggers the software to start capturing data continuously. Typically, only about 40-50 grams of water flow was needed to acquire enough data to determine a permeability value accurately at a given upstream pressure. Then, a new larger upstream pressure could be set, and the experiment repeated. The upstream pressure was increased to the next value with the regulator by about 5 psi. This process was repeated until achieving the final (highest) pressure desired (about 60 psi). To finish a measurement sequence, the pressure is reduced to ambient and the membrane removed and stored for later microscopy tests.

The permeability K is given by,

$$\mathrm{K} = \frac{Jl}{\Delta P}[=]\frac{cm^3 s}{g} \tag{2-1}$$

in which, J corresponds to the liquid flux at steady state (SS) conditions; l is the membrane thickness and ΔP is the pressure drop across the permeation cell. The data acquisition continuously records the permeate mass $m(t)$ which allows one to obtain the flux J through the relation,

$$J = \frac{1}{\rho A}\frac{dm}{dt} \tag{2-2}$$

where ρ is the permeate density (ρ=0.974 g/cm^3), and A is the cell effective filtration area dictated by the upstream pressurized area in the permeation cell (effective diameter of the cell D= 4.20 cm; A=13.85 cm^2). The values of $\frac{dm}{dt}$ were obtained by a linear regression on $m(t)$ constrained to the origin for each value of ΔP attempted.

In Eq. 2-1, ΔP values were taken as the upstream gauge pressure read from a Wika pressure gauge type 212.53 (Lawrenceville, GA), (0-60 psi range ±2.5% accuracy) installed in

the permeation cell. The thickness *l* for the substrates was determined with a Mitutoyo 547-400S Digimatic IDC Thickness Gauge Indicator (Kanagawa, Japan) (±0.001 mm resolution and ±0.004 mm accuracy) or the technical data sheets supplied by the manufacturer. For TFC's the coating layer thicknesses were obtained by NIS software applied to multiple SEM cross section microscopy images. The TFC total thickness corresponds to the addition of the substrate and coating layer thicknesses. A propagation of error analysis shows that the uncertainty in the K values given by Equations 2-1 and 2-2 is determined mainly by the thickness (*l*) and pressure drop (ΔP).

2.3 Results and Discussion

2.3.1 Hydrodynamic Permeability of Substrates and TFC Membranes

The flux and the hydrodynamic permeability of the substrates without surface modification were tested first. Representative data are shown in Figure 2-2 for the substrates PCTE 0.2 μm and SPEES 100 KDa. The error bars shown give the repeatability around the average based on measurements from 3-5 samples for all the results reported. Figure 2-2 (a) shows the flux *J* as a function of the pressure drop *(ΔP)* for the two substrates. Linear relationships are observed, as expected. Figure 2-2 (b) shows the permeability values (K) of the same order of magnitude 10^{-10} [$cm^3 \cdot s/g$] for both substrates, although the value for the SPEES is between 1.4-2.4 times that of the PCTE sample. The flux for the PCTE samples is more than three times higher than that the SPPES samples. The permeability values for the PCTE membranes are reasonably constant with the applied pressure drop, as expected. There is a minor increment in K of approximately 10% as ΔP increases from 15 to 45 psi. Interestingly, the mean K values for the SPEES samples increase with ΔP by 94% as ΔP increases from 15 to 45 psi. While the reason for this reproducible effect is not entirely clear, it likely results from reversible

mechanical deformation of the complex, asymmetric open-cell pore structure of the SPEES substrates under the applied pressure drop, which "opens" the pore structure somewhat.

Figure 2-3 shows representative data for K after modifying one surface of both, PCTE and SPEES, with the same, very thin polyelectrolyte layer (2.5 deposited bilayers of PAA and PAH atop the membrane surface) as described in Chapter 1. Recall this LbL pre-coating of polyelectrolytes establishes a reproducible surface charge, initializing reliable subsequent LbL coating by charged nanoparticles. The experimental conditions and procedure for determining K were identical to those used for bare substrates. The results indicate a significant permeability decrease because of the coating for the SPEES substrates by an increasing factor from 14 to 42 times as ΔP increases from 15 to 45 psi, but much less of a change for the PCTE substrates, which show only a minor decrease in K (average 46%). Microscopy (see Figure 1-2 (c) and (d)) reveals that the polyelectrolyte pre-coat blocks a significant portion of the small pores on the UF rated SPEES support, which is an asymmetric membrane with a very broad pore size distribution and a relatively small mean pore size. The much smaller effect observed on the MF rated PCTE supports, which is symmetric and has a very narrow pore size distribution with a relatively large pore size is consistent with the microscopy showing a thin pre-coat layer which does not significantly block the majority of pores.

The TFC membranes were then tested for both substrates modified with the polyelectrolyte layer and with 40, 60, 80 and 100 bilayers of both Ludox CL/Ludox TM (cationic/anionic) spherical/spherical and Ludox CL/Snowtex UP (cationic/anionic) spherical/elongated silica nanoparticle combinations. The results for the TFCs using MF rated PCTE supports indicate a *significant* reduction of hydrodynamic permeability K after the nanoparticle deposition in all cases for both nanoparticle combinations. Figure 2-4 summarizes

the results. Nanoparticle surface modification results in a permeability reduction of almost two orders of magnitude with respect to the bare substrates for TFC's made with PCTE supports and nearly as much with respect to the value resulting from PE coatings alone. The results were *different* for the SPEES substrates where no significant reduction in K beyond that from the PE pre-coat occurred with nanoparticle addition, for either nanoparticle combination and from any number of bilayers added in the range studied. The values of K obtained in this case are very much in line with the significantly reduced ones measured for PE only surface modification as can be observed in Figure 2-5. In brief, the nanoparticle deposited layer controls the hydraulics for the MF rated PCTE substrate based TFCs, while this is not the case for the UF rated SPEES substrate based TFCs.

The difference in results for these two substrates is surely related to their mean pore size and pore size distribution. The MF rated PCTE membranes have a relatively large mean pore size (0.22 μm) and a very narrow size distribution. The PE pre-coat does little to alter the pore characteristics, as seen qualitatively by microscopy (Figure 1-2 (c) and (d)) and quantitatively by K being reduced relatively weakly by the PE coat. Clearly, subsequent depositions of nanoparticle layers alter the effective pore size significantly, enough to cause a dramatic reduction in K of more than an order of magnitude.

That this is not the case for SPEES substrates follows from its smaller mean pore size (100 KDa dextran standards MWCO would correspond to approximately 0.01-0.02 μm pore size based on our high resolution SEM and its 95 Å radius of gyration R_g[19], significantly smaller than 0.2 μm for the PCTE substrate) and broad pore size distribution. The microscopy indicates that most of the SPEES surface pores get blocked by the initial PE coating except for a few large

pores (Figure 1-2 (c)). Those that remain are not far above the mean nanoparticle size, suggesting a minimal effect of nanoparticle coating on the hydraulic characteristics.

There does not seem to be a significant effect on the hydrodynamic permeability due to the introduction of elongated nanoparticles into the surface modification. Comparing Figure 2-4 (a) and (b) or Figure 2-5 (a) and (b) it is observed that for either substrate the measured values of K agree for the spherical/spherical and the spherical/elongated nanoparticle combinations.

Further, the data for both substrates suggests that for the (cationic/anionic) spherical/spherical nanoparticle case, there is a significant decline in permeability with the number of bilayers deposited (see Figure 2-6) to about 50% of its value. Linear regression fits of the data in Figure 2-6 give values of $(0.004\pm0.003)*10^{-11}$ [$cm^3 \cdot s/g$]/bilayer and $(0.027\pm0.002)*10^{-11}$ [$cm^3 \cdot s/g$]/bilayer for the PCTE and SPEES substrates respectively. For (cationic/anionic) spherical/elongated nanoparticle case, the average K values do not appear to show significant variance with the number of bilayers deposited in the range of 40 -100 bilayers.

2.3.2 Comparison with Theoretical Hydrodynamic Models

For the TFC membranes with PCTE supports, realistic hydrodynamic models can predict the membrane hydrodynamic permeability without adjustable parameters. Track etch symmetric membranes, such as the PCTE employed for this study, can be modeled realistically as parallel capillary tubes. The Hagen-Poiseuille equation dictates the pressure drop vs. flowrate through a cylindrical pore (Eq. 2-3). Solving the equation for the volumetric flow (q) and considering every track-etched pore as one of these cylinders, we can determine the flux, and therefore the permeability through the membrane, knowing the number of pores per unit of area determined from microscopy. Then, the permeability of the substrate denoted K_1 is determined using Equation 2-1. Hence,

$$q = \frac{\Delta P \pi r^4}{8\mu l}; J = \frac{nq}{A}; \mathrm{K}_1 = \frac{Jl}{\Delta P} \tag{2-3}$$

in which, r corresponds to the mean pore radius, μ is the fluid viscosity and $\left(\frac{n}{A}\right)$ is the number of pores per unit area.

Applying these relations we find the permeability, independent of the pressure drop (ΔP) and the membrane thickness (l), to be

$$\mathrm{K}_1 = \left(\frac{n}{A}\right)\frac{\pi r^4}{8\mu} \tag{2-4}$$

The results obtained using this model, without adjusting any parameters, indicate a permeability value of K_1=1.9*10^{-10} [cm^3·s/g] using an average pore diameter of 0.22 [μm] estimated by microscopy imaging and using the NIS imaging software on SEM micrographs of the PCTE membrane surfaces. This result agrees nearly with the quantitatively measured value (2.2*10^{-10} - 2.5*10^{-10} [cm^3·s/g])

The hydrodynamic influence of the deposited surface layer of nanoparticles can be modeled as an array of packed particles. Ergun's Equation[17] describes the flow through a packed bed of spheres:

$$\frac{\Delta P}{l} = \frac{J}{\mathrm{K}_2} = \frac{150(1-\varepsilon)^2 U\mu}{\varepsilon^3 \phi^2 D_p^2} + \frac{1.75(1-\varepsilon)U^2\rho}{\varepsilon^3 \phi D_p} \tag{2-5}$$

in which, ε corresponds to the void fraction, D_p is the bed packing particle size, ϕ corresponds to the particle sphericity, U is the fluid superficial velocity, ρ is the fluid density and μ is the fluid viscosity. Applying this model for example for a surface layer of 40 bilayers of Ludox spherical silica nanoparticles, using D_p of 20 nm, a void fraction of 0.545 and a sphericity of 1 the permeability of the nanoparticle coating K_2 is estimated to be K_2=1.5*10^{-12} [cm^3·s/g]. The

resulting hydrodynamic permeability of a TFC architecture K can be modeled as resistances in series[18]:

$$\frac{l}{\mathrm{K}} = \frac{l_1}{\mathrm{K}_1} + \frac{l_2}{\mathrm{K}_2} \tag{2-6}$$

where K_1 is the permeability of the substrate, K_2 is the permeability of the surface layer, l_1 and l_2 correspond to the substrate and surface layer thicknesses respectively; l is the TFC thickness.

As an example, using the values previously mentioned, one finds the permeability of a TFC membrane with the PCTE 0.2 μm substrate and 40 B-L coating of Ludox CL/Ludox TM (cationic/anionic) spherical/spherical silica nanoparticles of $K=2.7*10^{-11}$ [$cm^3 \cdot s/g$] which compares very well with the average $K=7.7*10^{-11}$ measured from experiments (See Figure 2-4 (a))

Comparing predicted values with the real measurements on PCTE based membranes, as showed in Figures 2-2 and 2-4, we observed near quantitative agreement for the bare substrate and the TFC membrane, which strongly suggest that the surface layers are largely defect (crack) free. If there were mechanical damage leading to cracks spanning the deposited layer, the permeability values for PCTE based membranes would be significantly higher from the predicted values.

Based on the resistances in series model described on Equation 2-6, it is possible to use this equation to predict the slopes shown on Figure 2-6, particularly regarding the spherical/spherical silica nanoparticles deposition case for both substrates employed.

From Equation 2-6, the permeability K is given by:

$$\mathrm{K} = \frac{l_1 + l_2}{\frac{l_1}{\mathrm{K}_1} + \frac{l_2}{\mathrm{K}_2}} \tag{2-7}$$

According to this result, the slope shown in Figure 2-6 is proportional to the derivative of this expression with respect to the surface layer thickness as follows,

$$\left(\frac{\partial \mathrm{K}}{\partial l_2}\right)_{l_1} = \frac{\frac{l_1}{\mathrm{K}_1} - \frac{l_1}{\mathrm{K}_2}}{\left(\frac{l_1}{\mathrm{K}_1} + \frac{l_2}{\mathrm{K}_2}\right)^2} = \left(\frac{\mathrm{K}}{l}\right)^2 l_1 \left(\frac{\mathrm{K}_2 - \mathrm{K}_1}{\mathrm{K}_1 \mathrm{K}_2}\right) < 0 \tag{2-8}$$

Since $K_2<K_1$, this result is negative in concordance to the slopes shown, particularly for the spherical/spherical case.

The proportionality to calculate the slope (m) is given by the following relation:

$$m = \left(\frac{\partial \mathrm{K}}{\partial l_2}\right)_{l_1} \left(\frac{\partial l_2}{\partial n}\right) \tag{2-9}$$

Hence, n corresponds to the number of bilayers deposited on the substrate surface.

2.3.3 Post Permeability Microscopy

Cross sectional and frontal incidence SEM imaging of TFC membranes after permeation tests ("post mortem" analysis) confirmed no mechanical damage occurred as a result of the tests. Figure 2-7 shows representative results. The original crack free architectures remain intact, showing integrity and robustness of the TFC under the conditions resembling typical applications. This reinforces the conclusions based on the agreement of data with the hydrodynamic models for PCTE based membranes.

2.4 Conclusions

The hydrodynamic permeabilities of TFC membranes made by LbL surface modification of MF/UF substrates with primarily nanoparticles were significantly reduced with respect to the bare substrates. Nonetheless these correspond to water fluxes somewhat higher than typical

commercial NF/RO membranes indicating that these TFCs have potential to compete with commercial NF/RO membranes provided they exhibit good rejection characteristics.

Indeed, direct examination by microscopy of TFC membrane surfaces after permeation tests showed that the thin surface layers survive typical permeation conditions used in NF/RO operations without mechanical damage which implies robustness and integrity of the materials produced. For TFC membranes based on PCTE supports, very good agreement with realistic hydrodynamic models with no adjustable parameters was established . This provides indirect confirmation that the nanoparticle surface layers are largely defect (crack) free.

The work demonstrates that successful preparation of filtration quality TFC membranes is possible by LbL surface modification of organic porous supports with an inorganic surface nanolayer. The methodology developed can be implemented with reliable results for a variety of substrates and nanoparticle combinations, suggesting the ability to engineer filtration TFC membranes for water purification applications. Complementary work reports on the selectivity characteristics of these membranes.

Acknowledgements

The author acknowledges Ji Seung Kim for his cooperation and compromise with this project. Amrut Biswal and Christian Lubombo from the Durning's Lab for their assistance, Dr. Elliot Campbell for his help with materials, equipment, facilities and friendship. In addition, the author especially thanks Dr. Tom Gsell and Dr. Amarnauth Singh from Pall Corporation for our valuables discussions and suggestions and, of course, my friends Mike Steves and Pauline Adejo from the Pall Microscopy Lab for all their assistance. Partial funding for this research was provided by a Pall Corporation grant.

References

1. Loeb, S.; Sourirajan, S. *Advances in Chemistry Series* **1963**, 38, 117-132.

2. Riley, R.L.; Lonsdale, H.K.; Lyons, C.R. *Journal of Applied Polymer Science* **1971**, 15, 1267-1276.

3. Loeb, S. *ACS Symposium Series* **1981**, 153, 1-9.

4. Schmidt, G.; Malwitz, M. *Current Opinion in Colloid and Interface Science* **2003**, 8, 103–108.

5. Rittigstein, P.; Priestley, R.D.; Broadbelt, L.D.; Torkelson, J.M. *Nature* **2007**, 6, 278-282.

6. Merkel, T.C.; Freeman, B.D.; Spontak, R.J.;He, Z.; Pinnau, I; Meakin, P; Hill, A.J. *Science* **2002**, 296, 519-522.

7. Petersen, R.J. *Journal of Membrane Science* **1993**, 83, 81-150.

8. Jons, S.; Ries, P.; McDonald, C.J. *Journal of Membrane Science* **1999**, 155, 79-99

9. Ramakrishnan, S.; McDonald, C.J.; Prud'homme, R.K.; Carbeck, J.D. *Journal of Membrane Science* **2004**, 231, 57-70.

10. Lee, D.; Gemici, Z.; Rubner, M.F.; Cohen, R.E. *Langmuir* **2007**, 23, 8833-8837.

11. Greenlee, L.F.; Lawler, D.F.; Freeman, B.D; Marrot, B.; Moulin, P. *Water Research* **2009**, 43, 2317-2348.

12. Riley, R.L. *"Reverse Osmosis" in Membrane Separation Systems, Vol. 2* **1991**, Noyes Data Corporation

13. Geise, G.M.; Park, H.B.; Sagle, A.C.; Freeman, B.D.; McGrath, J.E. *Journal of Membrane Science* **2011**, 369, 130-138.

14. Arena, J.T.; McCloskey, B.; Freeman, B.D.; McCutcheon, J.R. *Journal of Membrane Science* **2011**, 375, 55-62.

15. Shannon, M.A.; Bohn, P.W.; Elimelech, M.; Georgiadis, J.G.; Mariñas, B.J.; Mayes, A.M. *Nature* **2008**, 452, 301-310.

16. Ulbricht, M. *Polymer* **2006**, 47, 2217-2262.

17. Ergun, S. *Chemical Engineering Progress* **1952**, 48, 89-94.

18. Mulder, M. *Basic Principles of Membrane Technology* **1991,** Kluwer Academic Publishers.

19. de Belder, A.N. *Dextran* **2003**, Amersham Biosciences Collection.

Substrate	Polyelectrolyte PE pre-coat (PAH/PAA)	Cationic Nanoparticles	Anionic Nanoparticles	Number bilayers	Post Treatment
PCTE 0.2 μm	NA	NA	NA	NA	NA
SPEES® 100 KDa	NA	NA	NA	NA	NA
PCTE 0.2 μm	2.5 bilayers	NA	NA	NA	Y
SPEES® 100 KDa	2.5 bilayers	NA	NA	NA	Y
PCTE 0.2 μm	2.5 bilayers	Spherical 15 nm Ludox® CL	Spherical 25 nm Ludox® TM	40	Y
PCTE 0.2 μm	2.5 bilayers	Spherical 15 nm Ludox® CL	Spherical 25 nm Ludox® TM	60	Y
PCTE 0.2 μm	2.5 bilayers	Spherical 15 nm Ludox® CL	Spherical 25 nm Ludox® TM	80	Y
PCTE 0.2 μm	2.5 bilayers	Spherical 15 nm Ludox® CL	Spherical 25 nm Ludox® TM	100	Y
PCTE 0.2 μm	2.5 bilayers	Spherical 15 nm Ludox® CL	Elongated Snowtex®-UP	40	Y
PCTE 0.2 μm	2.5 bilayers	Spherical 15 nm Ludox® CL	Elongated Snowtex®-UP	60	Y
PCTE 0.2 μm	2.5 bilayers	Spherical 15 nm Ludox® CL	Elongated Snowtex®-UP	80	Y
PCTE 0.2 μm	2.5 bilayers	Spherical 15 nm Ludox® CL	Elongated Snowtex®-UP	100	Y
SPEES® 100 KDa	2.5 bilayers	Spherical 15 nm Ludox® CL	Spherical 25 nm Ludox® TM	40	Y
SPEES® 100 KDa	2.5 bilayers	Spherical 15 nm Ludox® CL	Spherical 25 nm Ludox® TM	60	Y
SPEES® 100 KDa	2.5 bilayers	Spherical 15 nm Ludox® CL	Spherical 25 nm Ludox® TM	80	Y
SPEES® 100 KDa	2.5 bilayers	Spherical 15 nm Ludox® CL	Spherical 25 nm Ludox® TM	100	Y
SPEES® 100 KDa	2.5 bilayers	Spherical 15 nm Ludox® CL	Elongated Snowtex®-UP	40	Y
SPEES® 100 KDa	2.5 bilayers	Spherical 15 nm Ludox® CL	Elongated Snowtex®-UP	60	Y
SPEES® 100 KDa	2.5 bilayers	Spherical 15 nm Ludox® CL	Elongated Snowtex®-UP	80	Y
SPEES® 100 KDa	2.5 bilayers	Spherical 15 nm Ludox® CL	Elongated Snowtex®-UP	100	Y

Note 1: NA – Not applicable.
Note 2: Snowtex®–UP: Anionic elongated silica nanoparticle whose dimensions are: 9-15 nm width; 40-100 nm length

Table 2-1. *Summary of all samples tested for hydrodynamic permeability measurements.*

a)

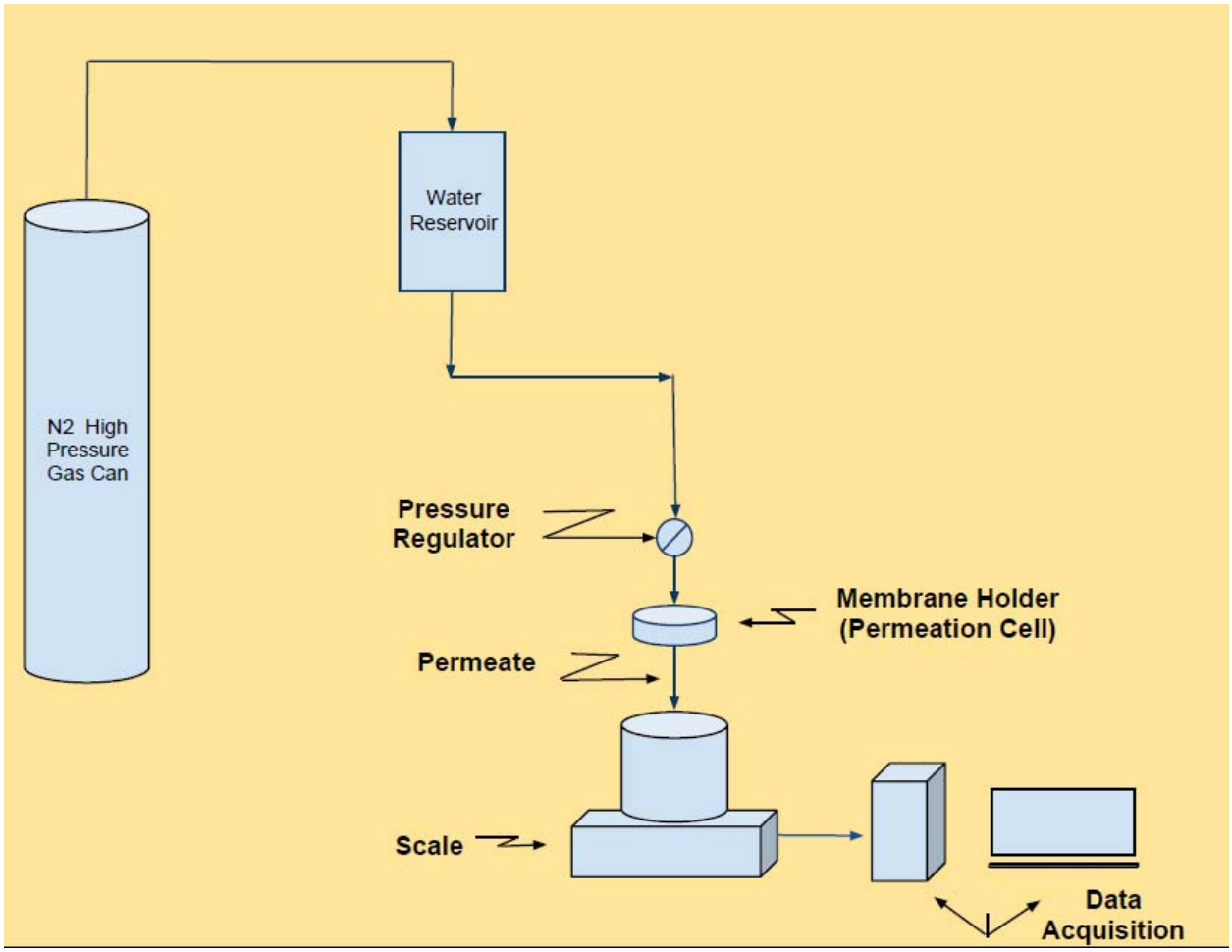
Water Reservoir
N2 High Pressure Gas Can
Pressure Regulator
Membrane Holder (Permeation Cell)
Permeate
Scale
Data Acquisition

b)

Figure 2-1. *(a) Schematic of the dead-end permeation setup designed to measure the steady flux and hydrodynamic permeability for porous substrates and TFC membranes. (b) Image of the actual equipment installed.*

a)

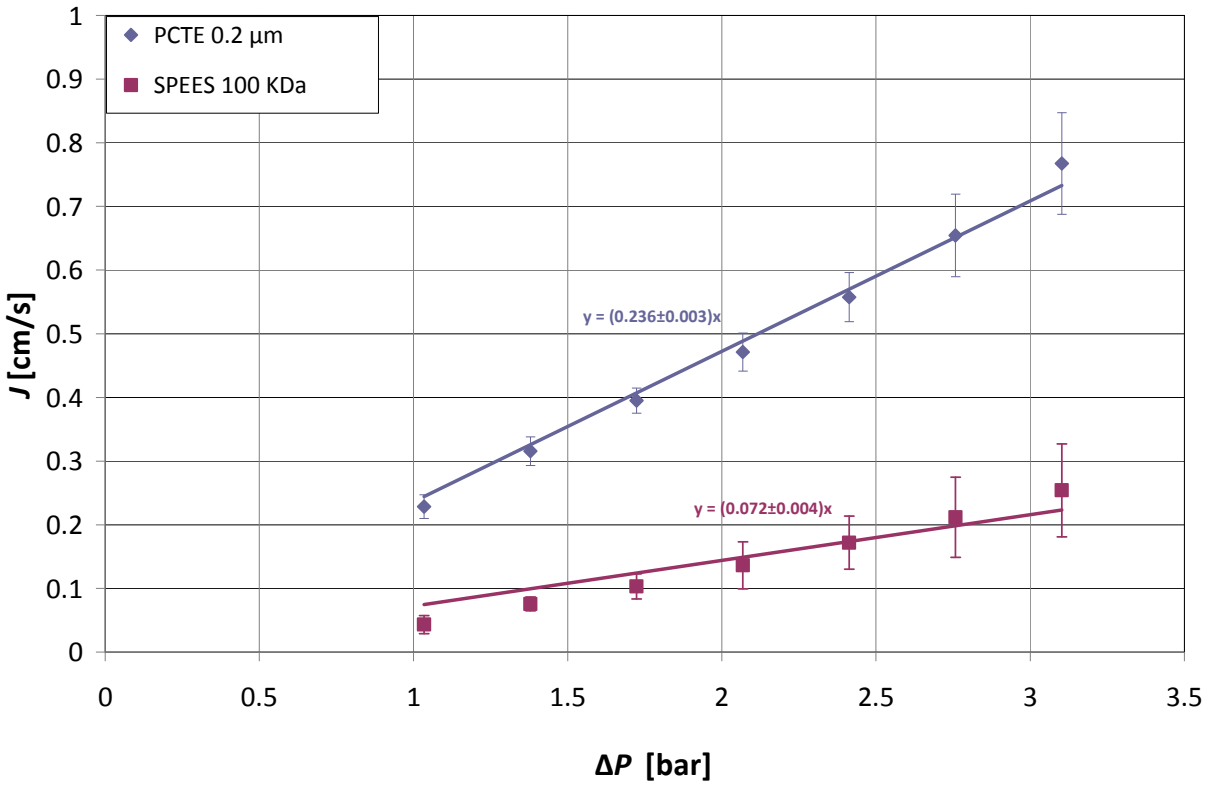
PCTE 0.2 µm
SPEES 100 KDa
y = (0.236±0.003)x
y = (0.072±0.004)x
J [cm/s]
ΔP [bar]
0
0.1
0.2
0.3
0.4
0.5
0.6
0.7
0.8
0.9
1
0
0.5
1
1.5
2
2.5
3
3.5

b)

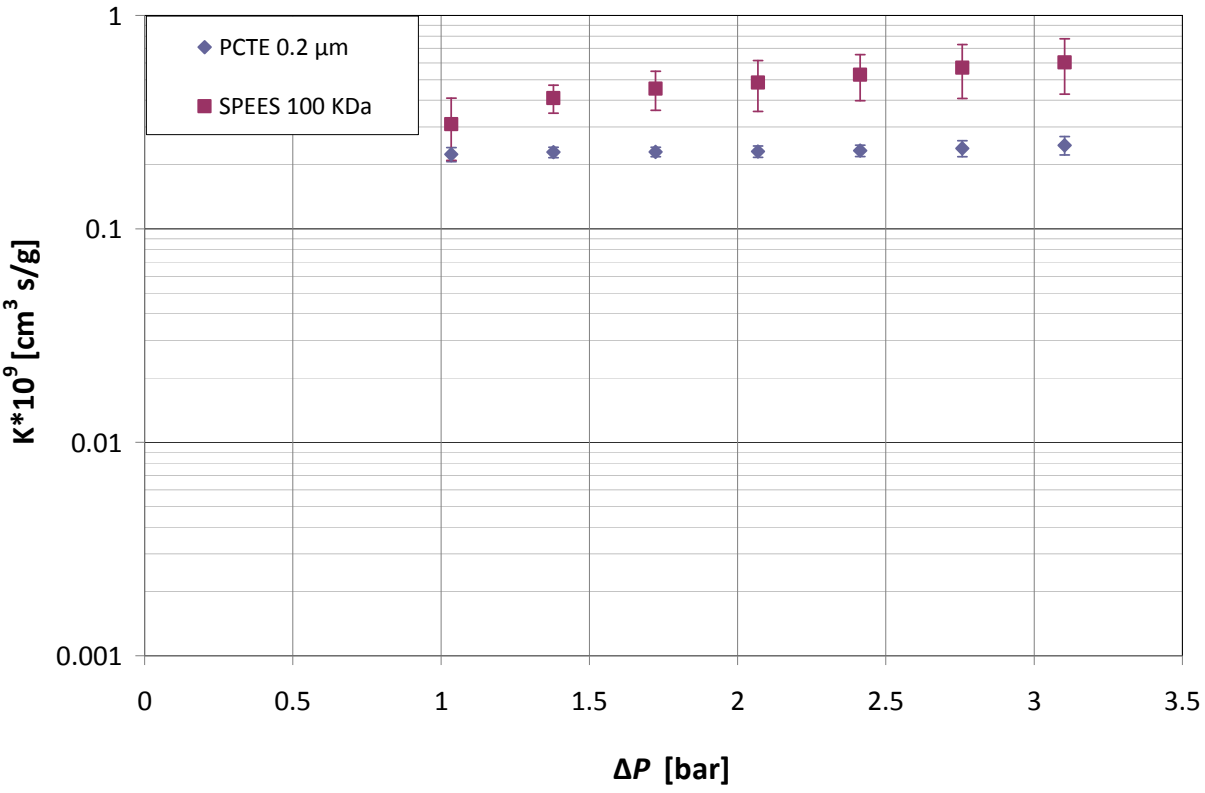

Figure 2-2. *Representative experimental data for the uncoated substrates PCTE 0.2 µm and SPEES 100 KDa at 25°C: (a) water flux, J vs. pressure drop ΔP. The slope values are shown with 95% confidence limits. (b) hydrodynamic permeability* K *vs. pressure drop ΔP. The lines in (a) are regression fits constrained to the origin.*

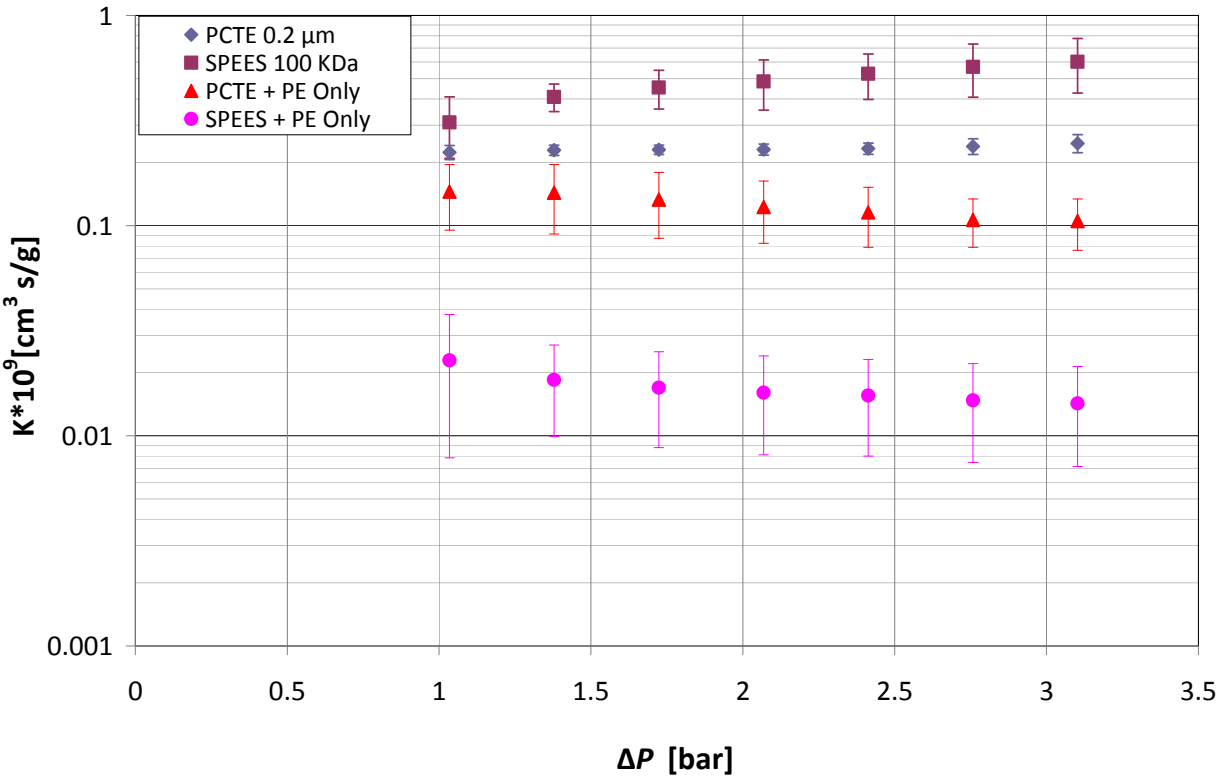

Figure 2-3. *Permeability* K*, at 25°C of PCTE 0.2 µm and SPEES 100 KDa substrates before and after surface modification with 2.5 bilayers of polyelectrolytes (PAA & PAH).*

a)

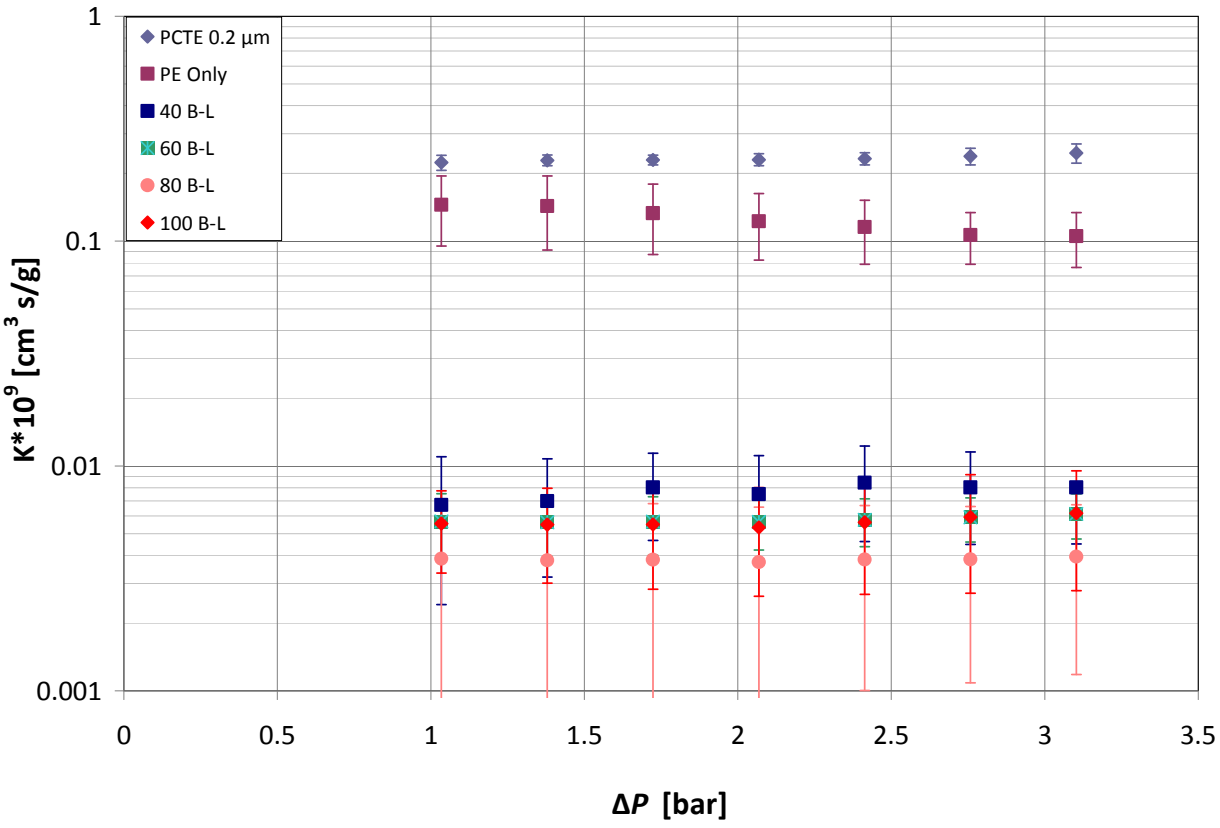
PCTE 0.2 µm
PE Only
40 B-L
60 B-L
80 B-L
100 B-L
1
0.1
0.01
0.001
K*10^9 [cm^3 s/g]
0
0.5
1
1.5
2
2.5
3
3.5
ΔP [bar]

b)

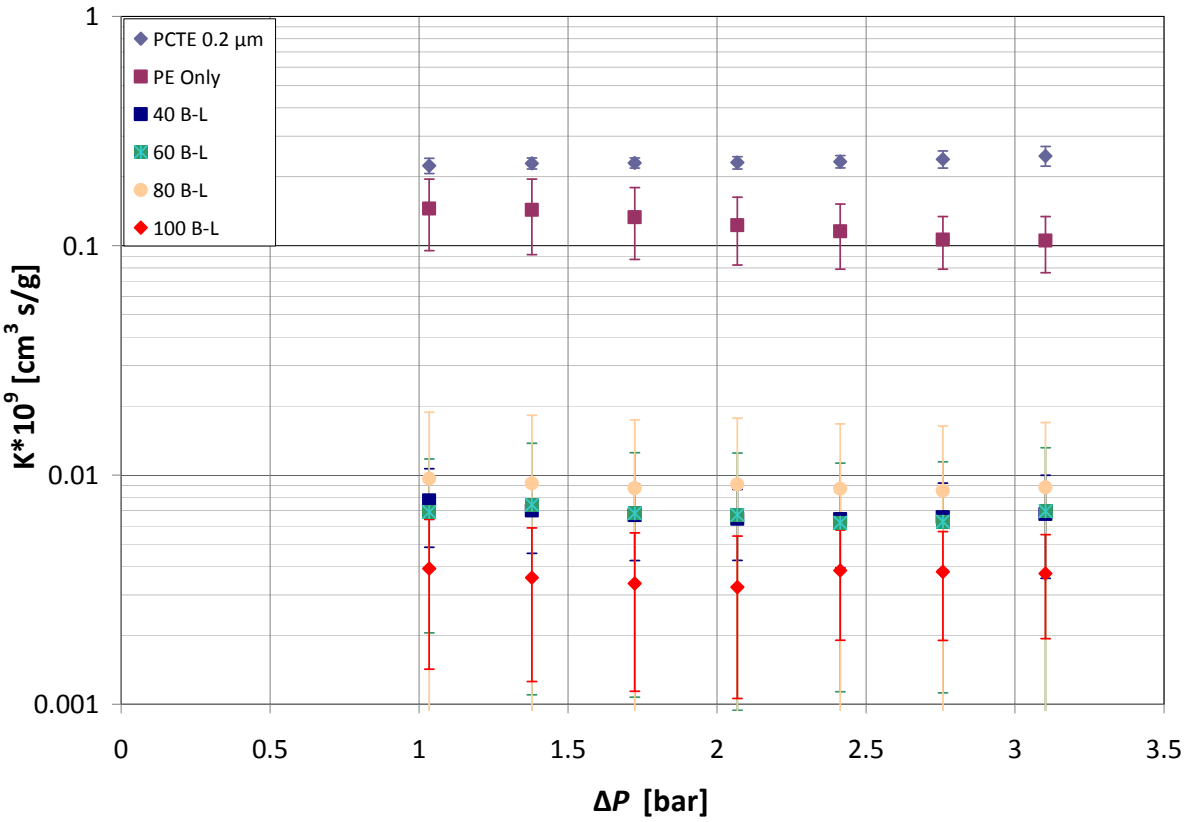

Figure 2-4. *Permeability* K *at 25°C of TFC membranes from: PCTE 0.2 µm substrates modified with 2.5 bilayers of polyelectrolytes (PAA & PAH) and (a) Ludox CL/Ludox TM (cationic/anionic) spherical/spherical silica nanoparticles for different numbers of bilayers. (b) Ludox CL/Snowtex UP (cationic/anionic) spherical/elongated silica nanoparticles for different numbers of bilayers.*

a)

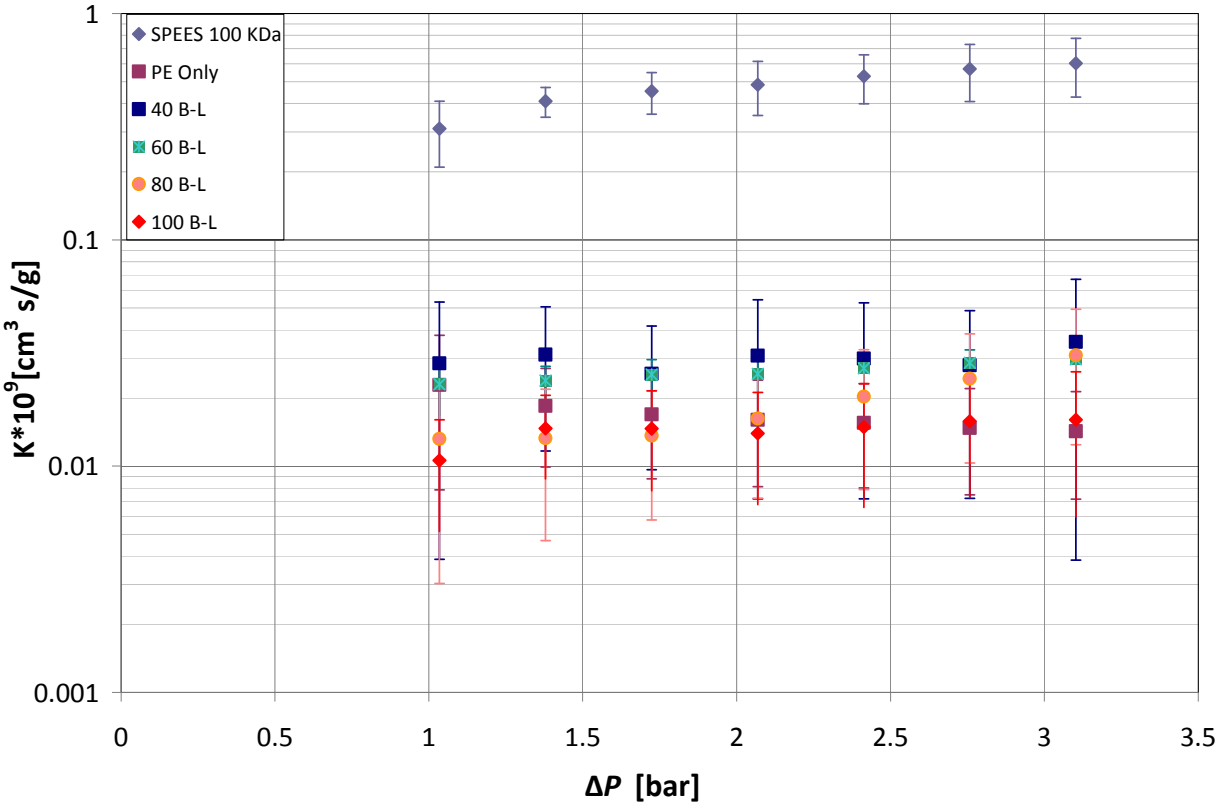
SPEES 100 KDa
PE Only
40 B-L
60 B-L
80 B-L
100 B-L
1
0.1
0.01
0.001
K*10^9[cm^3 s/g]
0
0.5
1
1.5
2
2.5
3
3.5
ΔP [bar]

b)

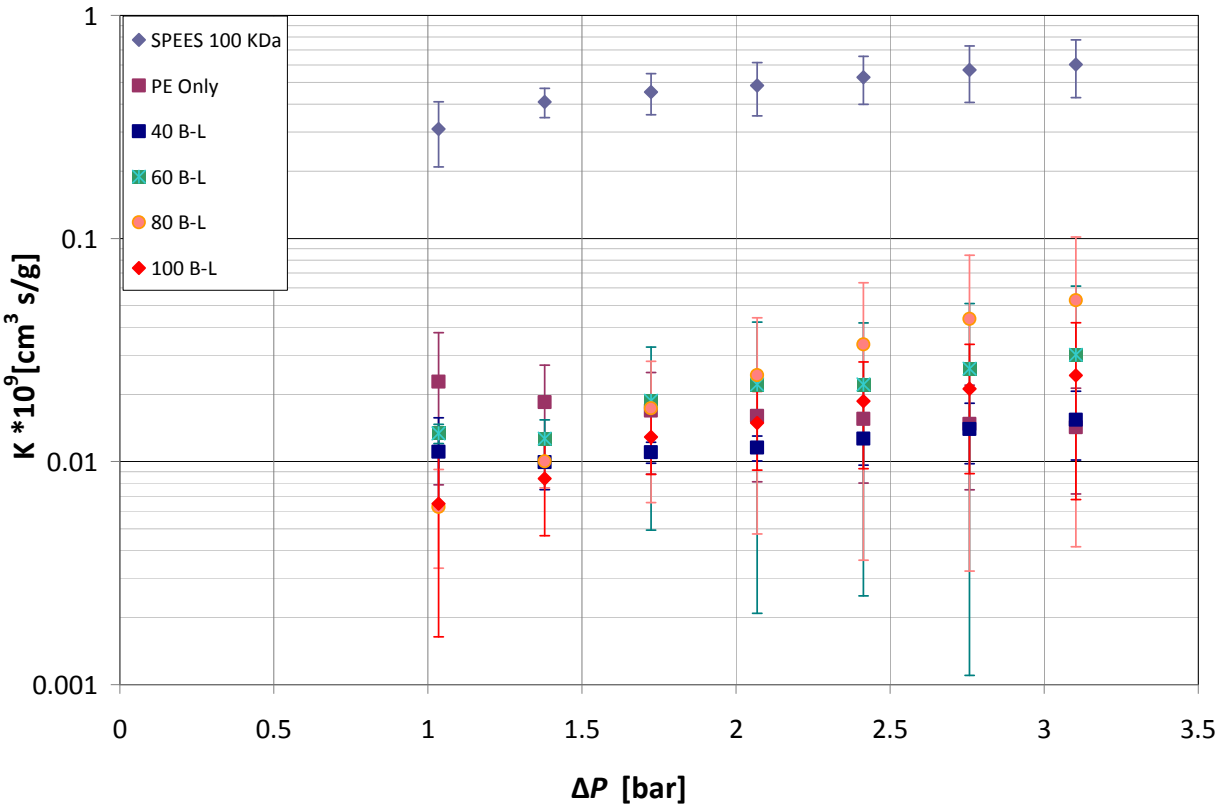

Figure 2-5. *Permeability* K *at 25°C of TFC membranes from: SPEES 100 KDa substrates modified with 2.5 bilayers of polyelectrolytes (PAA & PAH) and (a) Ludox CL/Ludox TM (cationic/anionic) spherical/spherical silica nanoparticles for different numbers of bilayers. (b) Ludox CL/Snowtex UP (cationic/anionic) spherical/elongated silica nanoparticles for different numbers of bilayers.*

a)

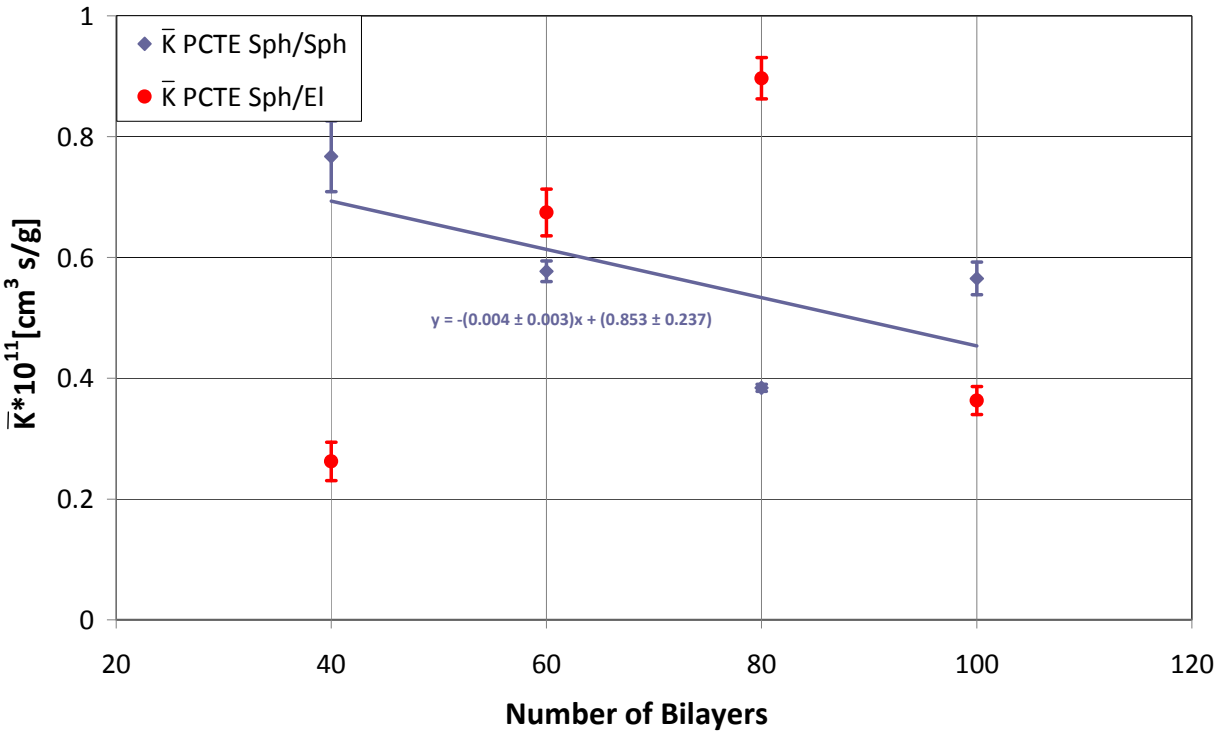
$\bar{K}$ PCTE Sph/Sph
$\bar{K}$ PCTE Sph/El
y = -(0.004 ± 0.003)x + (0.853 ± 0.237)
$\bar{K}*10^{11}$[cm^3 s/g]
Number of Bilayers
0
0.2
0.4
0.6
0.8
1
20
40
60
80
100
120

b)

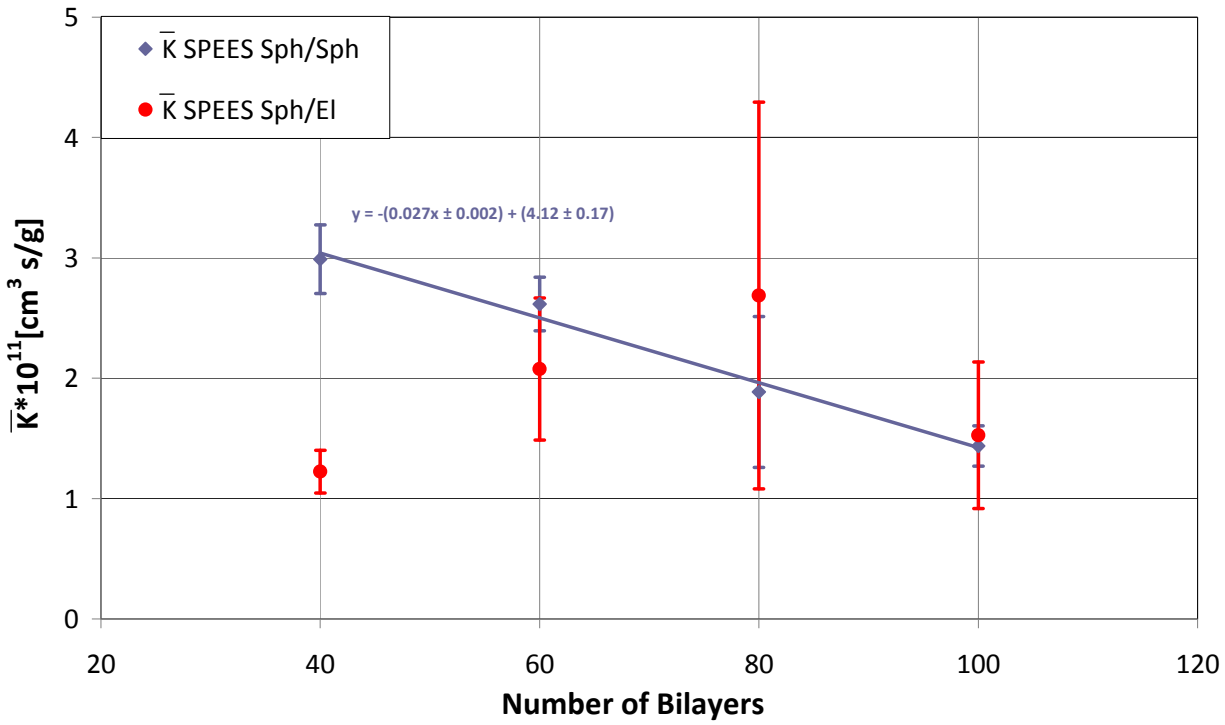

Figure 2-6. *Average permeability* $\overline{K}$ *at 25°C vs. number of bilayers of nanoparticles deposited for TFC membranes from: (a) PCTE 0.2 µm substrates modified with 2.5 bilayers of polyelectrolytes (PAA & PAH) and Ludox CL/Ludox TM (cationic/anionic) spherical/spherical silica nanoparticles and Ludox CL/Snowtex UP (cationic/anionic) spherical/elongated silica nanoparticles. (b) SPEES 100 KDa substrates modified with 2.5 bilayers of polyelectrolytes (PAA & PAH) and Ludox CL/Ludox TM (cationic/anionic) spherical/spherical silica nanoparticles and Ludox CL/Snowtex UP (cationic/anionic) spherical/elongated silica nanoparticles. The* $\overline{K}$ *values shown are the averages obtained over the ΔP range employed from 15-45 psi. The error bars shown provide the repeatability around an average based on measurements from 3-5 samples each.*

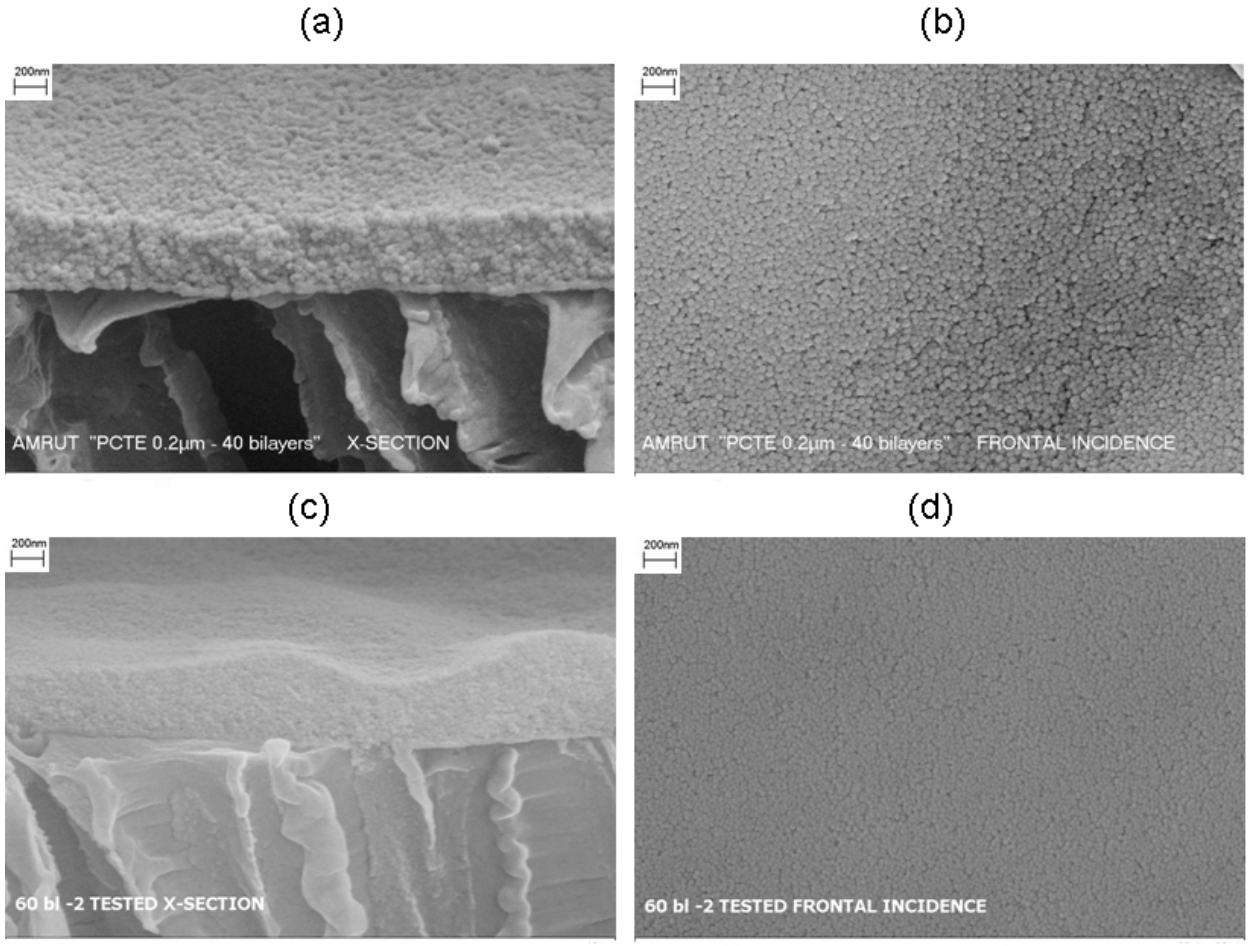

Figure 2-7. *Representative SEMs of the TFC membranes from PCTE substrates after permeation experiments (post mortem analysis) showing that the clear sharp interface remains intact between the substrate and nanoparticle layer. The crack-free architecture does not seem to have been altered with respect to the originals, demonstrating mechanical strength and robustness. (a) SEM of fracture surface cross section and frontal incidence of PCTE 0.2 µm - 40 bl - Ludox CL/Snowtex SUP (cationic/anionic) spherical/elongated silica nanoparticles. (b) Frontal incidence SEM of the same TFC (c) and (d) Fracture surface cross section and frontal incidence SEM of PCTE 0.03 µm - 60 bl - Ludox CL/Snowtex SOUP(cationic/anionic)spherical/elongated silica nanoparticles respectively.*

Chapter 3. Selectivity of Nanoparticle Surface Modified, Thin Film Composite Membranes

Abstract

Layer by Layer (LbL) deposition of mainly inorganic (silica) nanoparticles enabled surface modification of polymeric micro and ultrafiltration (MF/UF) membranes to produce filtration quality thin film composites (TFC) membranes with potential nanofiltration (NF) and reverse osmosis (RO) capabilities. Here we determine the separations capabilities of these novel TFC membranes using standard "rejection" tests normally used to characterize NF and RO membranes for their capabilities in typical applications, such as water softening or desalination. TFC membranes made from different combinations of substrates and surface modifications were tested, using both spherical (cationic/anionic) and elongated (anionic) silica nanoparticles in the surface layer with characteristic sizes in the range of 10-30 nm. For these, we report the dextran standards molecular weight "cut-off" (MWCO) using mixed dextrans from 1.5 to 500 KDa in dead-end stir cells, and the percentage of rejection of standard bivalent and monovalent salt solutions using steady cross flow permeation experiments. The results confirm rejection of at least 60% of even the smallest dextrans, an estimated dextran MWCO of 20 KDa, and rejection of 10% and 20% for monovalent (NaCl) and bivalent ($MgSO_4$) salts, respectively, for all the TFC membranes studied, while the unmodified membranes showed no rejection capability at all.

The work confirms that nanoparticle based LbL surface modification of MF/UF substrates can produce TFC membranes capable for at least some water purification applications, such as nanofiltration (NF) softening processes and natural organic matter (NOM) elimination.

3.1 Introduction

The term thin film composite (TFC) membrane refers to a bilayer film consisting of a porous nonselective support layer with a very thin selective barrier layer on top. [1, 2, 3] These membranes can combine organic and inorganic materials and their key properties can be tailored over a significant range for many applications[4, 5, 6] such as components for fuel cells and batteries, industrial gas separations and water purification.[6-9] Such structures have become standard for demanding pressure driven "filtration" applications used for water clean up, including ultrafiltration (UF), nanofiltration (NF) and reverse osmosis (RO). Since the "skin" layer and "support" core are complementary, they can be optimized independently for specific applications. Consequently, modern TFC membrane technology for water purification is remarkably diverse, with membranes having thermal and chemical stability, anti-biofouling characteristics, and even self-cleaning properties. [1, 4-10]

Our interest is to evaluate the potential for water clean up applications of novel TFC membranes produced by layer by layer (LbL) deposition of (mainly) inorganic nanoparticles onto existing microfiltration (MF) and ultrafiltration (UF) membranes. [1, 11] We report here on the selectivity capabilities of these TFC membranes, that is, their ability to reject "standard" contaminants in aqueous stock solutions (e.g. mixed dextrans and monovalent and bivalent salts), under pressure drops typically encountered in water purification processes. These measurements provide a necessary validation for any candidate membranes to be used in these applications.

In particular, we report a specification commonly used by manufacturers to describe the retention capabilities of membranes used in a variety of UF and NF applications known as the molecular weight "cut-off" (MWCO). This refers to the molecular mass of a standard polymeric solute which exhibits 90% rejection by the membrane in a pressure driven filtration process

(R90). Ultrafiltration and nanofiltration membranes for water clean up are usually characterized in this way using water soluble solutes of known molecular size, such as poly-ethylene glycols (PEG), dextrans or globular proteins. While there is currently no industry standard test for the determination of MWCO, dextran rejection tests using well defined molecular weight samples have become a common for characterization of ultrafiltration and some nanofiltration membranes. Dextrans are readily available in wide range of molecular weights and have low protein binding characteristics.[12-15] They are neutral, essentially linear polysaccharides produced by *Leuconostoc mesenteroides* NRRL B-512(F) bacteria.[12] The repeat unit consists of an (*α-1,6 linked glucan)* with side chains attached to the 3-position of the backbone glucose units[12] as shown in the scheme below.

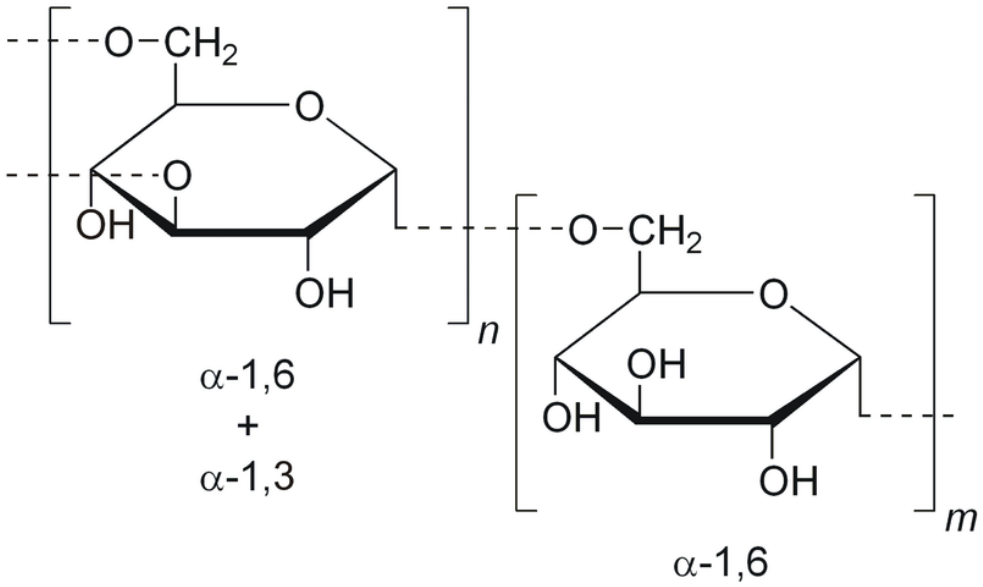

The dextran rejection experiment employed by us uses a range of different sized molecules in one challenge, compared to other procedures where a series of challenges with monodisperse solutes is used to determine the membrane MWCO. The concentrations of the various sized dextrans used in the challenge solution are set so that all size species are present at concentrations representative of typical applications.[13-16]

It is worth noting that dextran rejection measurements have become so common in characterizing selectivity of TFC membranes that the results are frequently reported as an effective pore size distribution for a membrane. Dextran rejection is also used to study membrane fouling against typical organic suspended contaminants in pressure driven UF and NF processes.[14, 15]

Selectivity of TFC membranes for NF or RO desalination processes is frequently characterized by percentage of rejection of stock solutions monovalent and bivalent salts in a pressure driven filtration process. Typically, NF rated membranes have a very high rejection of bivalent salts but a widely variable rejection of monovalent salts.[3, 19, 20] On the other hand RO membranes, should achieve greater than 95% rejection of monovalent salts such as NaCl.[17, 18]

Selectivity of TFC membranes has been studied systematically by many different groups. Generally, data shows that the higher the rejection, the lower the flux indicating a trade off between selectivity and permeability for most classes of UF, NF and RO membranes[3, 17, 18], although there are exceptions. For example, TFC RO membranes made by interfacial polymerization of polyamids, including zeolite-polyamide or polydopamine (PDA)-polyamide nanocomposites results in reverse osmosis membranes with dramatically improved permeability while maintaining comparable selectivity with RO membranes from the pure polyamide.[21, 22] These particular works demonstrate that exceptions to the selectivity/permeability trade-off rule of thumb within a set of closely related TFC membranes can result from specifically engineered nano-scale modifications of the selective “skin” layer. The fabrication method for the TFC membranes studied here readily enables such manipulations.

3.2 Experimental

3.2.1 Materials

All materials were used as received. The materials used for TFC membrane fabrication are described in detail in Chapter 1. For selectivity experiments in this chapter, we used MF rated substrates Nuclepore® polycarbonate track-etch (PCTE) membranes, 0.2 μm nominal pore size, from Whatman (Kent, UK) and UF rated substrates sulfonated poly etherethersulfone (SPEES®) with 100 KDa dextran molecular weight "cut-off" (MWCO) from Pall Corporation (Port Washington, NY). Two polyelectrolytes, poly(allylamine hydrochloride) (PAH, M_w = 56,000 Dalton), and poly(acrylic acid) (PAA, M_w=100,000 Dalton, 35 wt% solution in water) purchased from Sigma Aldrich (St. Louis, MO) were used in the TFC fabrication. The nanoparticles employed were Ludox® CL, supplied as a colloidal solution of spherical silica nanoparticles (30 wt% solution in water) with 15 nm average diameter, and Ludox® TM-40, supplied a colloidal spherical silica nanoparticles solution (40 wt% solution in water) with 25 nm average diameter from Sigma Aldrich (St. Louis, MO). Also anisotropic particles were used: Snowtex®-UP 9-15 nm width, 40-100 nm length, supplied as a basic colloidal solution of elongated silica nanoparticles, and Snowtex®-OUP 9-15 nm width, 40-100 nm length, supplied as an acidic colloidal solution of elongated silica nanoparticles. Both were obtained through Nissan Chemical America (Houston, TX). Millipore Q-Gard® 1 and Progard® 2 (Billerica, MA) systems provided DI water with a resistivity of 18.2 MΩ·cm @ 25 °C for all experiments reported in this work.

All dextrans, with the exception of a 10 KDa sample purchased from Sigma Aldrich (St. Louis, MO), were obtained from Fluka (St. Louis, MO). Sodium chloride (NaCl) and magnesium sulfate ($MgSO_4$) salts were obtained from Sigma Aldrich (St. Louis, MO).

3.2.2 TFC Membrane Preparation

The preparation of TFC membranes via LbL deposition is described in detail in Chapter 1. The supports used were coated by LbL using a robotic dipper on only one side of the flat sheet membrane, that is, the dip coating method using the special mounting frames described in Chapter 1 was employed. The samples prepared for selectivity experiments are summarized in Tables 3-1 and 3-2. The deposited nanoparticle layer thickness varied from about 200 nm for 40 bilayers for the spherical/spherical particle case to about 600 nm for 40 bilayers for the spherical/elongated particle case. All the TFC samples reported in this work were autoclaved at 121ºC for approximately one hour after the nanoparticle deposition, as described in Chapter 1.

3.2.3 Dextran Rejection via "Stirred Cell" Dead-End Permeation

The selectivity tests designed to evaluate mixed dextran rejection, employ a polydisperse stock solution of dextrans, as detailed in Table 3-3. The stock solution contains dextrans with molecular weights ranging from 1.5 KDa to 500 KDa. The experiments are conducted using 44.5 mm diameter Amicon 8050 "stirred" cells supplied by Millipore (Billerica, MA) with 50 ml volume capacity. Figure 3-1 (a) shows a schematic representation of the stirred cell dead-end permeation experiment. The actual setup used is shown in Figure 3-1 (b). The Amicon cells operate in a transient dead-end mode with the feed chamber magnetically stirred to minimize concentration polarization. The uncoated substrates and TFCs were first tested in the stir cell with DI water at 55 psi and 300 rpm at ambient temperature. The time to collect about 40 ml of permeate was determined and water flux calculated there from. Following this, experiments with mixed dextrans were carried out in the same cell at 5 psi and 220 rpm in the feed side of the cell. The time to collect about 3 ml of permeate was recorded and the solution flux was calculated

there from. Afterwards the feed and permeate solutions were analyzed by high pressure liquid chromatography (HPLC).

To perform the analysis, we employed a Thermo Scientific (Waltham, MA) HPLC setup equipped with a RI-150 refractive index detector and using a Tosoh TSK-GEL G4000PWXL column (King of Prussia, PA) for higher molecular weights and a Tosoh TSK-GEL G3000PWXL column for dextrans whose molecular weights were less than 60 KDa. Before running the chromatography, fresh HPLC grade water (50 µl) was injected to the mobile phase reservoir repeatedly until a flat baseline was obtained. For all runs the mobile phase flow rate was fixed at 1.0 ml/min.

Dextran standards for a HPLC calibration were prepared by measuring 5.0 mg of each dextran fraction into separate 10 ml volumetric flasks and dissolving them in HPLC grade water. The standards were first filtered using a 0.45 µm Pall Acrodisc® syringe filter and then injected (50 µl) into the HPLC at a mobile phase flow rate of 1.0 ml/min. The chromatographs enabled calculation of the retention times for each standard and these data were added to the historic data of dextran for these columns for the instrument. A comprehensive calibration for dextrans ($\log(M_p)$ vs. retention time) was therefore available and used for the evaluation of % rejection. Here M_p means the peak molecular weight for the (nearly) monodisperse standard samples.

Samples from dead-end permeation (feed and filtrate) were analyzed by first filtering them using a 0.45 µm Pall Acrodisc® syringe filter, then injecting 50 µl of each sample at a mobile phase flow rate of 1.0 ml/min into the HPLC. A water injection at the beginning and end of each sample run checked for any baseline shift. The response chromatograms (chromatogram deflection from baseline vs. retention time) were converted to response vs. dextran molecular

weight using the column calibration equations. Selectivity profiles are plotted as % rejection (R_d) vs. dextran molecular weight, where

$$R_d = \left(1 - \frac{Permeate\,\mathrm{Re}\,sponse}{Feed\,\mathrm{Re}\,sponse}\right) \times 100 \qquad (3\text{-}1)$$

for each molecular weight.

3.2.4 Salt Rejection via Steady Cross Flow Permeation

The selectivity experiments for mono and bivalent salts were conducted using a custom built cross flow cell equipped with VWR™ Symphony™ SP80PC Meter (Norristown, PA) for analysis of feed and permeate content (pH resolution ±0.01, relative accuracy ±0.002; conductivity resolution ±0.001 μS/cm, accuracy ±0.01 μS/cm). Sodium chloride (NaCl) and magnesium sulfate ($MgSO_4$) are the monovalent and bivalent salt standards used for these tests. 1 g/L of NaCl and 2 g/L of Mg SO_4 stock solutions were prepared with 5.00 g of NaCl and 10.00 g of $MgSO_4$ in DI water. A schematic representation of the setup appears in Figure 3-2. Figure 3-3 (a) and (b) shows the actual cross flow cell. The equipment is set up assembling the cross flow membrane sample holders in correct orientation (see Figure 3-2 (c)) and run at 100 psi and 25°C.

To perform the cross-flow experiment, first a membrane is placed in the cell and then pure deionized water is flowed for feed and resulting permeate. Then, standard solutions of NaCl or $MgSO_4$ are introduced through the upstream feed side compartment. The feed conditions were 100 psi, 25°C and a flow rate of 1 L/min for all experiments. After every 15 minutes of feed flow recirculation, permeate is collected for 4 minutes. Conductivity measurements on the feed and permeate are performed to evaluate the % rejection as described below. This process is repeated

until the results achieve steady state. The percentage of salt rejection (R_s) is calculated from data by the following equation:

$$R_s = \left(1 - \frac{C_p}{C_f}\right) \times 100 \tag{3-2}$$

in which C_p corresponds to the permeate conductivity and C_f the feed conductivity.

3.3 Results and Discussion

3.3.1 Dextran Rejection by TFC Membranes

As a control, the flux and the selectivity of the MF (PCTE 0.2 μm) and UF (SPEES 1000 KDa) rated substrates *without* surface modification were determined. We then evaluated dextran rejection after modifying each of the bare membrane surfaces for both substrates, using LbL deposition, with a very thin polyelectrolyte layer (2.5 bilayers of PAA and PAH atop the membrane surface) followed by 40 bilayers of Ludox CL/Ludox TM (cationic/anionic) spherical/spherical or Ludox CL/Snowtex UP (cationic/anionic) spherical/elongated silica nanoparticle combinations (see Table 3-2). The experimental conditions were identical for all the tests conducted (5 psi upstream, 220 rpm rotation in upstream compartment). The summary results are shown in Figure 3-4 for PCTE (MF rated) based composites and Figure 3-5 for SPEES (UF rated) based composites.

As expected, there is very limited dextran rejection from either the MF rated or UF rated substrates alone. There are, however, some differences observed between the two uncoated membranes especially for the high MW dextrans. The SPEES membrane clearly exhibits somewhat larger rejection of the higher dextrans compared with the PCTE substrate. This is undoubtedly due to the different pore size characteristics of the two. SPEES 100 KDa is an asymmetric UF rated membrane while PCTE 0.2 μm is symmetric MF rated membrane. Based on our imaging, the SPEES average sized pores are more than an order of magnitude smaller

than PCTE, and close to the dextran radius of gyration (R_g) for 100 KDa molecules.[12] In particular, the mean pore size of the SPEES UF rated membrane, 10-20 nm, is comparable with the characteristic size of the largest dextrans in solution (500 KDa) whose R_g is reported as 200 Å and whose hydrodynamic radius is reported as 147 Å[12]. Consequently it is expected that some of the high MW dextran would be rejected by the native SPEES membrane. On the other hand, the MF rated PCTE 0.2 μm membrane has a mean pore size significantly larger than the largest dextran in solution, consistent with the fact that all dextrans tested pass through the membrane unhindered.

The effect of depositing only the thin polyelectrolyte layer on the substrate's surface on dextran selectivity is dramatically different for the SPEES and PCTE based materials. While the PE coating on PCTE substrates causes no significant improvement of the rejection capabilities (the weak 8-10% shift of the entire plot upward in Figure 3.4 for the PE coated samples relative to the uncoated samples is within the experimental repeatability), the SPEES substrate showed significant shift in these characteristics. Overall the rejection improves for the SPEES noticeably and shows typical "cut off" characteristics in the range of the molecular weights explored. This result correlates well with our findings in previous chapters regarding the effects of the polyelectrolyte layer on this membrane's pore characteristics and hydrodynamic permeability. Recall the polyelectrolyte layer appears to block all but the very largest pores of the UF rated SPEES support, which is a tighter, more disperse membrane than the PCTE, suggesting that an effect on membrane selectivity should occur (see Figures 1-2 (c) and (d)). Recall also that the PE coating caused a decrease of the permeability of more than an order of magnitude for this substrate. By contrast, the same PE treatment had a much smaller effect on the MF rated PCTE whose much larger, nearly monodisperse pores were not significantly blocked, as observed

qualitatively by microscopy (Figure 1-2 (c) and (d)), and more quantitatively by the hydrodynamic permeability being nearly unaffected (See Figure 2-3).

TFC membranes were then challenged for dextran rejection, with both substrates modified with the polyelectrolyte layer and with 40 bilayers of Ludox CL/Ludox TM (cationic/anionic) spherical/spherical or Ludox CL/Snowtex UP (cationic/anionic) spherical/elongated silica nanoparticle combinations. A portion of the samples were not able to generate enough permeate at the operating conditions used for dextran rejection (5 psi pressure drop in the dead-end stir cells) which agrees with experience for this test for commercial membranes with NF or RO rating. From those samples able to generate permeate, typical "S" shaped selectivity plots resulted from the HPLC analysis (see Figures 3-4 and 3-5). For the PCTE 0.2 μm based composites the effect of adding nanoparticles is dramatic and very similar results were found for TFCs made on this substrate, with 40 bilayers of spherical particles (anionic and cationic) and for those made with 40 bilayers of anionic elongated nanoparticles and cationic spherical ones. The data indicate an average rejection of 60% for the smallest dextran in the stock solution (1500 Da) and 90% or higher for dextran molecules (R90) whose molecular weight is 20 KDa or larger, that is, the modified membranes exhibit an R90 of 20 KDa.

For the SPEES 100 KDa based composites only samples made with 40 bilayers of the spherical/spherical nanoparticles combination produced permeate. The rejection results are comparable to the PCTE based composites using the same surface modification, i.e. they are clearly governed by the nanoparticles layer, as they are for the PCTE based materials.

3.3.2 Salt Rejection by TFC Membranes

Cross flow experiments for NaCl and Mg SO_4 rejection were conducted only on SPEES based membranes and first on control samples of the uncoated SPEES 100 KDa membrane. These exhibits no rejection of either the monovalent or bivalent salts, i.e. the conductivities of the feed and permeate were always identical.

The SPEES 100 KDa based composites, with both the polyelectrolyte layer and with 40 bilayers of the Ludox CL/Ludox TM (cationic/anionic) spherical/spherical silica nanoparticle combinations, were challenged for monovalent and bivalent salts. The results, based on conductivity measurements, for solutions of 1 g/L of NaCl and 2 g/L of $MgSO_4$ indicate 10% rejection of NaCl and 20% of $MgSO_4$. (See Table 3-4).

3.4 Conclusions

This work demonstrates the successful preparation of filtration quality TFC membranes for water purification applications in the NF range by LbL surface modification of existing MF and UF rated membranes with an inorganic surface layer, comprised primarily of nanoparticles.

In particular dextran rejection by surface modified TFC membranes for either MF or UF rated supports is comparable with typical NF rated membranes for NOM removal, [17, 23, 24] whereas the bare substrates, or TFC's with surface modification by only a few bilayers of polyelectrolytes show minimal or no selectivity. Meanwhile measured water permeabilities for the nanoparticles modified membranes are significantly higher than most commercial NF membranes indicating that these TFCs have good potential for improved performance relative to existing materials, for at least some NF applications.

The cross flow selectivity results for mono and bivalent salts are also promising. While the TFC membranes produced in this work have relatively low salt rejection, it is nonetheless

significant that 10/20% is achieved for mono and bivalent salts respectively over substrates with no capability whatever. The surface modification procedures developed allow engineering of the selective surface layer (e.g. manipulation of its nano-scale architecture and internal chemistry) so that more effective desalination characteristics could likely be achieved.

Acknowledgements

The author gratefully thanks Selina Shi from Pall Corporation for all her cooperation and assistance during this project. Special thanks to Pall Corporation for the use of their facilities, labs and equipment and to Dr. Tom Gsell and Dr. Amarnauth Singh for our fruitful discussions. Partial funding for this research was provided by a Pall Corporation grant.

References

1. Decher, G.; Schlenoff, J.B. *Multilayer Thin Films* **2003,** Wiley-VCH.
2. Decher, G. *Science* **1997**, **277**, 1232-1237.
3. Petersen, R.J. *Journal of Membrane Science* **1993**, 83, 81-150.
4. Schmidt, G.; Malwitz, M. *Current Opinion in Colloid and Interface Science* **2003**, 8, 103–108.
5. Sanchez, C.; Julian, B.; Belleville, P.; Popall, M. *Journal of Materials Chemistry* **2005** 15, 3559–3592.
6. Vaia, R.A.; Giannelis, E.P. *Material Research Society Bulletin* **2001**, 26, 394–401.
7. Merkel, T.C.; Freeman, B.D.; Spontak, R.J.; He, Z.; Pinnau, I; Meakin, P; Hill, A.J. *Science* **2002**, 296, 519-522.
8. Rittigstein, P.; Priestley, R.D.; Broadbelt, L.D.; Torkelson, J.M. *Nature* **2007**, 6, 278-282.
9. Hillie, T.; Hlophe, M. *Nature Nanotechnology* **2007**, 2, 663-664.
10. Mauter, M.S.; Wang, Y.; Okemgbo, K.C; Osuji, C.O.; Gianellis, E.P; Elimelech, M. *Applied Materials & Interfaces* **2011**, 3, 2861-2868.
11. Srivastava, S.; Kotov, N.A. *Accounts of Chemical Research* **2008**, 41, 1831-1841.

12. de Belder, A.N. *Dextran* **2003**, Amersham Biosciences Collection.

13. Xenopoulos, A.; Blanchard M. *Desalination* **2006**, 199, 219.

14. Bakhshayeshi, M.; Zhou, H.; Olsen, C.; Yuan, W.; Zydney, A.L. *Journal of Membrane Science* **2011**, 385–386, 243–250.

15. Zydney, A. L.; Xenopoulos, A. *Journal of Membrane Science* **2007**, 291, 180–190.

16. Bakhshayeshi, M.; Kanani, D.; Mehta, A.; van Reis, R.; Kuriyel, R.; Jackson, N.; Zydney, A.L. *Journal of Membrane Science* **2011**, 379, 239–248.

17. Greenlee, L.F.; Lawler, D.F.; Freeman, B.D; Marrot, B.; Moulin, P. *Water Research* **2009**, 43, 2317-2348.

18. Geise, G.M.; Park, H.B.; Sagle, A.C.; Freeman, B.D.; McGrath, J.E. *Journal of Membrane Science* **2011**, 369, 130-138.

19. Van der Bruggen, B.; Manttari, M.; Nystrom, M. *Separation and Purification Technology* **2008**, 63, 251-263.

20. Schaep, J.; Vandecasteele, C.; Mohammad, A.W.; Bowen, R. *Separation and Purification Technology* **2001**, 22-23, 169–179.

21. Kim, S.; Marion, M.; Byeong-Heon, J.; Hoek, E.M.V. *Journal of Membrane Science* **2006**, 284, 361–372.

22. Arena, J.T.; McCloskey, B.; Freeman, B.D.; McCutcheon, J.R. *Journal of Membrane Science* **2011**, 375, 55-62.

23. Thorsen, T; Fløgstad, H. *Nanofiltration in Drinking Water Treatment* **2006**.

24. Ulbricht, M. *Polymer* **2006**, 47, 2217-2262.

Substrate	Polyelectrolyte PE pre-coat (PAH/PAA)	Cationic Nanoparticles	Anionic Nanoparticles	Number bilayers	Post Treatment
PCTE 0.2 μm	NA	NA	NA	NA	NA
SPEES®100 KDa	NA	NA	NA	NA	NA
PCTE 0.2 μm	2.5 bilayers	NA	NA	NA	Y
SPEES®100 KDa	2.5 bilayers	NA	NA	NA	Y
PCTE 0.2 μm	2.5 bilayers	Spherical 15 nm Ludox® CL	Spherical 25 nm Ludox® TM	40	Y
PCTE 0.2 μm	2.5 bilayers	Spherical 15 nm Ludox® CL	Elongated Snowtex®-UP	40	Y
SPEES®100 KDa	2.5 bilayers	Spherical 15 nm Ludox® CL	Spherical 25 nm Ludox® TM	40	Y
SPEES®100 KDa	2.5 bilayers	Spherical 15 nm Ludox® CL	Elongated Snowtex®-UP	40	Y

Note 1: NA – Not applicable.
Note 2: Snowtex®–UP: Anionic elongated silica nanoparticles whose dimensions are: 9-15 nm width; 40-100 nm length

Table 3-1. *Summary of all samples tested for dextran rejection.*

Substrate	Polyelectrolyte PE pre-coat (PAH/PAA)	Cationic Nanoparticles	Anionic Nanoparticles	Number bilayers	Post Treatment
SPEES®100 KDa	NA	NA	NA	NA	NA
SPEES®100 KDa	2.5 bilayers	Spherical 15 nm Ludox® CL	Spherical 25 nm Ludox® TM	40	Y

Note 1: NA – Not applicable.

Table 3-2. *Summary of all samples tested for salt rejection.*

Dextrans (MW in KDa)	Supplier	Cat. #	Conc. (g/L)
1.5	Fluka	31412	0.55
6	Fluka	31388	0.65
10	Sigma	D9260	0.65
20	Fluka	31387	0.65
40	Fluka	31389	0.65
70	Fluka	31390	0.6
100	Fluka	09184	0.55
200	Fluka	31398	0.55
500	Fluka	31392	1.10
2000	Sigma	D5376	3

Table 3-3. *Composition of dextran stock solution for stirred-cell permeation tests.*

Membrane	T°C	Water Flow @ 100 psi ml/min	Solution Flow @ 100 psi ml/min	C_f [µS/cm]	C_p [µS/cm]	*Rs* [%]
SPEES®100 KDa Monovalent Challenge	25.0			2102	2101	0.0
SPEES®100 KDa Bivalent Challenge	25.0			2750	2750	0.0
SPEES®100 KDa 40 bl Sph/Sph Monovalent Challenge	25.0	1.6	1.3	2104	1905	9.5
SPEES®100 KDa 40 bl Sph/Sph Bivalent Challenge	25.0	1.7	1.2	2750	2190	20.4

Table 3-4. *Summary of all SPEES 100 KDa based samples tested for cross flow permeation challenging monovalent (NaCl 1 g/L) and bivalent salts ($MgSO_4$ 2 g/L).*

a)

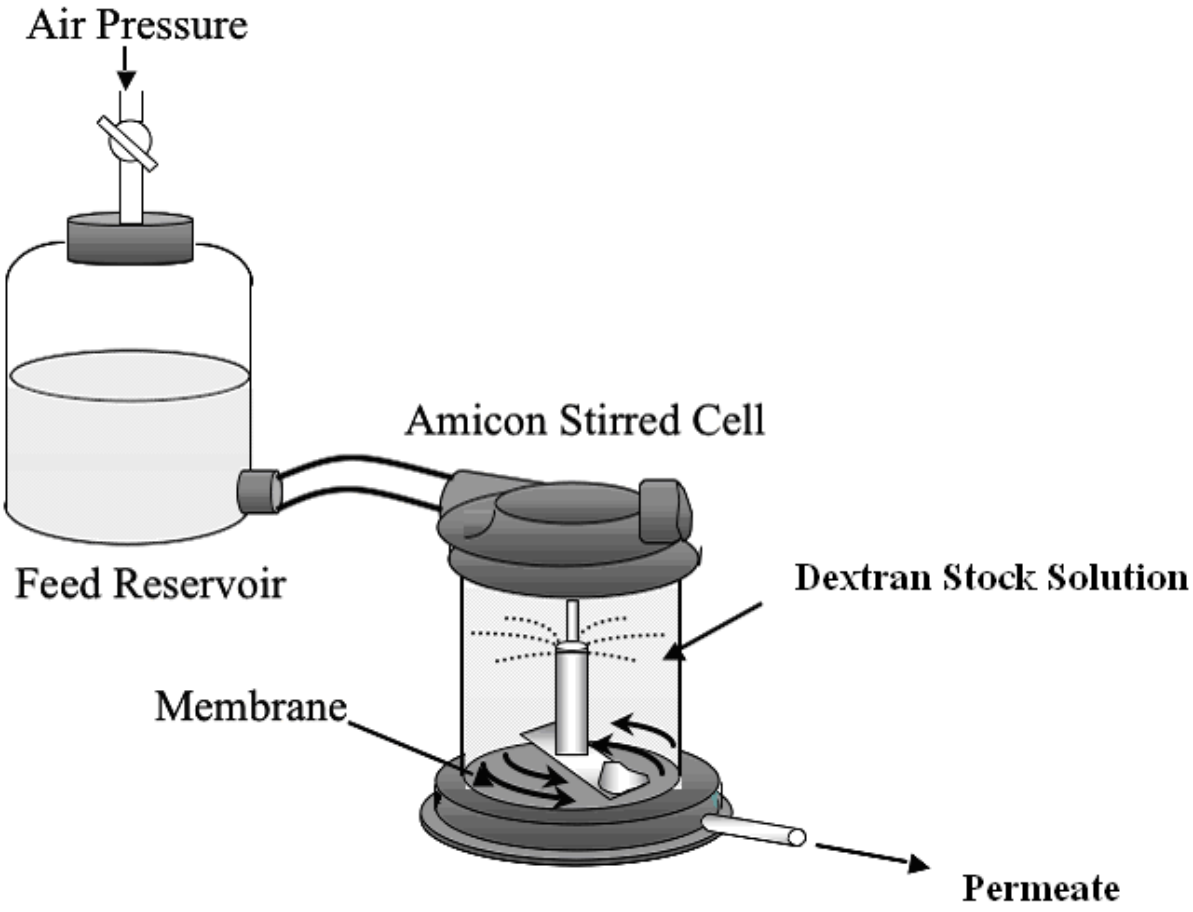
Air Pressure
Amicon Stirred Cell
Feed Reservoir
Dextran Stock Solution
Membrane
Permeate

b)

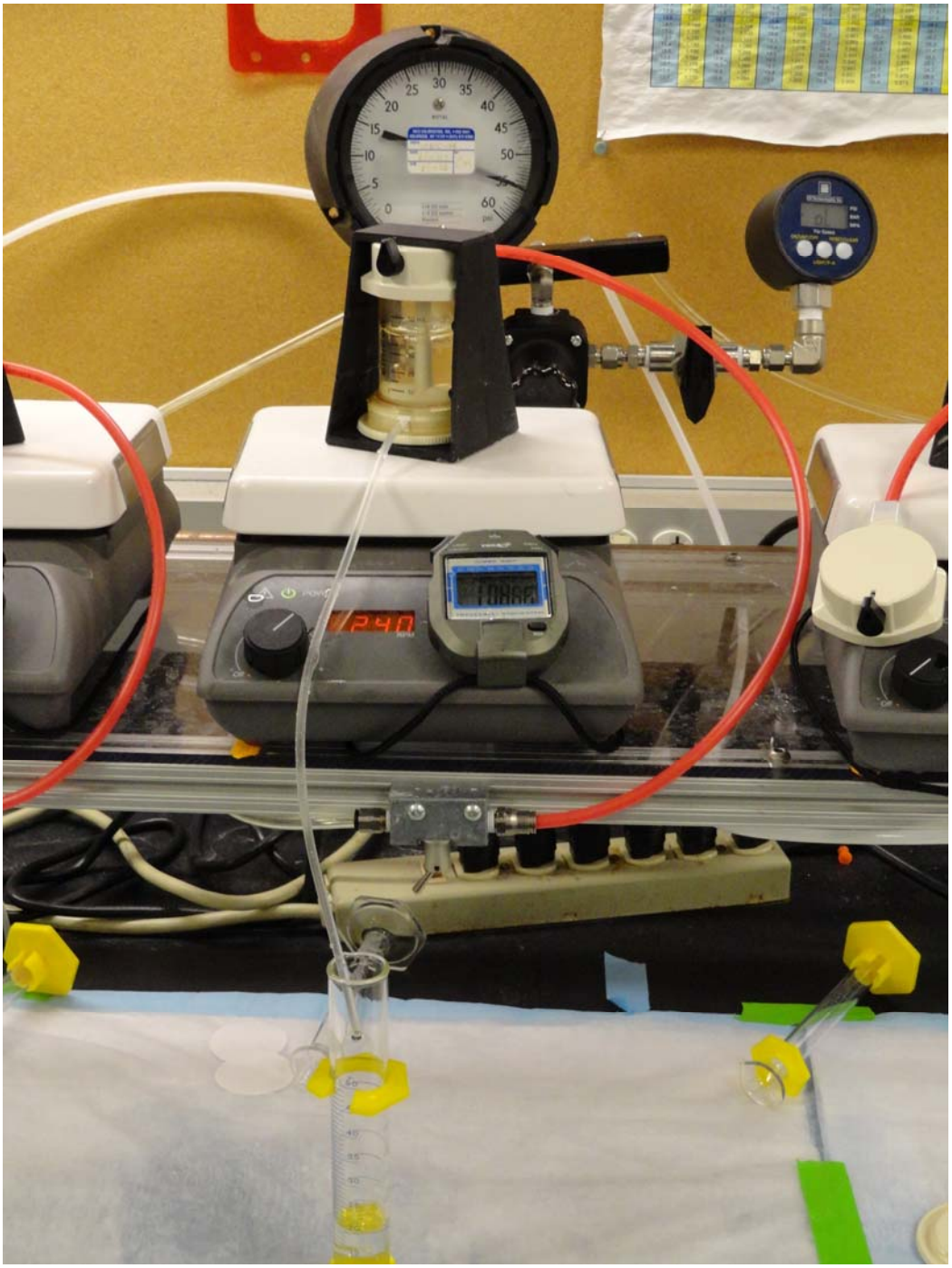

Figure 3-1. *Setup of dead end permeation with Amicon stirred cells. a) Schematic of dead-end permeation using stirred cells for dextran rejection selectivity experiments; b) Equipment installed in operation for porous substrates and TFC membranes..*

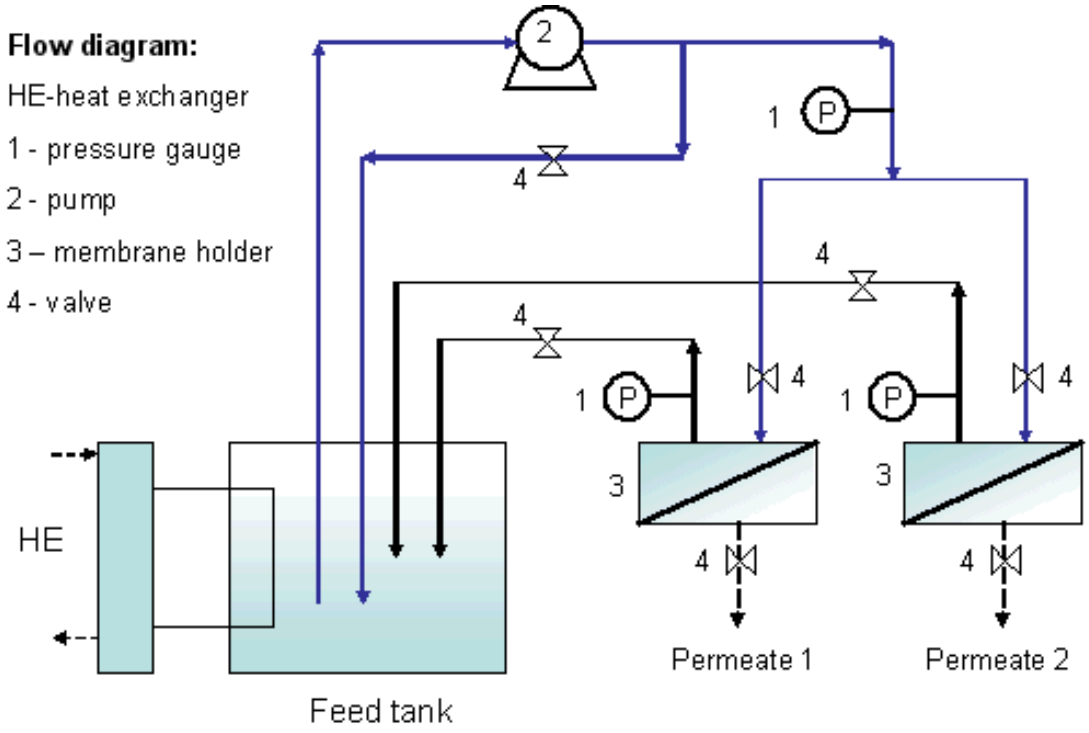

Figure 3-2. *Schematic of the cross flow permeation setup designed to measure monovalent and bivalent salt selectivity for uncoated substrates and TFC membranes.*

a)

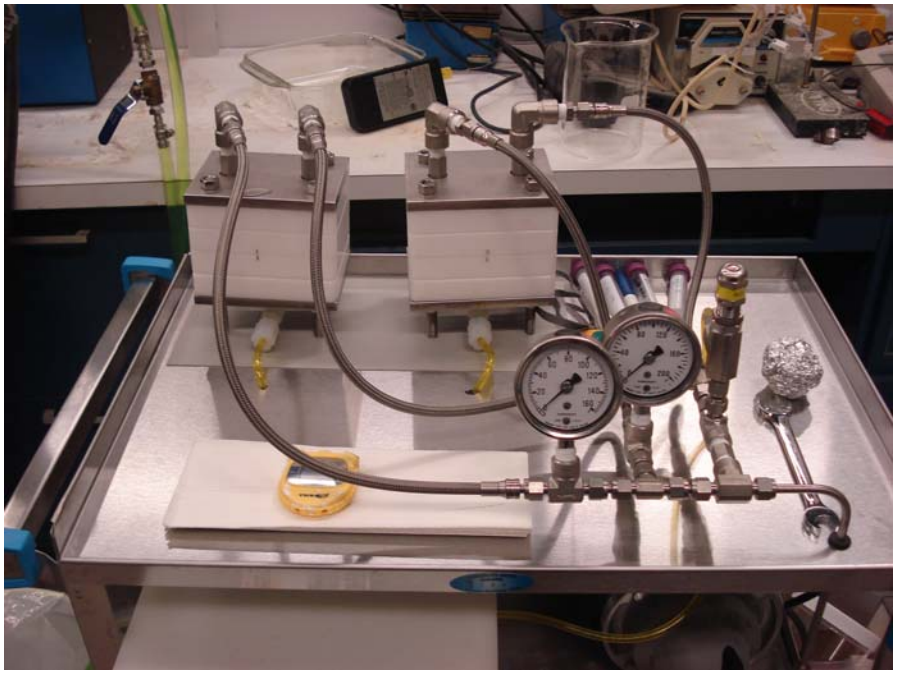

b)

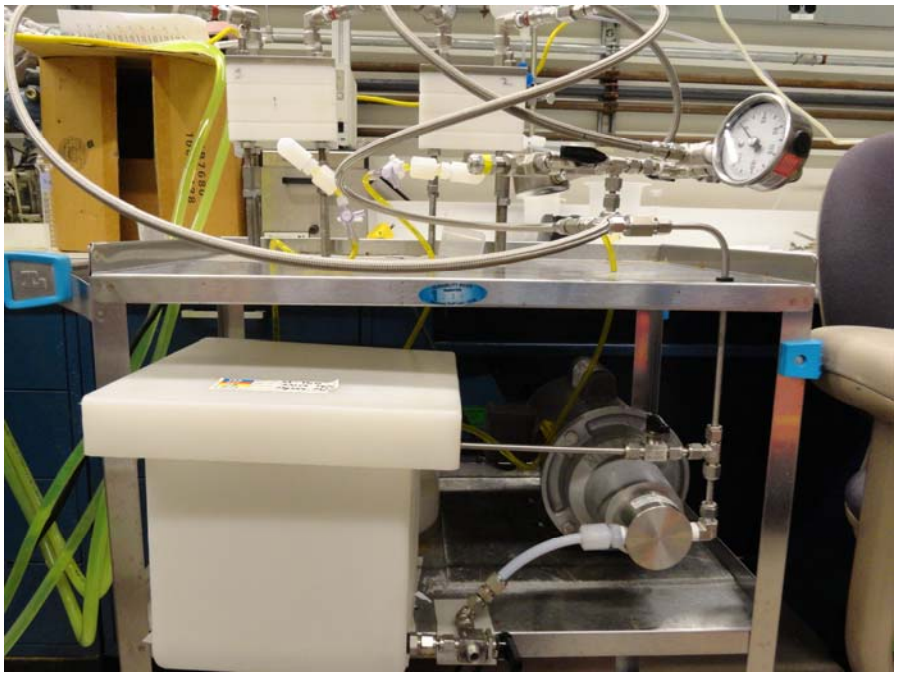

c)

Figure 3-3. *Cross flow permeation equipment designed for selectivity experiments. (a) and (b) cross flow system setup; (c) cross flow membrane holder showing a SPPES based TFC membrane aligned and ready to be tested. The red rectangular sealing ring defines the membrane filtration area.*

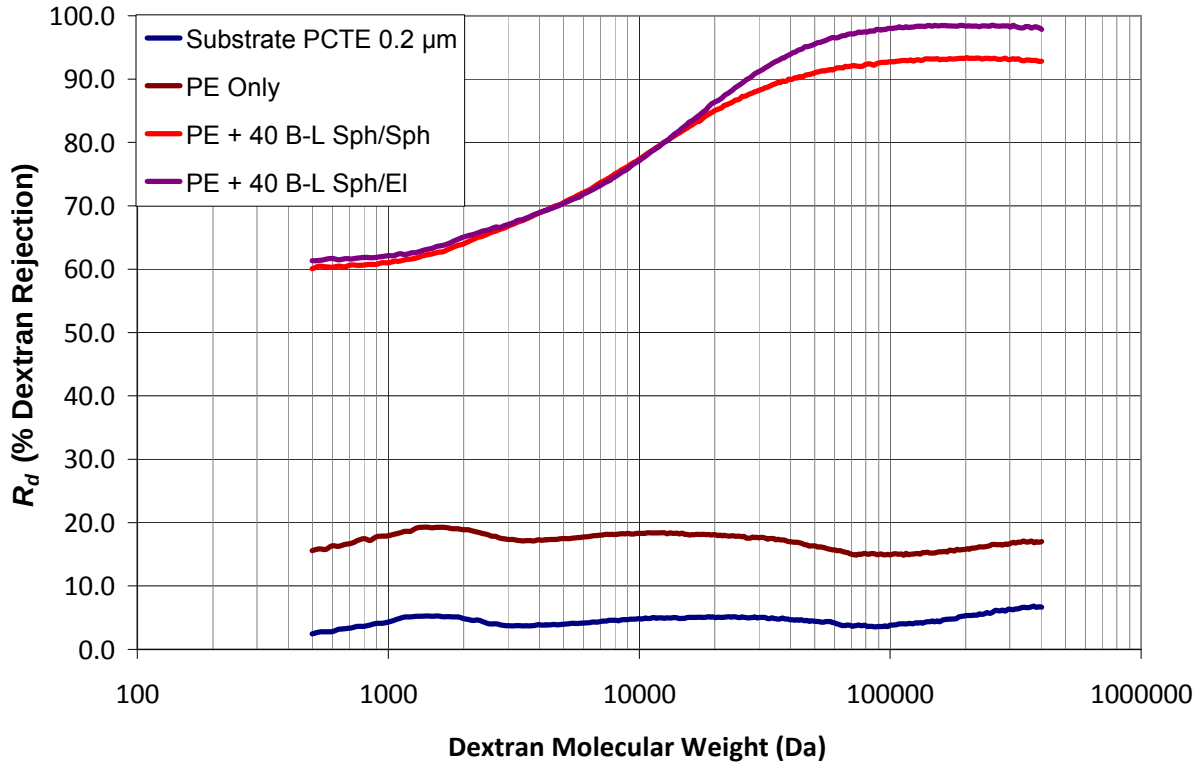

Figure 3-4. *Dextrans rejection R_d vs. molecular weight at 25°C for PCTE 0.2 µm uncoated substrate, and after substrate modification with 2.5 bilayers of the polyelectrolytes PAA and PAH, and with 40 bilayers of Ludox CL/Ludox TM (cationic/anionic) spherical/spherical silica nanoparticles or with 40 bilayers of Ludox CL/Snowtex UP (cationic/anionic) spherical/elongated silica nanoparticles.*

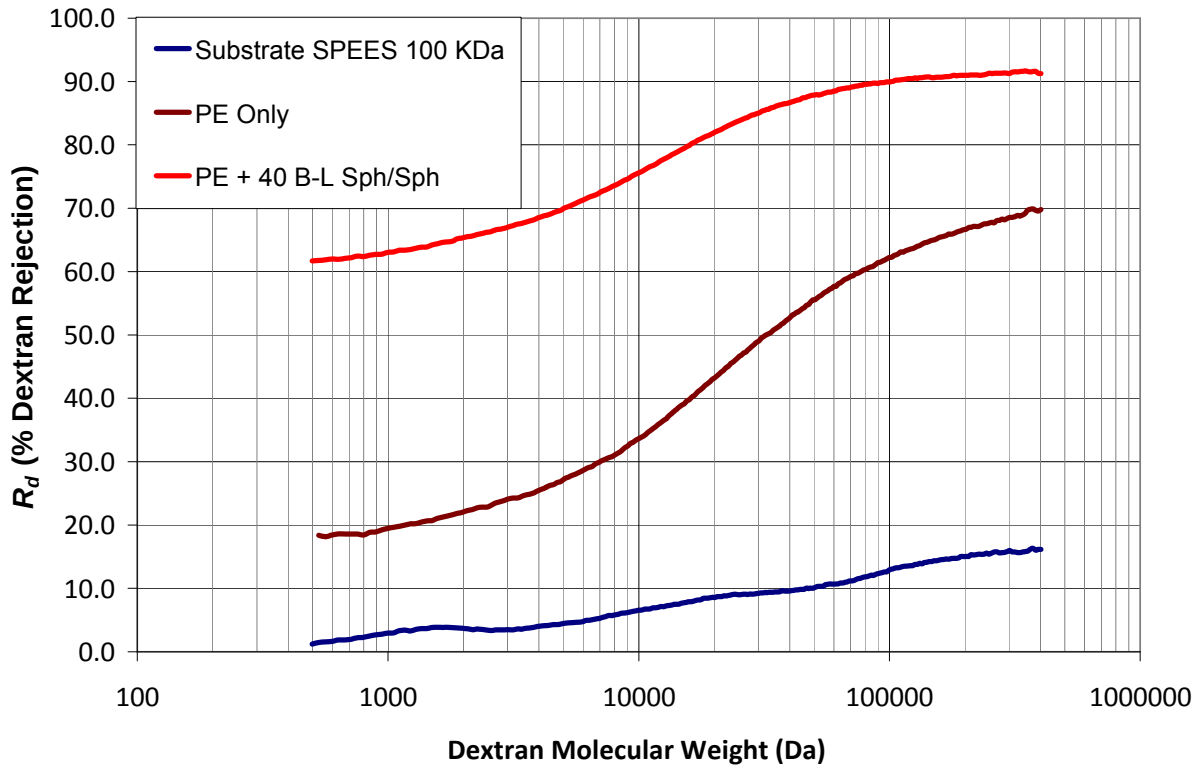

Figure 3-5. *Dextran rejection selectivity R_d vs. molecular weight at 25°C for SPEES 100 KDa uncoated substrate, and after substrate modification with 2.5 bilayers of the polyelectrolytes PAA and PAH, and with 40 bilayers of Ludox CL/Ludox TM (cationic/anionic) spherical/spherical silica nanoparticles.*

Chapter 4. Theory of Pressure Driven Multicomponent Mass Transport Across Membranes

Abstract

In an effort to develop a rigorous theoretical treatment for nanofiltration (NF) and reverse osmosis (RO) processes that includes well defined molecular-level parameters we applied the Curtiss and Bird (CB) multicomponent flux laws[1] which explicitly include the effects of a pressure drop. The multicomponent diffusivities encountered in the CB theory for an isothermal system have been connected with component self diffusion coefficients. This involves going from the CB multicomponent diffusivities to the "Stefan Maxwell" multicomponent diffusivities, and then to the friction coefficients defined by Kirkwood and Bearman[2]. Transformation to the component self diffusion coefficients follows from the use of a geometric mean mixing rule for the multicomponent cross friction coefficients. The important output defines the essential transport coefficients needed to determine the steady flux of species through a membrane under an applied pressure drop. Importantly, introducing the component self diffusion coefficients allow connection to the free volume framework which permits quantitative assessment of the effects of temperature and composition on the transport. Three practically important limits of the final result for a ternary system are developed: Infinitely diluted trace components in a membrane; finite, dilute concentrations of traces, and cross linked membranes. The results for a multicomponent system at infinite dilution are also deduced by an inductive argument. Future experimental scrutiny of these results will permit a better understanding of the key factors optimizing contaminant rejection in NF and RO processes, including desalination.

4.1 Introduction

For pressure driven membrane separation processes, the separation mechanisms are either hydrodynamic "filtration" of dissolved contaminants from the feed and/or the selective partitioning and diffusion through the membrane of feed components. For the high pressure drop processes of nanofiltration (NF) and reverse osmosis (RO), the transport mechanism is thought to be controlled mainly by partitioning/diffusion since typically no open channels exist in these membranes.[3-6]

There have been a few prior efforts to model multicomponent mass transfer across membranes to include from first principles the effects of a pressure drop.[3, 7] Cussler's book[8] provides a review of the basic ideas. Few are cast in terms of transport properties with clear molecular level interpretations, and none appear with properties that are easily measured or estimated in simple experiments apart from the actual separation processes.

The main goal of this work is to develop a framework that provides better understanding of the key transport properties that govern NF and RO processes to enable greater capability to engineer membranes in the NF/RO range for specific applications. A practical approach is to apply a rigorous form of the general multicomponent species flux laws derived from statistical mechanics, to the case of a three components fluid system (ternary case) to include the membrane and two fluid components to be separated by the membrane.

A statistical mechanically based treatment can include the pressure effect to cover NF and RO applications. By examining the ternary case, the transport coefficients appearing in the theory can be connected to more familiar self-diffusion coefficients.[9-11] This permits exploiting a body of work developed for correlation and prediction of mutual diffusion

coefficients to the case of pressure driven ternary mass transport. Generalizations to quaternary systems or higher, can then be pursued.

4.2 Overview of Model Development

We adapt the Curtiss-Bird (CB) theory for the multi-component flux relations,[1] as described above. The CB formalism is exploited as a route to writing the thermodynamically "correct" multi-component diffusive flux laws for an isothermal ternary system. These include a matrix of multicomponent diffusivities, $\tilde{D}_{ij}$. We then introduce the self diffusion coefficients, D_i employed in the free volume theory of Vrentas and Duda.[9] in lieu of the $\tilde{D}_{ij}$.

A connection between the $\tilde{D}_{ij}$ and the D_i is developed using the relationship between another of the CB transport coefficient matrices related to the $\tilde{D}_{ij}$, the "Stefan Maxwell" diffusivities, $\tilde{C}_{ij}$, and the friction coefficients matrix, ζ_{ij}, together with an empirical geometric mean rule connecting cross to self friction coefficients. The well known result for a binary system[9] is recovered from this approach and the explicit relationships for the ternary case are established. The results for the ternary case are verified to be consistent with the non-equilibrium thermodynamic restrictions discussed by Vrentas and Vrentas.[12, 13] Three practically important limits are then explored: infinitely dilute trace components in a membrane limit, dilute but finite concentration of components, i.e. a "weakly" nonlinear limit and a solid membrane limit. Finally an inductive generalization of the ternary flux law for the infinitely dilute trace limit is given for multicomponent systems. The last result permits rudimentary modeling of a desalination process, where there are four components at a minimum: Membrane, water, anionic solute, and cationic solute. The symbols employed in

what follows are consistent with original literature when possible and defined in an appended table.

4.3 Fluxes in a Ternary System

The multicomponent diffusivities ($\tilde{D}_{ij}$) shown in (4-1) are based on a symmetric definition given by Curtiss in 1968.[14]

$$\tilde{D}_{ij} = \frac{cRT\alpha_{ij}}{\rho_i \rho_j} \tag{4-1}$$

These obey the following:

$$\tilde{D}_{ij} = \tilde{D}_{ji} \tag{4-2}$$

$$\sum_{i=1}^{N} \omega_i \tilde{D}_{ij} = 0 \tag{4-3}$$

The CB multicomponent flux laws establish the relation between the mass flux of component *i* in the barycentric frame of reference, j_i, and the driving forces as follow:[1]

$$j_i = -D_i^T \nabla \ln T - \rho_i \sum_{j=1}^{N} \tilde{D}_{ij} d_j \tag{4-4}$$

The diffusional driving force, d_i, has units $[=]\frac{1}{L}$ and the $\tilde{D}_{ij}[=]\frac{L^2}{t}$.

The following analysis assumes isothermal conditions with no external body forces applied. Subscripts 1 and 2 indicate feed components while subscript 3 corresponds to the membrane material. The last is frequently high molecular weight or cross-linked polymer. Accordingly, for a ternary case (4-4) reduces to:

$$\begin{aligned} j_1 &= -\rho_1\left(\tilde{D}_{11} d_1 + \tilde{D}_{12} d_2 + \tilde{D}_{13} d_3\right) \\ j_2 &= -\rho_2\left(\tilde{D}_{21} d_1 + \tilde{D}_{22} d_2 + \tilde{D}_{23} d_3\right) \\ j_3 &= -\rho_3\left(\tilde{D}_{31} d_1 + \tilde{D}_{32} d_2 + \tilde{D}_{33} d_3\right) \end{aligned} \tag{4-5}$$

4.3.1 Analysis of Diffusional Driving Forces d_i

From the CB theory[1]:

$$cRTd_i = c_i RT\sum_{j=1}^{v-1}\left(\frac{\partial \ln a_i}{\partial x_j}\right)_{T,P,x}\nabla x_j + (c_i\overline{v_i} - \omega_i)\nabla P - \rho_i g_i - \omega_i\sum_{j=1}^{v}\rho_j g_j \tag{4-6}$$

The third and fourth terms on the right hand side of (4-6) can be neglected when external body fields are absent. Consequently,

$$d_i = x_i\sum_{j=1}^{v-1}\left(\frac{\partial \ln a_i}{\partial x_j}\right)_{T,P,x}\nabla x_j + \frac{\left(c_i\overline{v_i} - \omega_i\right)}{cRT}\nabla P \tag{4-7}$$

Since activities a_i are defined $\mu_i = \mu_i^0 + RT\ln a_i$ then

$$d_1 = \frac{x_1}{RT}\left[\left(\frac{\partial\mu_1}{\partial x_1}\right)\nabla x_1 + \left(\frac{\partial\mu_1}{\partial x_2}\right)\nabla x_2\right] + \frac{\left(c_1\overline{v_1} - \omega_1\right)}{cRT}\nabla P \tag{4-8}$$

$$d_2 = \frac{x_2}{RT}\left[\left(\frac{\partial\mu_2}{\partial x_1}\right)\nabla x_1 + \left(\frac{\partial\mu_2}{\partial x_2}\right)\nabla x_2\right] + \frac{\left(c_2\overline{v_2} - \omega_2\right)}{cRT}\nabla P \tag{4-9}$$

$$d_3 = \frac{x_3}{RT}\left[\left(\frac{\partial\mu_3}{\partial x_1}\right)\nabla x_1 + \left(\frac{\partial\mu_3}{\partial x_2}\right)\nabla x_2\right] + \frac{\left(c_3\overline{v_3} - \omega_3\right)}{cRT}\nabla P \tag{4-10}$$

where partial derivatives are at fixed $T, P, x_{k\neq j}$. This shows that diffusional driving forces satisfy $\sum_i d_i = 0$.

Using this we have:

$$d_3 = -\left(d_1 + d_2\right) \tag{4-11}$$

and replacing in the first of Eq. (4-5) gives:

$$j_1 = -\rho_1\left(\left(\tilde{D}_{11} - \tilde{D}_{13}\right)d_1 + \left(\tilde{D}_{12} - \tilde{D}_{13}\right)d_2\right) \tag{4-12}$$

for example, putting Eqs. (4-8) – (4-10) into (4-12) gives:

$$j_1 = -\rho_1 \left(\begin{array}{l} \left(\tilde{D}_{11} - \tilde{D}_{13} \right) \left(\frac{x_1}{RT} \left[\left(\frac{\partial \mu_1}{\partial x_1} \right) \nabla x_1 + \left(\frac{\partial \mu_1}{\partial x_2} \right) \nabla x_2 \right] + \frac{\left(c_1 \overline{v_1} - \omega_1 \right)}{cRT} \nabla P \right) \\ + \left(\tilde{D}_{12} - \tilde{D}_{13} \right) \left(\frac{x_2}{RT} \left[\left(\frac{\partial \mu_2}{\partial x_1} \right) \nabla x_1 + \left(\frac{\partial \mu_2}{\partial x_2} \right) \nabla x_2 \right] + \frac{\left(c_2 \overline{v_2} - \omega_2 \right)}{cRT} \nabla P \right) \end{array} \right) \tag{4-13}$$

for the flux of diffusant 1. Reorganizing terms and converting mole to mass fractions, the following are obtained for the two independent feed component mass fluxes:

$$j_1 = -\rho \left(\begin{array}{l} \underbrace{\left[\frac{\omega_1^2 M}{RTM_1} \left(\tilde{D}_{11} - \tilde{D}_{13} \right) \left(\frac{\partial \mu_1}{\partial \omega_1} \right) + \frac{\omega_1 \omega_2 M}{RTM_2} \left(\tilde{D}_{12} - \tilde{D}_{13} \right) \left(\frac{\partial \mu_2}{\partial \omega_1} \right) \right]}_{D_{11}^*} \nabla \omega_1 \\ + \underbrace{\left[\frac{\omega_1^2 M}{RTM_1} \left(\tilde{D}_{11} - \tilde{D}_{13} \right) \left(\frac{\partial \mu_1}{\partial \omega_2} \right) + \frac{\omega_1 \omega_2 M}{RTM_2} \left(\tilde{D}_{12} - \tilde{D}_{13} \right) \left(\frac{\partial \mu_2}{\partial \omega_2} \right) \right]}_{D_{12}^*} \nabla \omega_2 \\ + \underbrace{\left[\frac{\omega_1 M}{\rho RT} \left(\left(\frac{\rho_1 \overline{v_1}}{M_1} - \omega_1 \right) \left(\tilde{D}_{11} - \tilde{D}_{13} \right) + \left(\frac{\rho_2 \overline{v_2}}{M_2} - \omega_2 \right) \left(\tilde{D}_{12} - \tilde{D}_{13} \right) \right) \right]}_{D_{P1}} \nabla P \end{array} \right) \tag{4-14}$$

$$j_2 = -\rho \left(\begin{array}{l} \underbrace{\left[\frac{\omega_1^2 M}{RTM_1} \left(\tilde{D}_{12} - \tilde{D}_{23} \right) \left(\frac{\partial \mu_1}{\partial \omega_1} \right) + \frac{\omega_1 \omega_2 M}{RTM_2} \left(\tilde{D}_{22} - \tilde{D}_{23} \right) \left(\frac{\partial \mu_2}{\partial \omega_1} \right) \right]}_{D_{21}^*} \nabla \omega_1 \\ + \underbrace{\left[\frac{\omega_1^2 M}{RTM_1} \left(\tilde{D}_{12} - \tilde{D}_{23} \right) \left(\frac{\partial \mu_1}{\partial \omega_2} \right) + \frac{\omega_1 \omega_2 M}{RTM_2} \left(\tilde{D}_{22} - \tilde{D}_{23} \right) \left(\frac{\partial \mu_2}{\partial \omega_2} \right) \right]}_{D_{22}^*} \nabla \omega_2 \\ + \underbrace{\left[\frac{\omega_1 M}{\rho RT} \left(\left(\frac{\rho_1 \overline{v_1}}{M_1} - \omega_1 \right) \left(\tilde{D}_{12} - \tilde{D}_{23} \right) + \left(\frac{\rho_2 \overline{v_2}}{M_2} - \omega_2 \right) \left(\tilde{D}_{22} - \tilde{D}_{23} \right) \right) \right]}_{D_{P2}} \nabla P \end{array} \right) \tag{4-15}$$

Recall j_3 follows from $-\left(j_1 + j_2\right)$. These connect phenomenologically defined multicomponent diffusivities D_{ij}^* to the CB diffusivities, $\tilde{D}_{ij}$.

4.4 Phenomenological Transport Coefficients, D_{ij}^* and D_{Pi}

The phenomenological coefficients D_{ij}^* appearing in the mass flux expressions for components 1 and 2 in Eqs. (4-14) and (4-15), relate the mass fraction gradients to the fluxes. In matrix notation,

$$j^P = -\rho D^* \cdot \nabla \omega$$

$$j^P = \begin{bmatrix} j_1^P \\ j_2^P \end{bmatrix}$$

with the superscript indicating constant total pressure conditions, and

$$\nabla \omega = \begin{bmatrix} \nabla \omega_1 \\ \nabla \omega_2 \end{bmatrix}.$$

Also,

$$D^* = \begin{pmatrix} D_{11}^* & D_{12}^* \\ D_{21}^* & D_{22}^* \end{pmatrix}$$

with,

$$D_{11}^* = \frac{M\omega_1}{RT}\left[\frac{\omega_1}{M_1}\tilde{D}_{11}\left(\frac{\partial \mu_1}{\partial \omega_1}\right) + \frac{\omega_2}{M_2}\tilde{D}_{12}\left(\frac{\partial \mu_2}{\partial \omega_1}\right) - \left(\frac{\omega_1}{M_1}\left(\frac{\partial \mu_1}{\partial \omega_1}\right) + \frac{\omega_2}{M_2}\left(\frac{\partial \mu_2}{\partial \omega_1}\right)\right)\tilde{D}_{13}\right] \tag{4-16}$$

$$D_{12}^* = \frac{M\omega_1}{RT}\left[\frac{\omega_1}{M_1}\tilde{D}_{11}\left(\frac{\partial \mu_1}{\partial \omega_2}\right) + \frac{\omega_2}{M_2}\tilde{D}_{12}\left(\frac{\partial \mu_2}{\partial \omega_2}\right) - \left(\frac{\omega_1}{M_1}\left(\frac{\partial \mu_1}{\partial \omega_2}\right) + \frac{\omega_2}{M_2}\left(\frac{\partial \mu_2}{\partial \omega_2}\right)\right)\tilde{D}_{13}\right] \tag{4-17}$$

$$D_{21}^* = \frac{M\omega_1}{RT}\left[\frac{\omega_1}{M_1}\tilde{D}_{12}\left(\frac{\partial \mu_1}{\partial \omega_1}\right) + \frac{\omega_2}{M_2}\tilde{D}_{22}\left(\frac{\partial \mu_2}{\partial \omega_1}\right) - \left(\frac{\omega_1}{M_1}\left(\frac{\partial \mu_1}{\partial \omega_1}\right) + \frac{\omega_2}{M_2}\left(\frac{\partial \mu_2}{\partial \omega_1}\right)\right)\tilde{D}_{23}\right] \tag{4-18}$$

$$D_{22}^* = \frac{M\omega_1}{RT}\left[\frac{\omega_1}{M_1}\tilde{D}_{12}\left(\frac{\partial \mu_1}{\partial \omega_2}\right) + \frac{\omega_2}{M_2}\tilde{D}_{22}\left(\frac{\partial \mu_2}{\partial \omega_2}\right) - \left(\frac{\omega_1}{M_1}\left(\frac{\partial \mu_1}{\partial \omega_2}\right) + \frac{\omega_2}{M_2}\left(\frac{\partial \mu_2}{\partial \omega_2}\right)\right)\tilde{D}_{23}\right] \tag{4-19}$$

The transport coefficients giving the contribution to the feed component fluxes because of a total pressure gradient are

$$D_{P1} = \frac{\omega_1 M}{\rho RT}\left[\left(\frac{\rho_1 \overline{v_1}}{M_1} - \omega_1\right)\left(\tilde{D}_{11} - \tilde{D}_{13}\right) + \left(\frac{\rho_2 \overline{v_2}}{M_2} - \omega_2\right)\left(\tilde{D}_{12} - \tilde{D}_{13}\right)\right] \tag{4-20}$$

$$D_{P2} = \frac{\omega_1 M}{\rho RT}\left[\left(\frac{\rho_1 \overline{v_1}}{M_1} - \omega_1\right)\left(\tilde{D}_{12} - \tilde{D}_{23}\right) + \left(\frac{\rho_2 \overline{v_2}}{M_2} - \omega_2\right)\left(\tilde{D}_{22} - \tilde{D}_{23}\right)\right] \tag{4-21}$$

4.4.1 Phenomenological Coefficients in Terms of Self Diffusion Coefficients, D_i

The CB "Fickian" diffusivities ($\tilde{D}_{ij}$) are related with the "Stefan-Maxwell" diffusivities ($\tilde{C}_{ij}$) as summarized by Curtiss.[14]

$$\tilde{D}_{11} = \frac{\omega_3^2 \tilde{C}_{12} + \omega_2^2 \tilde{C}_{13} + (\omega_2 + \omega_3)^2 \tilde{C}_{23}}{\Delta_3} \tag{4-22}$$

$$\tilde{D}_{12} = \frac{\omega_3^2 \tilde{C}_{12} - \omega_2(\omega_1 + \omega_3)\tilde{C}_{13} - \omega_1(\omega_2 + \omega_3)\tilde{C}_{23}}{\Delta_3} \tag{4-23}$$

$$\tilde{D}_{13} = \frac{\omega_2^2 \tilde{C}_{13} - \omega_3(\omega_1 + \omega_2)\tilde{C}_{12} - \omega_1(\omega_2 + \omega_3)\tilde{C}_{23}}{\Delta_3} \tag{4-24}$$

$$\tilde{D}_{22} = \frac{\omega_3^2 \tilde{C}_{12} + \omega_1^2 \tilde{C}_{23} + (\omega_1 + \omega_3)^2 \tilde{C}_{13}}{\Delta_3} \tag{4-25}$$

$$\tilde{D}_{23} = \frac{\omega_1^2 \tilde{C}_{23} - \omega_3(\omega_1 + \omega_2)\tilde{C}_{12} - \omega_2(\omega_1 + \omega_3)\tilde{C}_{13}}{\Delta_3} \tag{4-26}$$

$$\Delta_3 = \tilde{C}_{12}\tilde{C}_{13} + \tilde{C}_{12}\tilde{C}_{23} + \tilde{C}_{13}\tilde{C}_{23} \tag{4-27}$$

In turn the $\tilde{C}_{ij}$ are related to the friction coefficients (ζ_{ij}) defined by Bearman and Kirkwood[2] as follows:

$$\tilde{C}_{ij} = \frac{n\zeta_{ij}x_i x_j}{kT} = \frac{cN_A^2\zeta_{ij}x_i x_j}{RT} \tag{4-28}$$

Therefore the D_{ij}^* can be expressed entirely in terms of the ζ_{ij} in lieu of the $\tilde{D}_{ij}$. The result for D_{11}^* is shown in Eq. (4-29); Appendix A gives some details of the development. Analogous results can be written for the three other D_{ij}^*.

$$D_{11}^{*}=\frac{\omega_1}{\rho N_A^2\left(\zeta_{12}\zeta_{13}\frac{\omega_1}{M_1}+\zeta_{12}\zeta_{23}\frac{\omega_2}{M_2}+\zeta_{13}\zeta_{23}\frac{\omega_3}{M_3}\right)}\left[\begin{array}{l}\left(\omega_1\frac{M_3}{M_1}\zeta_{12}+(\omega_2+\omega_3)\zeta_{23}\right)\left(\frac{\partial\mu_1}{\partial\omega_1}\right)\\+\left(\omega_2\frac{M_3}{M_2}\zeta_{12}+\omega_2\zeta_{13}\right)\left(\frac{\partial\mu_2}{\partial\omega_1}\right)\end{array}\right] \tag{4-29}$$

The D_{ij}^{*} can then be expressed in terms of self diffusion coefficients defined by Bearman[15] assuming the validity of a geometric mean rule for the cross friction coefficients in terms of self friction coefficients. The key relations needed and some of the details of the development are summarized in Appendices B and C. The final expressions for multicomponent diffusivities D_{ij}^{*} in terms of the D_i are:

$$D_{11}^{*}=\left[\omega_1\Phi_1\left(\frac{\partial\mu_1}{\partial\omega_1}\right)+\omega_2\Phi_2\left(\frac{\partial\mu_2}{\partial\omega_1}\right)\right]\Phi \tag{4-30}$$

$$D_{12}^{*}=\left[\omega_1\Phi_1\left(\frac{\partial\mu_1}{\partial\omega_2}\right)+\omega_2\Phi_2\left(\frac{\partial\mu_2}{\partial\omega_2}\right)\right]\Phi \tag{4-31}$$

$$D_{21}^{*}=\left[\omega_1\Phi_3\left(\frac{\partial\mu_1}{\partial\omega_1}\right)+\omega_2\Phi_4\left(\frac{\partial\mu_2}{\partial\omega_1}\right)\right]\Phi \tag{4-32}$$

$$D_{22}^{*}=\left[\omega_1\Phi_3\left(\frac{\partial\mu_1}{\partial\omega_2}\right)+\omega_2\Phi_4\left(\frac{\partial\mu_2}{\partial\omega_2}\right)\right]\Phi \tag{4-33}$$

where the following variables are defined:

$$\Phi=\frac{(\rho_1\rho_2\rho_3)^{1/2}(D_1^{\oplus}D_2^{\oplus}D_3^{\oplus})^{1/2}}{RT(M_1M_2M_3)^{1/2}\left(\left(\frac{\rho_1}{M_1D_1^{\oplus}}\right)^{1/2}+\left(\frac{\rho_2}{M_2D_2^{\oplus}}\right)^{1/2}+\left(\frac{\rho_3}{M_3D_3^{\oplus}}\right)^{1/2}\right)} \tag{4-34}$$

$$\Phi_1=\omega_1\frac{M_3}{M_1}\left(\frac{M_1}{\rho_1D_1^{\oplus}}\right)^{1/2}\left(\frac{M_2}{\rho_2D_2^{\oplus}}\right)^{1/2}+(\omega_2+\omega_3)\left(\frac{M_2}{\rho_2D_2^{\oplus}}\right)^{1/2}\left(\frac{M_3}{\rho_3D_3^{\oplus}}\right)^{1/2} \tag{4-35}$$

$$\Phi_2=\omega_1\frac{M_3}{M_2}\left(\frac{M_1}{\rho_1D_1^{\oplus}}\right)^{1/2}\left(\frac{M_2}{\rho_2D_2^{\oplus}}\right)^{1/2}-\omega_1\left(\frac{M_1}{\rho_1D_1^{\oplus}}\right)^{1/2}\left(\frac{M_3}{\rho_3D_3^{\oplus}}\right)^{1/2} \tag{4-36}$$

$$\Phi_3 = \omega_1 \frac{M_3}{M_1}\left(\frac{M_1}{\rho_1 D_1^{\oplus}}\right)^{1/2}\left(\frac{M_2}{\rho_2 D_2^{\oplus}}\right)^{1/2} - \omega_1\left(\frac{M_2}{\rho_2 D_2^{\oplus}}\right)^{1/2}\left(\frac{M_3}{\rho_3 D_3^{\oplus}}\right)^{1/2} \tag{4-37}$$

$$\Phi_4 = \omega_1 \frac{M_3}{M_2}\left(\frac{M_1}{\rho_1 D_1^{\oplus}}\right)^{1/2}\left(\frac{M_2}{\rho_2 D_2^{\oplus}}\right)^{1/2} + \frac{\omega_1}{\omega_2}(\omega_1+\omega_3)\left(\frac{M_1}{\rho_1 D_1^{\oplus}}\right)^{1/2}\left(\frac{M_3}{\rho_3 D_3^{\oplus}}\right)^{1/2} \tag{4-38}$$

Also

$$\left(\frac{\rho_1}{M_1}D_1^{\oplus}\right) \equiv D_1\left(\frac{\rho_1}{M_1} + \frac{\rho_2 D_1}{M_2 D_2} + \frac{\rho_3 D_1}{M_3 D_3}\right) \tag{4-39}$$

$$\left(\frac{\rho_2}{M_2}D_2^{\oplus}\right) \equiv D_2\left(\frac{\rho_1 D_2}{M_1 D_1} + \frac{\rho_2}{M_2} + \frac{\rho_3 D_2}{M_3 D_3}\right) \tag{4-40}$$

$$\left(\frac{\rho_3}{M_3}D_3^{\oplus}\right) \equiv D_3\left(\frac{\rho_1 D_3}{M_1 D_1} + \frac{\rho_2 D_3}{M_2 D_2} + \frac{\rho_3}{M_3}\right) \tag{4-41}$$

The coefficients of pressure gradient are:

$$D_{P1} = \frac{\Phi M_3}{\rho}\left[\left(\frac{\rho_1\overline{v_1}\omega_1}{M_1} + \frac{\rho_2\overline{v_2}\omega_1\omega_3}{M_2} - \omega_1(\omega_1+\omega_2)\right)\left(\frac{M_1}{\rho_1 D_1^{\oplus}}\right)^{1/2}\left(\frac{M_2}{\rho_2 D_2^{\oplus}}\right)^{1/2} + \left(\frac{(\omega_2+\omega_3)}{M_3}\left(\rho_1\overline{v_1} - \omega_1 M_1\left(\frac{\rho_2\overline{v_2}}{M_2}+1\right)\right)\right)\left(\frac{M_2}{\rho_2 D_2^{\oplus}}\right)^{1/2}\left(\frac{M_3}{\rho_3 D_3^{\oplus}}\right)^{1/2} - \left(\frac{\rho_2\overline{v_2}\omega_1(\omega_1+\omega_3) - \omega_1\omega_2 M_2}{M_3}\right)\left(\frac{M_1}{\rho_1 D_1^{\oplus}}\right)^{1/2}\left(\frac{M_3}{\rho_3 D_3^{\oplus}}\right)^{1/2}\right] \tag{4-42}$$

$$D_{P2} = \frac{\Phi M_3}{\rho}\left[\left(\frac{\rho_1\overline{v_1}\omega_1}{M_1} + \frac{\rho_2\overline{v_2}\omega_1\omega_3}{M_2} - \omega_1(\omega_1+\omega_2)\right)\left(\frac{M_1}{\rho_1 D_1^{\oplus}}\right)^{1/2}\left(\frac{M_2}{\rho_2 D_2^{\oplus}}\right)^{1/2} + \left(\frac{(\omega_2+\omega_3)}{M_3}\left(\rho_1\overline{v_1} - \omega_1 M_1\left(\frac{\rho_2\overline{v_2}}{M_2}+1\right)\right)\right)\left(\frac{M_2}{\rho_2 D_2^{\oplus}}\right)^{1/2}\left(\frac{M_3}{\rho_3 D_3^{\oplus}}\right)^{1/2} - \left(\frac{\rho_2\overline{v_2}\omega_1(\omega_1+\omega_3) - \omega_1\omega_2 M_2}{M_3}\right)\left(\frac{M_1}{\rho_1 D_1^{\oplus}}\right)^{1/2}\left(\frac{M_3}{\rho_3 D_3^{\oplus}}\right)^{1/2}\right] \tag{4-43}$$

4.5 Practically Important Limiting Cases

Eqs. (4-30) – (4-33) supply the transport coefficients needed to describe isothermal mass transport in a ternary system without the influence of body fields. The effects of composition and total pressure gradients are properly included. The statistical mechanical basis ensures a thermodynamically consistent description, i.e. that the corresponding entropy production is non-negative. In principle, the variation of the transport coefficients with composition and component molecular weight can be fully accounted for via appropriate

descriptions for the $\mu_i = \mu_i(\omega_j, T, P)$ and $D_i = D_i(\omega_j, T, P)$. Implementation of this appears daunting in view of the complexity of the expressions for the D_{ij}^* and D_{Pi} in terms of the μ_i and D_i. We therefore develop limiting approximate forms for these of practical importance.

The limiting cases correspond to likely scenarios for NF and RO applications. The results for ternary systems can handle a binary feed mixture (components 1 and 2) which usually corresponds to water (component 1) and a suspended trace contaminant (component 2). The membrane (component 3) is frequently polymeric, either high molecular weight melt or glass, or crosslinked, i.e. essentially infinite molecular weight. Further, many polymeric NF or RO membranes show low solubility coefficients for water, i.e. the polymer is typically hydrophobic and insoluble in water. Consequently, the limiting cases of interest are:

- trace levels of components 1 and 2 in 3
- infinite molecular weight of component 3

The former can be explored by establishing first the limiting values of D_{ij}^* and D_{Pi} with ω_1, ω_2 taken to zero, and then by determining the first corrections for finite concentrations, linear in ω_1 and ω_2. The latter corrections correspond to a weakly non-linear limit.

4.5.1 Trace Levels of Feed in a Membrane

This case occurs when a system contains almost pure polymer (melt) and the feed solvent plus impurity at infinite dilution. Therefore, for this scenario the following applies:

$$D_{ij}^* = \lim_{\substack{\omega_1, \omega_2 \to 0 \\ \omega_3 \to 1}} \left(D_{ij}^*\right)_{T,P}$$

$$D_{Pi} = \lim_{\substack{\omega_1, \omega_2 \to 0 \\ \omega_3 \to 1}} \left(D_{Pi}\right)$$

One needs the values of $\omega_1\left(\frac{\partial\mu_1}{\partial\omega_1}\right)_{T,P}, \omega_1\left(\frac{\partial\mu_1}{\partial\omega_2}\right)_{T,P}, \omega_2\left(\frac{\partial\mu_2}{\partial\omega_1}\right)_{T,P}$ and $\omega_2\left(\frac{\partial\mu_2}{\partial\omega_2}\right)_{T,P}$ appearing in the D_{ij}^* (see Eqs. (4-30) - (4-33)). For this purpose the following general relations are assumed:

$$\mu_i = \mu_i^0 + RT\ln a_i \tag{4-44}$$

$$a_i = \gamma_i(T, P, \omega_1, \omega_2)\omega_i \tag{4-45}$$

for i=1, 2. The γ_i are weight fraction based activity coefficients.

Then it follows

$$\lim_{\substack{\omega_1,\omega_2\to 0\\ \omega_3\to 1}} \omega_i\left(\frac{\partial\mu_i}{\partial\omega_i}\right)_{T,P,\omega_j} = RT \qquad (i=1, 2; j=1, 2; j\neq i) \tag{4-46}$$

$$\lim_{\substack{\omega_1,\omega_2\to 0\\ \omega_3\to 1}} \omega_i\left(\frac{\partial\mu_i}{\partial\omega_j}\right)_{T,P,\omega_i} = 0 \qquad (i=1, 2; j=1, 2; j\neq i) \tag{4-47}$$

Also, one needs the trace limits of $D_i^{\oplus}$, Φ and the Φ_i given by Eqs. (4-34) - (4-41). These are developed in Appendix D. From this results one can establish, for example

$$\lim_{\substack{\omega_1,\omega_2\to 0\\ \omega_3\to 1}} D_{11}^* = \left[\left(\lim_{\substack{\omega_1,\omega_2\to 0\\ \omega_3\to 1}} \Phi_1\right)\left(\lim_{\substack{\omega_1,\omega_2\to 0\\ \omega_3\to 1}} \omega_1\frac{\partial\mu_1}{\partial\omega_1}\right) + \left(\lim_{\substack{\omega_1,\omega_2\to 0\\ \omega_3\to 1}} \Phi_2\right)\left(\lim_{\substack{\omega_1,\omega_2\to 0\\ \omega_3\to 1}} \omega_2\frac{\partial\mu_2}{\partial\omega_2}\right)\right]\lim_{\substack{\omega_1,\omega_2\to 0\\ \omega_3\to 1}} \Phi \tag{4-48}$$

$$\boxed{\lim_{\substack{\omega_1,\omega_2\to 0\\ \omega_3\to 1}} D_{11}^* = D_1^{\infty} \equiv D_{11}^{*\infty}} \tag{4-49}$$

where the superscript indicates the trace value.

Following the same procedure for the D_{ij}^* one finds:

$$\boxed{\lim_{\substack{\omega_1,\omega_2\to 0\\ \omega_3\to 1}} D_{12}^* = 0} \tag{4-50}$$

$$\boxed{\lim_{\substack{\omega_1,\omega_2\to 0\\ \omega_3\to 1}} D_{21}^* = 0} \tag{4-51}$$

$$\boxed{\lim_{\substack{\omega_1,\omega_2\to 0\\ \omega_3\to 1}} D_{22}^* = D_2^{\infty} \equiv D_{22}^{*\infty}} \tag{4-52}$$

The diffusivities due to pressure (D_{P1} & D_{P2}) in this limit, are given by:

$$\lim_{\substack{\omega_1,\omega_2\to 0\\ \omega_3\to 1}} D_{P1} = D_1\left(\frac{\rho_1\overline{v_1}}{RT}\right) \tag{4-53}$$

$$\lim_{\substack{\omega_1,\omega_2\to 0\\ \omega_3\to 1}} D_{P2} = D_2\left(\frac{\rho_2\overline{v_2}}{RT}\right) \tag{4-54}$$

So, for infinitely dilute traces in a membrane, the cross diffusion (D_{12}^* & D_{21}^*) terms are negligible and the principal diffusion coefficients (D_{11}^* & D_{22}^*) reduce to the self diffusion coefficients. The pressure diffusion coefficients D_{Pi} become directly proportional to the corresponding self diffusion coefficients in the trace regime but are negligibly small in the limit.

4.5.2 Weakly Non-Linear Trace Limit for a Ternary System

Here we consider that ω_1 and ω_2 are small but finite. Therefore, non linearities with respect to composition variables appear in the description of steady transport of species across a membrane. In principle, the asymptotic dependence of the D_{ij}^* and D_{Pi} on ω_1 and ω_2 is obtained via Taylor expansions:

$$D_{ij}^* = D_{ij}^{*\infty} + \omega_1\left(\frac{\partial D_{ij}^*}{\partial\omega_1}\right)_{\substack{\omega_i=0\\ \omega_2=0}} + \omega_2\left(\frac{\partial D_{ij}^*}{\partial\omega_2}\right)_{\substack{\omega_j=0\\ \omega_2=0}} + O(\omega_1^2,\omega_2^2,\omega_1\omega_2) + \ldots\ldots (i=1,2;\ j=1,2) \tag{4-55}$$

$$D_{Pi} = D_{Pi}^{\infty} + \omega_1\left(\frac{\partial D_{Pi}}{\partial\omega_1}\right)_{\substack{\omega_i=0\\ \omega_2=0}} + \omega_2\left(\frac{\partial D_{Pi}}{\partial\omega_2}\right)_{\substack{\omega_j=0\\ \omega_2=0}} + O(\omega_1^2,\omega_2^2,\omega_1\omega_2) + \ldots\ldots (i=1,2;\ j=1,2) \tag{4-56}$$

Retaining only the first three terms and including the trace limit values from the previous section, the asymptotic forms for the weakly non-linear limit are

$$D_{11}^* \cong D_1^{\infty} + \omega_1\left(\frac{\partial D_{11}^*}{\partial\omega_1}\right)_{\substack{\omega_1=0\\ \omega_2=0}} + \omega_2\left(\frac{\partial D_{11}^*}{\partial\omega_2}\right)_{\substack{\omega_1=0\\ \omega_2=0}} \tag{4-57}$$

$$D_{12}^{*} \cong \omega_1 \left(\frac{\partial D_{12}^{*}}{\partial \omega_1} \right)_{\substack{\omega_1=0 \\ \omega_2=0}} + \omega_2 \left(\frac{\partial D_{12}^{*}}{\partial \omega_2} \right)_{\substack{\omega_1=0 \\ \omega_2=0}} \tag{4-58}$$

$$D_{21}^{*} \cong \omega_1 \left(\frac{\partial D_{21}^{*}}{\partial \omega_1} \right)_{\substack{\omega_1=0 \\ \omega_2=0}} + \omega_2 \left(\frac{\partial D_{21}^{*}}{\partial \omega_2} \right)_{\substack{\omega_1=0 \\ \omega_2=0}} \tag{4-59}$$

$$D_{22}^{*} \cong D_2^{\infty} + \omega_1 \left(\frac{\partial D_{22}^{*}}{\partial \omega_1} \right)_{\substack{\omega_1=0 \\ \omega_2=0}} + \omega_2 \left(\frac{\partial D_{22}^{*}}{\partial \omega_2} \right)_{\substack{\omega_1=0 \\ \omega_2=0}} \tag{4-60}$$

$$D_{P1} \cong D_{P1}^{\infty} + \omega_1 \left(\frac{\partial D_{P1}}{\partial \omega_1} \right)_{\substack{\omega_1=0 \\ \omega_2=0}} + \omega_2 \left(\frac{\partial D_{P1}}{\partial \omega_2} \right)_{\substack{\omega_1=0 \\ \omega_2=0}} \tag{4-61}$$

$$D_{P2} \cong D_{P2}^{\infty} + \omega_1 \left(\frac{\partial D_{P2}}{\partial \omega_1} \right)_{\substack{\omega_1=0 \\ \omega_2=0}} + \omega_2 \left(\frac{\partial D_{P2}}{\partial \omega_2} \right)_{\substack{\omega_1=0 \\ \omega_2=0}} \tag{4-62}$$

The derivatives indicated above, are quite complex since all the components of Eqs. (4-30) – (4-33) and (4-42) – (4-43) are dependent on ω_1. Therefore, a reasonable alternative to find the real limits is given by the following relations:

$$D_{11}^{*} \cong D_1^{\infty} + \omega_1 \left(\frac{\partial D_1}{\partial \omega_1} \right)_{\substack{\omega_1=0 \\ \omega_2=0}} + \omega_2 \left(\frac{\partial D_1}{\partial \omega_2} \right)_{\substack{\omega_1=0 \\ \omega_2=0}} \tag{4-63}$$

$$D_{12}^{*} \cong \omega_1 \left(\frac{\partial D_{12}^{*}}{\partial \omega_1} \right)_{\substack{\omega_1=0 \\ \omega_2=0}} + \omega_2 \left(\frac{\partial D_{12}^{*}}{\partial \omega_2} \right)_{\substack{\omega_1=0 \\ \omega_2=0}} \tag{4-64}$$

$$D_{21}^{*} \cong \omega_1 \left(\frac{\partial D_{21}^{*}}{\partial \omega_1} \right)_{\substack{\omega_1=0 \\ \omega_2=0}} + \omega_2 \left(\frac{\partial D_{21}^{*}}{\partial \omega_2} \right)_{\substack{\omega_1=0 \\ \omega_2=0}} \tag{4-65}$$

$$D_{22}^{*} \cong D_2^{\infty} + \omega_1 \left(\frac{\partial D_2}{\partial \omega_1} \right)_{\substack{\omega_1=0 \\ \omega_2=0}} + \omega_2 \left(\frac{\partial D_2}{\partial \omega_2} \right)_{\substack{\omega_1=0 \\ \omega_2=0}} \tag{4-66}$$

$$D_{P1} \cong D_{P1}^{\infty} + \omega_1 \left(\frac{\partial D_{P1}}{\partial \omega_1} \right)_{\substack{\omega_1=0 \\ \omega_2=0}} + \omega_2 \left(\frac{\partial D_{P1}}{\partial \omega_2} \right)_{\substack{\omega_1=0 \\ \omega_2=0}} \tag{4-67}$$

$$D_{P2} \cong D_{P2}^{\infty} + \omega_1 \left(\frac{\partial D_{P2}}{\partial \omega_1} \right)_{\substack{\omega_1=0 \\ \omega_2=0}} + \omega_2 \left(\frac{\partial D_{P2}}{\partial \omega_2} \right)_{\substack{\omega_1=0 \\ \omega_2=0}} \tag{4-68}$$

4.5.3 High Molecular Weight Polymer Limit for a Ternary System

If it is assumed the membrane consists of very high molecular weight polymer, one can justifiably take the following limit of the general results (4-30) - (4-33) and (4-42) – (4-43).

$$\lim_{\substack{M_3 \to \infty \\ D_3 \to 0 \\ D_3 M_3 \to 0}} \left(D_{ij}^{*} \right)_{T,P}; \lim_{\substack{M_3 \to \infty \\ D_3 \to 0 \\ D_3 M_3 \to 0}} \left(D_{Pi} \right)$$

This limit process is consistent with the known dependence of D_3 on M_3 for very high molecular weight polymer melts. It also provides correct limiting values if the membrane is cross-linked polymer.

Appendix E provides the limiting values or asymptotical functional forms of $D_i^{\oplus}$, Φ and Φ_i. Collecting these results leads to:

$$\lim_{\substack{M_3 \to \infty \\ D_3 \to 0 \\ D_3 M_3 \to 0}} D_{11}^{*} = \omega_2 \left[\frac{(1-\omega_1) D_1 M_1 + \omega_1 D_2 M_2}{\omega_1 M_2 + \omega_2 M_1} \right] \tag{4-69}$$

$$\lim_{\substack{M_3 \to \infty \\ D_3 \to 0 \\ D_3 M_3 \to 0}} D_{12}^{*} = -\omega_1 \left[\frac{(1-\omega_1) D_1 M_1 + \omega_1 M_2 D_2}{\omega_1 M_2 + \omega_2 M_1} \right] \tag{4-70}$$

$$\lim_{\substack{M_3 \to \infty \\ D_3 \to 0 \\ D_3 M_3 \to 0}} D_{21}^{*} = -\omega_1 \left[\frac{\omega_2 D_1 M_1 + (1-\omega_2) D_2 M_2}{\omega_1 M_2 + \omega_2 M_1} \right] \tag{4-71}$$

$$\lim_{\substack{M_3 \to \infty \\ D_3 \to 0 \\ D_3 M_3 \to 0}} D_{22}^{*} = \omega_1^2 \left[\frac{\omega_2 D_1 M_1 + (1-\omega_2) D_2 M_2}{\omega_2 (\omega_1 M_2 + \omega_2 M_1)} \right] \tag{4-72}$$

Interestingly, in this limit, the cross diffusion terms are negative.

$$\lim_{\substack{M_3\to\infty \\ D_3\to 0 \\ D_3M_3\to 0}} D_{P1} = D_1\left(\frac{\rho_1\overline{v_1}}{RT}\right) \tag{4-73}$$

$$\lim_{\substack{M_3\to\infty \\ D_3\to 0 \\ D_3M_3\to 0}} D_{P2} = D_2\left(\frac{\rho_2\overline{v_2}}{RT}\right) \tag{4-74}$$

4.6. Conclusions

We presented a development of the diffusive flux laws applicable to NF/RO processes with a statistical mechanical basis that only includes parameters with a well defined molecular level interpretation. This has been constructed by linking the transport properties in Curtiss and Bird's multicomponent flux laws[1] to component self diffusion coefficients. The output defines the essential transport coefficients needed to predict the steady flux of species through a dense membrane under an applied pressure drop. The results were developed explicitly for three components and are consistent with the thermodynamic restrictions cited by Vrentas and Vrentas for the ternary case.[12, 13] The same sequence of steps was also applied to a binary system leading to the well established relationships for an ordinary diffusion flux developed by Vrentas and Duda.[9]

The general results were specialized to three practically relevant limits: Infinitely dilute trace components in a membrane, trace component at small but finite concentrations and the limit of high molecular weight membranes. Future experimental scrutiny of these results will permit a better understanding of the transport mechanisms relevant to NF and RO processes, especially with respect to the effects of fixed charge and water content in membranes.

Nomenclature:

a_i = *activity of component i*
c_i = *molar concentration of component i*
c = $\sum_i c_i$ = *total molar concentration*

$\tilde{C}_{ij}$ = *"Stefan-Maxwell" multicomponent diffusivities [t/L^2]*
d_i = *diffusional driving force [1/L]*
$\tilde{D}_{ij}$ = *"Fickian" multicomponent diffusivities [L^2/t] defined by CB*
D_{ij}^* = *phenomenological multicomponent diffusivities due to concentration*
D_{Pi} = *phenomenological multicomponent diffusivities due to pressure*
D_i = *self diffusion coefficient*
j_i = *mass flux of component i*
k = *Boltzmann's constant*
M = *average molecular weight*
M_i = *molecular weight of component i*
n = *total number density [molecules/L^3] =* cN_A
N_A = *Avogadro's number*
P = *total pressure drop*
R = *universal gases constant*
T = *absolute temperature*
$\hat{V}_i^0$ = *specific volume of pure component i*
$\hat{V}_i$ = *specific volume of component i*
x_i = *molar fraction of component i*

Greek Symbols

α_{ij} = *phenomenological coefficients defined by CB*
γ_i = *activity coefficient of component i*
$\overline{v_i}$ = *partial molar volume of component i*
ρ_i = *density of component i*
ρ = *total density of the mixture*
ζ_{ij} = *friction coefficients*
μ_i = *chemical potential of component i*
μ_i^0 = *reference chemical potential of component i*
ω_i = *mass fraction of component i*

References

1. Curtiss, C.F.; Bird, R.F. *Industrial & Engineering Chemistry Research* **1999,** 38, 2515-2522.

2. Bearman, R.J.; Kirkwood, J.G. *Journal of Physical Chemistry* **1958**, 28, 136-145.

3. Lee, C.H. *Journal of Applied Polymer Science* **1975**, 19, 83-95.

4. Soltanieh, M; Gill, W.N. *Chemical Engineering Communications*, **1981**, 12, 279-363.
5. Greenlee, L.F.; Lawler, D.F.; Freeman, B.D; Marrot, B.; Moulin, P. *Water Research* **2009**, 43, 2317-2348.

6. Li, D.; Wang, H. *Journal of Materials Chemistry*, **2010**, 20, 4561-4566.

7. Vandezande, P.; Gevers, L.E.M.; Vankelecom, I.F.J. *Chemical Society Reviews*, **2008**, 37, 365-405.

8. Cussler, E.L *Diffusion* **2009,** Cambridge University Press, Third Edition.

9. Vrentas, J.S; Duda, J.L. *Journal of Polymer Science: Polymer Physics Edition* **1977,** 15, 403-416.

10. Vrentas, J.S.; Duda, J.L.; Ling, H.C. *Journal of Applied Polymer Science*, **1985**, 30, 4499-4536.

11. Surana, R.K; Danner, R.P; Duda, J.L. *Industrial & Engineering Chemistry Research*, **1998**, *37,* 3203-3207.

12. Vrentas, J.S.; Vrentas, C.M. *Industrial & Engineering Chemistry Research* **2005,** *44,* 1112-1119.

13. Vrentas, J.S.; Vrentas, C.M. *Industrial & Engineering Chemistry Research* **2007,** *46,* 3422-3428.

14. Curtiss, C.F. *Journal of Chemical Physics* **1968**, 49, 2917-2919.

15. Bearman, R.J. *Journal of Physical Chemistry* **1961**, *65,* 1961–1968.

16. Vrentas, J.S.; Duda, J.L.; Ni, L.W. *Macromolecules* **1983**, 16, 261-266.

Appendix-A

Recasting D_{ij}^{*} in terms of ζ_{ij}

Implementing Eqs. (4-22) to (4-24) on the result for D_{11}^{*} in Eq. (4-16) we find,

$$D_{11}^{*}=\frac{M\omega_1}{RT}\left[\begin{array}{l}\dfrac{\omega_1}{M_1}\left(\dfrac{\omega_3^2\tilde{C}_{12}+\omega_2^2\tilde{C}_{13}+(\omega_2+\omega_3)^2\tilde{C}_{23}}{\Delta_3}\right)\left(\dfrac{\partial\mu_1}{\partial\omega_1}\right)\\ +\dfrac{\omega_2}{M_2}\left(\dfrac{\omega_3^2\tilde{C}_{12}+\omega_2(\omega_1+\omega_3)\tilde{C}_{13}+\omega_1(\omega_2+\omega_3)\tilde{C}_{23}}{\Delta_3}\right)\left(\dfrac{\partial\mu_2}{\partial\omega_1}\right)\\ -\left(\dfrac{\omega_1}{M_1}\left(\dfrac{\partial\mu_1}{\partial\omega_1}\right)+\dfrac{\omega_2}{M_2}\left(\dfrac{\partial\mu_2}{\partial\omega_1}\right)\right)\left(\dfrac{\omega_2^2\tilde{C}_{13}-\omega_3(\omega_1+\omega_2)\tilde{C}_{12}-\omega_1(\omega_2+\omega_3)\tilde{C}_{23}}{\Delta_3}\right)\end{array}\right] \tag{A-1}$$

Extracting common factors and reducing terms lead to:

$$D_{11}^{*}=\frac{M\omega_1}{RTM_1M_2\Delta_3}\left[\begin{array}{l}\left(\omega_1M_2\tilde{C}_{12}\left[\omega_3^2+\omega_3(\omega_1+\omega_2)\right]+\omega_1M_2\tilde{C}_{23}\left[(\omega_2+\omega_3)^2+\omega_1(\omega_2+\omega_3)\right]\right)\left(\dfrac{\partial\mu_1}{\partial\omega_1}\right)\\ +\left(\omega_2M_1\tilde{C}_{12}\left[\omega_3^2+\omega_3(\omega_1+\omega_2)\right]-\omega_2M_1\tilde{C}_{13}\left[\omega_2(\omega_1+\omega_3)+\omega_2^2\right]\right)\left(\dfrac{\partial\mu_2}{\partial\omega_1}\right)\end{array}\right] \tag{A-2}$$

Reducing terms further, the following expression is obtained:

$$D_{11}^{*}=\frac{M\omega_1}{RT}\left[\left(\frac{\omega_1\omega_3\tilde{C}_{12}+\omega_1(\omega_2+\omega_3)\tilde{C}_{23}}{M_1\Delta_3}\right)\left(\frac{\partial\mu_1}{\partial\omega_1}\right)+\left(\frac{\omega_2\omega_3\tilde{C}_{12}-\omega_2^2\tilde{C}_{13}}{M_2\Delta_3}\right)\left(\frac{\partial\mu_2}{\partial\omega_1}\right)\right] \tag{A-3}$$

Introducing the friction coefficients on Eq. (4-28) gives,

$$D_{11}^{*}=\frac{\omega_1^2\rho N_A^2M^2}{(RT)^2}\left[\left(\frac{\dfrac{\omega_1\omega_2\omega_3}{M_1M_2}\zeta_{12}+\dfrac{(\omega_2+\omega_3)\omega_2\omega_3}{M_2M_3}\zeta_{23}}{M_1\Delta_3}\right)\left(\frac{\partial\mu_1}{\partial\omega_1}\right)+\left(\frac{\dfrac{\omega_2^2\omega_3}{M_1M_2}\zeta_{12}-\dfrac{\omega_2^2\omega_3}{M_1M_3}\zeta_{13}}{M_2\Delta_3}\right)\left(\frac{\partial\mu_2}{\partial\omega_1}\right)\right] \tag{A-4}$$

The operator Δ_3 contains the $\tilde{C}_{ij}$ diffusivities and is expressed in terms of the friction factors:

$$\Delta_3 = \left(\frac{\rho N_A^2}{MRT}\right)^2 \frac{M^4 \omega_1 \omega_2 \omega_3}{M_1 M_2 M_3}\left[\zeta_{12}\zeta_{13}\frac{\omega_1}{M_1} + \zeta_{12}\zeta_{23}\frac{\omega_2}{M_2} + \zeta_{13}\zeta_{23}\frac{\omega_3}{M_3}\right] \tag{A-5}$$

Putting (A-5) into (A-4) leads to:

$$D_{11}^* = \frac{\omega_1}{\rho N_A^2\left(\zeta_{12}\zeta_{13}\frac{\omega_1}{M_1} + \zeta_{12}\zeta_{23}\frac{\omega_2}{M_2} + \zeta_{13}\zeta_{23}\frac{\omega_3}{M_3}\right)}\left[\begin{array}{l}\left(\omega_1\frac{M_3}{M_1}\zeta_{12} + (\omega_2+\omega_3)\zeta_{23}\right)\left(\frac{\partial \mu_1}{\partial \omega_1}\right) \\ +\left(\omega_2\frac{M_3}{M_2}\zeta_{12} + \omega_2\zeta_{13}\right)\left(\frac{\partial \mu_2}{\partial \omega_1}\right)\end{array}\right] \tag{A-6}$$

Appendix-B

Relation between the Friction Coefficients, ζ_{ij}, and the Self Diffusion Coefficients, D_i

From Bearman,[15] the self diffusion coefficients are related to friction coefficients by,

$$D_i = \frac{kT}{\zeta_i} \tag{B-1}$$

$$\zeta_i = \sum_{j=1}^{N} c_j \zeta_{ij} \tag{B-2}$$

Applying these equations to the binary case:

$$\zeta_1 = c_1\zeta_{11} + c_2\zeta_{12} \tag{B-3}$$

$$\zeta_2 = c_1\zeta_{21} + c_2\zeta_{22} \tag{B-4}$$

$$D_1 = \frac{kT}{c_1\zeta_{11} + c_2\zeta_{12}} \tag{B-5}$$

$$D_2 = \frac{kT}{c_1\zeta_{12} + c_2\zeta_{22}} \tag{B-6}$$

where,

$$c_i[=]\frac{molecules}{volume} = N_A\frac{\rho_i}{M_i} \tag{B-7}$$

$$k = \frac{R}{N_A} \tag{B-8}$$

Assuming a geometric mean for the friction coefficients:

$$\zeta_{12} = (\zeta_{11}\zeta_{22})^{1/2} \tag{B-9}$$

one can invert Eqs. (B-5) and (B-6) to find the relationships between self-friction coefficients and self diffusion coefficients.

$$\zeta_{11} = \frac{kT}{D_1\left[c_1 + \frac{D_1}{D_2}c_2\right]} \tag{B-10}$$

$$\zeta_{22} = \frac{kT}{D_2\left[\frac{D_2}{D_1}c_1 + c_2\right]} \tag{B-11}$$

For the ternary case the same analysis applies. We denote by components 1 and 2 the feed (solvent, impurity) and by component 3 the membrane material (polymer melt or network). The relation between self friction and self diffusion coefficients uses the symmetry of the cross friction coefficients

$$\begin{aligned} \zeta_{12} &= \zeta_{21} \\ \zeta_{13} &= \zeta_{31} \\ \zeta_{23} &= \zeta_{32} \end{aligned} \tag{B-12}$$

the geometric mean rule

$$\begin{aligned} \zeta_{12} &= \left(\zeta_{11}\zeta_{22}\right)^{1/2} \\ \zeta_{13} &= \left(\zeta_{11}\zeta_{33}\right)^{1/2} \\ \zeta_{23} &= \left(\zeta_{22}\zeta_{33}\right)^{1/2} \end{aligned} \tag{B-13}$$

and Bearman's expressions for self diffusion coefficients:

$$D_1 = \frac{kT}{c_1\zeta_{11} + c_2\zeta_{12} + c_3\zeta_{13}} \tag{B-14}$$

$$D_2 = \frac{kT}{c_1\zeta_{21} + c_2\zeta_{22} + c_3\zeta_{23}} \tag{B-15}$$

$$D_3 = \frac{kT}{c_1\zeta_{31} + c_2\zeta_{32} + c_3\zeta_{33}} \tag{B-16}$$

The inversion of these equations using the application of the previous conditions provides,

$$\zeta_{11} = \frac{kT}{D_1\left[c_1 + \frac{D_1}{D_2}c_2 + \frac{D_1}{D_3}c_3\right]} \tag{B-17}$$

$$\zeta_{22} = \frac{kT}{D_2\left[\frac{D_2}{D_1}c_1 + c_2 + \frac{D_2}{D_3}c_3\right]} \tag{B-18}$$

$$\zeta_{33} = \frac{kT}{D_3\left[\frac{D_3}{D_1}c_1 + \frac{D_3}{D_2}c_2 + c_3\right]} \tag{B-19}$$

These results can be extended by induction to N components in molecular form,

$$\boxed{\zeta_{ii} = \frac{kT}{D_i \sum_{j=1}^{N} c_j \frac{D_i}{D_j}}} \tag{B-20}$$

and in molar form,

$$\boxed{\zeta_{ii} = \frac{RT}{N_A^2 D_i \sum_{j=1}^{N} \frac{\rho_j}{M_j} \frac{D_i}{D_j}}} \tag{B-21}$$

Appendix-C

Replacing ζ_{ij} with D_i in D_{ij}^*

Replacing in Eq. (4-29) the cross friction coefficients, ζ_{ij}, with self friction coefficients, ζ_{ii}, using Eq. (B-15) following expression is obtained for D_{11}^*:

$$D_{11}^* = \frac{\omega_1}{\rho N_A^2 \left(\zeta_{11}\zeta_{22}^{1/2}\zeta_{33}^{1/2}\frac{\omega_1}{M_1} + \zeta_{11}^{1/2}\zeta_{22}\zeta_{33}^{1/2}\frac{\omega_2}{M_2} + \zeta_{11}^{1/2}\zeta_{22}^{1/2}\zeta_{33}\frac{\omega_3}{M_3} \right)} \left[\begin{array}{l} \left(\omega_1 \frac{M_3}{M_1}\zeta_{11}^{1/2}\zeta_{22}^{1/2} + (\omega_2+\omega_3)\zeta_{22}^{1/2}\zeta_{33}^{1/2} \right)\left(\frac{\partial \mu_1}{\partial \omega_1} \right) \\ + \left(\omega_2 \frac{M_3}{M_2}\zeta_{11}^{1/2}\zeta_{22}^{1/2} - \omega_2 \zeta_{11}^{1/2}\zeta_{33}^{1/2} \right)\left(\frac{\partial \mu_2}{\partial \omega_1} \right) \end{array} \right] \tag{C-1}$$

Appendix B supplies the results (B-17) – (B19) connecting the ζ_{ii} to the D_i. Consequently one can write

$$D_{11}^* = A(B+C) \tag{C-2}$$

where,

$$A = \frac{\omega_1}{\rho RT \left(\frac{1}{D_1\left(\frac{\rho_1}{M_1}+\frac{\rho_2 D_1}{M_2 D_2}+\frac{\rho_3 D_1}{M_3 D_3}\right) D_2\left(\frac{\rho_1 D_2}{M_1 D_1}+\frac{\rho_2}{M_2}+\frac{\rho_3 D_2}{M_3 D_3}\right) D_3\left(\frac{\rho_1 D_3}{M_1 D_1}+\frac{\rho_2 D_3}{M_2 D_2}+\frac{\rho_3}{M_3}\right)} \right)^{1/2} \left[\left(\frac{1}{D_1\left(\frac{\rho_1}{M_1}+\frac{\rho_2 D_1}{M_2 D_2}+\frac{\rho_3 D_1}{M_3 D_3}\right)} \right)^{1/2} \frac{\omega_1}{M_1} + \left(\frac{1}{D_2\left(\frac{\rho_1 D_2}{M_1 D_1}+\frac{\rho_2}{M_2}+\frac{\rho_3 D_2}{M_3 D_3}\right)} \right)^{1/2} \frac{\omega_2}{M_2} + \left(\frac{1}{D_3\left(\frac{\rho_1 D_3}{M_1 D_1}+\frac{\rho_2 D_3}{M_2 D_2}+\frac{\rho_3}{M_3}\right)} \right)^{1/2} \frac{\omega_3}{M_3} \right]} \tag{C-3}$$

$$B = \left[\left(\omega_1 \frac{M_3}{M_1} \left(\frac{1}{D_1\left(\frac{\rho_1}{M_1}+\frac{\rho_2 D_1}{M_2 D_2}+\frac{\rho_3 D_1}{M_3 D_3}\right)} \right)^{1/2} \left(\frac{1}{D_2\left(\frac{\rho_1 D_2}{M_1 D_1}+\frac{\rho_2}{M_2}+\frac{\rho_3 D_2}{M_3 D_3}\right)} \right)^{1/2} + (\omega_2+\omega_3) \left(\frac{1}{D_2\left(\frac{\rho_1 D_2}{M_1 D_1}+\frac{\rho_2}{M_2}+\frac{\rho_3 D_2}{M_3 D_3}\right)} \right)^{1/2} \left(\frac{1}{D_3\left(\frac{\rho_1 D_3}{M_1 D_1}+\frac{\rho_2 D_3}{M_2 D_2}+\frac{\rho_3}{M_3}\right)} \right)^{1/2} \right) \left(\frac{\partial \mu_1}{\partial \omega_1} \right) \right] \tag{C-4}$$

$$C = \left[\left(\omega_2 \frac{M_3}{M_2} \left(\frac{1}{D_1\left(\frac{\rho_1}{M_1}+\frac{\rho_2 D_1}{M_2 D_2}+\frac{\rho_3 D_1}{M_3 D_3}\right)} \right)^{1/2} \left(\frac{1}{D_2\left(\frac{\rho_1 D_2}{M_1 D_1}+\frac{\rho_2}{M_2}+\frac{\rho_3 D_2}{M_3 D_3}\right)} \right)^{1/2} - \omega_2 \left(\frac{1}{D_1\left(\frac{\rho_1}{M_1}+\frac{\rho_2 D_1}{M_2 D_2}+\frac{\rho_3 D_1}{M_3 D_3}\right)} \right)^{1/2} \left(\frac{1}{D_3\left(\frac{\rho_1 D_3}{M_1 D_1}+\frac{\rho_2 D_3}{M_2 D_2}+\frac{\rho_3}{M_3}\right)} \right)^{1/2} \right) \left(\frac{\partial \mu_2}{\partial \omega_1} \right) \right] \tag{C-5}$$

Defining

$$\left(\frac{\rho_1}{M_1}D_1^{\oplus}\right)=D_1\left(\frac{\rho_1}{M_1}+\frac{\rho_2 D_1}{M_2 D_2}+\frac{\rho_3 D_1}{M_3 D_3}\right) \tag{C-6}$$

$$\left(\frac{\rho_2}{M_2}D_2^{\oplus}\right)=D_2\left(\frac{\rho_1 D_2}{M_1 D_1}+\frac{\rho_2}{M_2}+\frac{\rho_3 D_2}{M_3 D_3}\right) \tag{C-7}$$

$$\left(\frac{\rho_3}{M_3}D_3^{\oplus}\right)=D_3\left(\frac{\rho_1 D_3}{M_1 D_1}+\frac{\rho_2 D_3}{M_2 D_2}+\frac{\rho_3}{M_3}\right) \tag{C-8}$$

the result for D_{11}^{*} can be cast

$$D_{11}^{*}=\frac{\omega_1(\rho_1\rho_2\rho_3)^{1/2}(D_1^{\oplus}D_2^{\oplus}D_3^{\oplus})^{1/2}}{RT(M_1M_2M_3)^{1/2}\left(\left(\frac{\rho_1}{M_1D_1^{\oplus}}\right)^{1/2}+\left(\frac{\rho_2}{M_2D_2^{\oplus}}\right)^{1/2}+\left(\frac{\rho_3}{M_3D_3^{\oplus}}\right)^{1/2}\right)}\left[\begin{array}{l}\left(\omega_1\frac{M_3}{M_1}\left(\frac{M_1}{\rho_1D_1^{\oplus}}\right)^{1/2}\left(\frac{M_2}{\rho_2D_2^{\oplus}}\right)^{1/2}+(\omega_2+\omega_3)\left(\frac{M_2}{\rho_2D_2^{\oplus}}\right)^{1/2}\left(\frac{M_3}{\rho_3D_3^{\oplus}}\right)^{1/2}\right)\left(\frac{\partial\mu_1}{\partial\omega_1}\right)\\+\left(\omega_2\frac{M_3}{M_2}\left(\frac{M_1}{\rho_1D_1^{\oplus}}\right)^{1/2}\left(\frac{M_2}{\rho_2D_2^{\oplus}}\right)^{1/2}-\omega_2\left(\frac{M_1}{\rho_1D_1^{\oplus}}\right)^{1/2}\left(\frac{M_3}{\rho_3D_3^{\oplus}}\right)^{1/2}\right)\left(\frac{\partial\mu_2}{\partial\omega_1}\right)\end{array}\right] \tag{C-9}$$

The same analysis performed for the other three multicomponent diffusivities D_{12}^{*}, D_{21}^{*} & D_{22}^{*} gives:

$$D_{12}^{*}=\frac{\omega_1(\rho_1\rho_2\rho_3)^{1/2}(D_1^{\oplus}D_2^{\oplus}D_3^{\oplus})^{1/2}}{RT(M_1M_2M_3)^{1/2}\left(\left(\frac{\rho_1}{M_1D_1^{\oplus}}\right)^{1/2}+\left(\frac{\rho_2}{M_2D_2^{\oplus}}\right)^{1/2}+\left(\frac{\rho_3}{M_3D_3^{\oplus}}\right)^{1/2}\right)}\left[\begin{array}{l}\left(\omega_1\frac{M_3}{M_1}\left(\frac{M_1}{\rho_1D_1^{\oplus}}\right)^{1/2}\left(\frac{M_2}{\rho_2D_2^{\oplus}}\right)^{1/2}+(\omega_2+\omega_3)\left(\frac{M_2}{\rho_2D_2^{\oplus}}\right)^{1/2}\left(\frac{M_3}{\rho_3D_3^{\oplus}}\right)^{1/2}\right)\left(\frac{\partial\mu_1}{\partial\omega_2}\right)\\+\left(\omega_2\frac{M_3}{M_2}\left(\frac{M_1}{\rho_1D_1^{\oplus}}\right)^{1/2}\left(\frac{M_2}{\rho_2D_2^{\oplus}}\right)^{1/2}-\omega_2\left(\frac{M_1}{\rho_1D_1^{\oplus}}\right)^{1/2}\left(\frac{M_3}{\rho_3D_3^{\oplus}}\right)^{1/2}\right)\left(\frac{\partial\mu_2}{\partial\omega_2}\right)\end{array}\right] \tag{C-10}$$

$$D_{21}^{*}=\frac{\omega_1(\rho_1\rho_2\rho_3)^{1/2}(D_1^{\oplus}D_2^{\oplus}D_3^{\oplus})^{1/2}}{RT(M_1M_2M_3)^{1/2}\left(\left(\frac{\rho_1}{M_1D_1^{\oplus}}\right)^{1/2}+\left(\frac{\rho_2}{M_2D_2^{\oplus}}\right)^{1/2}+\left(\frac{\rho_3}{M_3D_3^{\oplus}}\right)^{1/2}\right)}\left[\begin{array}{l}\left(\omega_1\frac{M_3}{M_1}\left(\frac{M_1}{\rho_1D_1^{\oplus}}\right)^{1/2}\left(\frac{M_2}{\rho_2D_2^{\oplus}}\right)^{1/2}-\omega_1\left(\frac{M_2}{\rho_2D_2^{\oplus}}\right)^{1/2}\left(\frac{M_3}{\rho_3D_3^{\oplus}}\right)^{1/2}\right)\left(\frac{\partial\mu_1}{\partial\omega_1}\right)\\+\left(\omega_2\frac{M_3}{M_2}\left(\frac{M_1}{\rho_1D_1^{\oplus}}\right)^{1/2}\left(\frac{M_2}{\rho_2D_2^{\oplus}}\right)^{1/2}+(\omega_1+\omega_3)\left(\frac{M_1}{\rho_1D_1^{\oplus}}\right)^{1/2}\left(\frac{M_3}{\rho_3D_3^{\oplus}}\right)^{1/2}\right)\left(\frac{\partial\mu_2}{\partial\omega_1}\right)\end{array}\right] \tag{C-11}$$

$$D_{22}^{*}=\frac{\omega_1(\rho_1\rho_2\rho_3)^{1/2}(D_1^{\oplus}D_2^{\oplus}D_3^{\oplus})^{1/2}}{RT(M_1M_2M_3)^{1/2}\left(\left(\frac{\rho_1}{M_1D_1^{\oplus}}\right)^{1/2}+\left(\frac{\rho_2}{M_2D_2^{\oplus}}\right)^{1/2}+\left(\frac{\rho_3}{M_3D_3^{\oplus}}\right)^{1/2}\right)}\left[\begin{array}{l}\left(\omega_1\frac{M_3}{M_1}\left(\frac{M_1}{\rho_1D_1^{\oplus}}\right)^{1/2}\left(\frac{M_2}{\rho_2D_2^{\oplus}}\right)^{1/2}-\omega_1\left(\frac{M_2}{\rho_2D_2^{\oplus}}\right)^{1/2}\left(\frac{M_3}{\rho_3D_3^{\oplus}}\right)^{1/2}\right)\left(\frac{\partial\mu_1}{\partial\omega_2}\right)\\+\left(\omega_2\frac{M_3}{M_2}\left(\frac{M_1}{\rho_1D_1^{\oplus}}\right)^{1/2}\left(\frac{M_2}{\rho_2D_2^{\oplus}}\right)^{1/2}+(\omega_1+\omega_3)\left(\frac{M_1}{\rho_1D_1^{\oplus}}\right)^{1/2}\left(\frac{M_3}{\rho_3D_3^{\oplus}}\right)^{1/2}\right)\left(\frac{\partial\mu_2}{\partial\omega_2}\right)\end{array}\right] \tag{C-12}$$

Appendix-D

Trace Limits Values of $D_i^{\oplus}$, Φ and Φ_i (i=1, 4)

For a ternary system,

$$\lim_{\substack{\omega_1,\omega_2\to 0\\ \omega_3\to 1}}\left(\frac{\rho_1}{M_1}D_1^{\oplus}\right)\equiv\frac{D_1^2\rho}{D_3M_3} \tag{D-1}$$

$$\lim_{\substack{\omega_1,\omega_2\to 0\\ \omega_3\to 1}}\left(\frac{\rho_2}{M_2}D_2^{\oplus}\right)\equiv\frac{D_2^2\rho}{D_3M_3} \tag{D-2}$$

$$\lim_{\substack{\omega_1,\omega_2\to 0\\ \omega_3\to 1}}\left(\frac{\rho_3}{M_3}D_3^{\oplus}\right)\equiv\frac{D_3\rho}{M_3} \tag{D-3}$$

$$\lim_{\substack{\omega_1,\omega_2\to 0\\ \omega_3\to 1}}\Phi=\frac{(\rho_1\rho_2\rho_3)^{1/2}(D_1^{\oplus}D_2^{\oplus}D_3^{\oplus})^{1/2}}{RT(M_1M_2M_3)^{1/2}\left(\left(\frac{\rho_1}{M_1D_1^{\oplus}}\right)^{1/2}+\left(\frac{\rho_2}{M_2D_2^{\oplus}}\right)^{1/2}+\left(\frac{\rho_3}{M_3D_3^{\oplus}}\right)^{1/2}\right)} \tag{D-4}$$

$$\lim_{\substack{\omega_1,\omega_2\to 0\\ \omega_3\to 1}}\Phi_1=\omega_1\frac{M_3}{M_1}\left(\frac{M_1}{\rho_1D_1^{\oplus}}\right)^{1/2}\left(\frac{M_2}{\rho_2D_2^{\oplus}}\right)^{1/2}+(\omega_2+\omega_3)\left(\frac{M_2}{\rho_2D_2^{\oplus}}\right)^{1/2}\left(\frac{M_3}{\rho_3D_3^{\oplus}}\right)^{1/2} \tag{D-5}$$

$$\lim_{\substack{\omega_1,\omega_2\to 0\\ \omega_3\to 1}}\Phi_2=\omega_1\frac{M_3}{M_2}\left(\frac{M_1}{\rho_1D_1^{\oplus}}\right)^{1/2}\left(\frac{M_2}{\rho_2D_2^{\oplus}}\right)^{1/2}-\omega_1\left(\frac{M_1}{\rho_1D_1^{\oplus}}\right)^{1/2}\left(\frac{M_3}{\rho_3D_3^{\oplus}}\right)^{1/2} \tag{D-6}$$

$$\lim_{\substack{\omega_1,\omega_2\to 0\\ \omega_3\to 1}}\Phi_3=\omega_1\frac{M_3}{M_1}\left(\frac{M_1}{\rho_1D_1^{\oplus}}\right)^{1/2}\left(\frac{M_2}{\rho_2D_2^{\oplus}}\right)^{1/2}-\omega_1\left(\frac{M_2}{\rho_2D_2^{\oplus}}\right)^{1/2}\left(\frac{M_3}{\rho_3D_3^{\oplus}}\right)^{1/2} \tag{D-7}$$

$$\lim_{\substack{\omega_1,\omega_2\to 0\\ \omega_3\to 1}}\Phi_4=\omega_1\frac{M_3}{M_2}\left(\frac{M_1}{\rho_1D_1^{\oplus}}\right)^{1/2}\left(\frac{M_2}{\rho_2D_2^{\oplus}}\right)^{1/2}+\frac{\omega_1}{\omega_2}(\omega_1+\omega_3)\left(\frac{M_1}{\rho_1D_1^{\oplus}}\right)^{1/2}\left(\frac{M_3}{\rho_3D_3^{\oplus}}\right)^{1/2} \tag{D-8}$$

Appendix-E

High Molecular Weight Limiting Values of $D_i^{\oplus}$, Φ and Φ_i (i=1, 4)

$$\lim_{\substack{M_3\to\infty \\ D_3\to 0 \\ D_3M_3\to 0}} D_1^{\oplus} = \left(\frac{D_3}{D_1}\right)^{1/2}\left(\frac{M_3}{D_1\rho_3}\right)^{1/2} \tag{E-1}$$

$$\lim_{\substack{M_3\to\infty \\ D_3\to 0 \\ D_3M_3\to 0}} D_2^{\oplus} = \left(\frac{D_3}{D_2}\right)^{1/2}\left(\frac{M_3}{D_2\rho_3}\right)^{1/2} \tag{E-2}$$

$$\lim_{\substack{M_3\to\infty \\ D_3\to 0 \\ D_3M_3\to 0}} D_3^{\oplus} = \left(\frac{M_3}{D_3\rho_3}\right)^{1/2} \tag{E-3}$$

Using these results, it is also found that:

$$\lim_{\substack{M_3\to\infty \\ D_3\to 0 \\ D_3M_3\to 0}} \Phi = \frac{\omega_1 D_1 D_2 \rho_3^2}{\rho RTM_3\omega_3} \tag{E-4}$$

$$\lim_{\substack{M_3\to\infty \\ D_3\to 0 \\ D_3M_3\to 0}} \Phi_1 = \frac{\omega_1 M_3^2 D_3}{M_1 D_1 D_2 \rho_3} + \frac{(\omega_2+\omega_3)M_3}{D_2\rho_3} \tag{E-5}$$

$$\lim_{\substack{M_3\to\infty \\ D_3\to 0 \\ D_3M_3\to 0}} \Phi_2 = \frac{\omega_2 M_3^2 D_3}{M_2 D_1 D_2 \rho_3} - \frac{\omega_2 M_3}{D_1\rho_3} \tag{E-6}$$

$$\lim_{\substack{M_3\to\infty \\ D_3\to 0 \\ D_3M_3\to 0}} \Phi_3 = \frac{\omega_1 M_3^2 D_3}{M_1 D_1 D_2 \rho_3} - \frac{\omega_1 M_3}{D_2\rho_3} \tag{E-7}$$

$$\lim_{\substack{M_3\to\infty \\ D_3\to 0 \\ D_3M_3\to 0}} \Phi_4 = \frac{\omega_2 M_3^2 D_3}{M_2 D_1 D_2 \rho_3} + \frac{(\omega_1+\omega_3)M_3}{D_1\rho_3} \tag{E-8}$$

Appendix-F

Analysis of a Binary System

Here we establish that the same sequence of steps used to develop Eqs. (4-30) – (4-33) from the CB theory[1] in a ternary system lead to the well established relationships for an ordinary diffusion flux in a binary system.[9]

The multicomponent diffusivities $\tilde{D}_{ij}$ depend on the symmetric diffusivity definition given by Curtiss in 1968.[14]

$$\tilde{D}_{ij} = \frac{cRT\alpha_{ij}}{\rho_i \rho_j} \tag{F-1}$$

which have the properties:

$$\tilde{D}_{ij} = \tilde{D}_{ji} \tag{F-2}$$

$$\sum_{i=1}^{N} \omega_i \tilde{D}_{ij} = 0 \tag{F-3}$$

Equation 2.9 of the CB theory[1] establishes the relation between the mass flux of component *i* relative to the local velocity and the driving forces as:

$$j_i = -D_i^T \nabla \ln T - \rho_i \sum_{j=1}^{N} \tilde{D}_{ij} d_j \tag{F-4}$$

The driving force d_i has units $[=]\frac{1}{L}$ and the multicomponent diffusivities $\tilde{D}_{ij}$ have units $[=]\frac{L^2}{t}$. For the isothermal, isobaric case with no external body forces applied we have for a binary case,

$$j_1 = -\rho_1 \left(\tilde{D}_{11} d_1 + \tilde{D}_{12} d_2 \right) \tag{F-5}$$

$$j_2 = -\rho_2 \left(\tilde{D}_{21} d_1 + \tilde{D}_{22} d_2 \right) \tag{F-6}$$

The "Fickian" diffusivities are related to the "Stefan-Maxwell" diffusivities ($\tilde{C}_{ij}$) in the CB theory[1] by:

$$\tilde{D}_{11} = \frac{\omega_2^2}{\tilde{C}_{12}} \tag{F-7}$$

$$\tilde{D}_{12} = -\frac{\omega_1 \omega_2}{\tilde{C}_{12}} \tag{F-8}$$

$$\tilde{D}_{22} = \frac{\omega_1^2}{\tilde{C}_{12}} \tag{F-9}$$

for the binary case from (F-5) and (F-6) we obtain:

$$j_1 = -\rho_1 \left(\frac{\omega_2^2}{\tilde{C}_{12}} d_1 - \frac{\omega_1 \omega_2}{\tilde{C}_{12}} d_2 \right) \tag{F-10}$$

$$j_2 = -\rho_2 \left(-\frac{\omega_1 \omega_2}{\tilde{C}_{12}} d_1 + \frac{\omega_1^2}{\tilde{C}_{12}} d_2 \right) \tag{F-11}$$

From equation 7.8 of the CB theory[1] we have for an isobaric system with no forced diffusion. :

$$d_i = x_i \sum_{j=1}^{v-1} \left(\frac{\partial \ln a_i}{\partial x_j} \right)_{T,P,x} \nabla x_j \tag{F-12}$$

For the binary case

$$d_1 = x_1 \left(\frac{\partial \ln a_1}{\partial x_1} \right) \nabla x_1 \tag{F-13}$$

$$d_2 = x_2 \left(\frac{\partial \ln a_2}{\partial x_1} \right) \nabla x_1 \tag{F-14}$$

The activity is related with the chemical potential via:

$$\mu_i(T,P,x) = \mu_i^0(T,P) + RT \ln a_i \tag{F-15}$$

Incorporating this gives:

$$d_1 = \frac{x_1}{RT}\left(\frac{\partial \mu_1}{\partial x_1}\right)_{T,P} \nabla x_1 \tag{F-16}$$

Since the diffusional driving forces satisfy $\sum_i d_i = 0$ for the binary case,

$$d_1 = -d_2 \tag{F-17}$$

Replacing for d_2 in equation (F-10), the flux for component 1 is:

$$j_1 = -\rho_1\left(\frac{\omega_2^2}{\tilde{C}_{12}} + \frac{\omega_1\omega_2}{\tilde{C}_{12}}\right)d_1 \tag{F-18}$$

Introducing Eq. (F-16), we obtain:

$$j_1 = -\rho_1\left(\frac{\omega_2(\omega_1+\omega_2)}{\tilde{C}_{12}}\right)\frac{x_1}{RT}\left(\frac{\partial \mu_1}{\partial x_1}\right)_{T,P} \nabla x_1 \tag{F-19}$$

with $\sum_i \omega_i = 1$ and using the chain rule we obtain:

$$j_1 = -\rho_1\left(\frac{1}{\tilde{C}_{12}}\right)\frac{\omega_2 x_1}{RT}\left(\frac{\partial \mu_1}{\partial \omega_1}\right)_{T,P}\left(\frac{\partial \omega_1}{\partial x_1}\right)_{T,P} \nabla x_1 \tag{F-20}$$

Using that $\nabla \omega_1 = \left(\frac{\partial \omega_1}{\partial x_1}\right)_{T,P} \nabla x_1$ and $\rho_1 = \omega_1 \rho$ it follows

$$j_1 = -\rho\left(\frac{\omega_1\omega_2 x_1}{RT\,\tilde{C}_{12}}\left(\frac{\partial \mu_1}{\partial \omega_1}\right)_{T,P}\right)\nabla \omega_1 \tag{F-21}$$

which corresponds to the first Fick's Law with the binary mutual diffusion coefficient (D_{12}) given by:

$$D_{12} = \frac{\omega_1\omega_2 x_1}{RT\,\tilde{C}_{12}}\left(\frac{\partial \mu_1}{\partial \omega_1}\right)_{T,P} \tag{F-22}$$

From Bearman and Kirkwood[2], the Stefan-Maxwell diffusivity is related with the friction coefficient by:

$$\tilde{C}_{12} = \frac{n\zeta_{12}x_1x_2}{kT} \tag{F-23}$$

Replacing $\tilde{C}_{12}$ in the equation (F-22) gives,

$$D_{12} = \frac{\omega_1\omega_2 x_1 KT}{RTn\zeta_{12}x_1x_2}\left(\frac{\partial\mu_1}{\partial\omega_1}\right)_{T,P} \tag{F-24}$$

or

$$D_{12} = \frac{\omega_1\omega_2}{N_A n\zeta_{12}x_2}\left(\frac{\partial\mu_1}{\partial\omega_1}\right)_{T,P} \tag{F-25}$$

since

$$n = cN_A \tag{F-26}$$

$$\left(\frac{\partial\mu_1}{\partial\omega_1}\right)_{T,P} = \left(\frac{\partial\mu_1}{\partial\rho_1}\right)_{T,P}\left(\frac{\partial\rho_1}{\partial\omega_1}\right)_{T,P} \tag{F-27}$$

$$\omega_i = \frac{\rho_i}{\rho}; x_i = \frac{c_i}{c}; c_i = \frac{\rho_i}{M_i}; c = \frac{\rho}{M} \tag{F-28}$$

with

$$M = \sum_i x_i M_i \tag{F-29}$$

the following equation is obtained for the mutual diffusion coefficient:

$$D_{12} = \frac{\omega_1\omega_2}{N_A^2 c\varsigma_{12}x_2}\left(\frac{\partial\mu_1}{\partial\rho_1}\right)_{T,P}\left(\frac{\partial\rho_1}{\partial\omega_1}\right)_{T,P} \tag{F-30}$$

One needs $\left(\frac{\partial\rho_1}{\partial\omega_1}\right)_{T,P}$ in order to make the connection with the Vrentas and Duda's results.[9]

Assuming the partial specific volumes are independent of the concentration; that is, that the volume change of mixing is negligible[16], one has $\rho_i = \frac{\omega_i}{\sum \omega_i \hat{V}_i^0}$ so that

$$\left(\frac{\partial \rho_1}{\partial \omega_1}\right)_{T,P} = \frac{\left(\omega_1 \hat{V}_1^0 + \omega_2 \hat{V}_2^0\right) - \omega_1\left(\hat{V}_1^0 - \hat{V}_2^0\right)}{\left(\omega_1 \hat{V}_1^0 + \omega_2 \hat{V}_2^0\right)^2} \tag{F-31}$$

which simplifies to,

$$\left(\frac{\partial \rho_1}{\partial \omega_1}\right)_{T,P} = \frac{\hat{V}_2^0}{\left(\omega_1 \hat{V}_1^0 + \omega_2 \hat{V}_2^0\right)^2} = \frac{\hat{V}_2}{\left(\omega_1 \hat{V}_1 + \omega_2 \hat{V}_2\right)^2} = \frac{\hat{V}_2}{\hat{V}^2} = \rho^2 \hat{V}_2 \tag{F-32}$$

Since $\hat{V}_1 = \hat{V}_1^0$ and $\hat{V}_2 = \hat{V}_2^0$. Putting the last result in equation (F-30), gives

$$D_{12} = \frac{\omega_1 \omega_2 \hat{V}_2}{N_A^2 c \zeta_{12} x_2 \hat{V}^2}\left(\frac{\partial \mu_1}{\partial \rho_1}\right)_{T,P} \tag{F-33}$$

Converting mole fraction to mass fraction and specific volume to density, the mutual diffusion coefficient can be expressed,

$$D_{12} = \frac{\rho_1 M_2 \hat{V}_2}{N_A^2 \zeta_{12}}\left(\frac{\partial \mu_1}{\partial \rho_1}\right)_{T,P} = D \tag{F-34}$$

The same analysis can be performed for component 2 (the polymer) obtaining:

$$D_{21} = \frac{\rho_2 M_1 \hat{V}_1}{N_A^2 \zeta_{12}}\left(\frac{\partial \mu_2}{\partial \rho_2}\right)_{T,P} = D \tag{F-35}$$

The expressions derived here for D correspond to those in Vrentas and Duda for the mutual diffusion coefficient derived directly form Bearman and Kirkwood results.[2]